Summer 8-12-2011

Structure and Properties of Bi-containing Mixed A-site Perovskites

David M. Stein
University of Pennsylvania, dmstein@seas.upenn.edu

Structure and Properties of Bi-containing Mixed A-site Perovskites

Abstract

This thesis describes a series of studies undertaken to explore the criteria for the stabilization of Bi^{3+} in a perovskite through the formation of mixed A-site solid solutions. Electronically similar to Pb^{2+} but with a smaller ionic radius, Bi^{3+} has the potential to replace and improve upon Pb-based counterparts for dielectric and piezoelectric applications.

Building off the discovery that $Bi(Zn_{1/2}Ti_{1/2})O_3$ increases the tetragonality of $PbTiO_3$, the first part of this work identified a new substituent, $Bi(Zn_{3/4}W_{1/4})O_6$, that is also able to increase the *c/a* of $PbTiO_3$. In the process, the crystal chemical criterion for enhancing the tetragonality of $PbTiO_3$ was clarified.

From there, these tetragonality-enhancing additives were introduced into lead-free perovskite chemistries in an attempt to stabilize a new generation of environmentally benign ferroelectric materials.

The final section returns to lead-containing systems by investigating ternary systems in an attempt to capture the high *c/a* of the mixed Pb-Bi systems at an MPB. Unexpected dielectric behavior was observed in some compositions, which was shown to be the result of the structure entering a region of 2-phase coexistence. A new crystal-chemical parameter is defined to describe the variance of the B-site displacement factors and used to develop an empirical model for predicting the incidence of this 2-phase coexistence region. An atomistic model similar to those of relaxor ferroelectrics was proposed to explain the behavior.

Degree Type
Dissertation

Degree Name
Doctor of Philosophy (PhD)

Graduate Group
Materials Science & Engineering

First Advisor
Peter K. Davies

Keywords
Piezoelectric, Perovskite, Lead-free, Ferroelectric, Dielectric, Curie temperature

Subject Categories
Ceramic Materials

STRUCTURE AND PROPERTIES OF BI-CONTAINING MIXED A-SITE PEROVSKITES

David Michael Stein

A Dissertation

in

Materials Science and Engineering

Presented to the Faculties of the University of Pennsylvania in Partial Fulfillment of the Requirements for the Degree of Doctor of Philosophy

2011

_____

Peter K. Davies, Professor of Materials Science and Engineering
Supervisor of Dissertation

_____

Russell Composto, Professor of Materials Science and Engineering
Graduate Group Chair

Dissertation Committee:
Dawn Bonnell, Professor of Materials Science and Engineering
Andrew Rappe, Professor of Chemistry
John Vohs, Professor of Chemical Engineering

Acknowledgements

While the technical contributions of others on one's research are regularly acknowledged through references, contributions of a more social nature rarely get their due. I appreciate the opportunity to thank those people without whom this dissertation would not be possible. I only hope I don't slight anyone.

I'd like to start with expressing my gratitude to my advisor, Peter K. Davies, who has patiently guided me through this process. His influence on my research is obvious, but it's his influence on my writing that may have the most lasting effect. I hope that someday I am able to create compelling storylines from my data as easily and naturally as he does.

Looking back, I can count three people who had a disproportional effect on bending my life's trajectory towards this path, though their effect on my life is hardly limited to this contribution. My high school football coach, Terry Verelli, was the first person to suggest I attend Carnegie Mellon. Once there, Lane Martin convinced me to take the introductory materials science course and my undergraduate research advisor, Prof. Paul Salvador, was instrumental in my decision to pursue a career in materials research. I'd also like to thank the entire materials science department there for promoting undergraduate research; classwork is no substitute for the experience of scientific research. For this and more, I thank you all.

I am also very thankful for the people I have had the honor to work with here at Penn. Matt Suchomel served variously as a mentor, collaborator, and friend. I hope this arrangement is able to continue in the future. The research group of Prof. Andrew Rappe, especially Joe Bennett and Ilya Grinberg, was both a pleasure to work with and a strong influence on my understanding of the field. I'm also lucky to have worked with many thoughtful and fun people in the Davies

group. My experience here would have been much less rich if not for Hui, Niti, Thirumal, Beth, Mark, Yuqi, and Vince. I also need to thank Pat Overend for knowing the answer to every bureaucratic question I ever posed as well as making the department feel more like a family and Bill Romanow & Steve Szewczyk for keeping our lab running when we couldn't.

I've also been lucky to have found such a great group of friends in this department and city. I met David Conklin on my first official day at Penn and he has been there for all the ups and downs of this process. The ever evolving lunch crew has always been a highlight of my days here. I'll never be able to think about darts, Uno®, or movies starring Jason Statham (among other topics) without thinking about one version of the group or another. I'd especially like to thank Jamie Ford for being such a curmudgeon for our entertainment, Evan Goulet for somehow being both my landlord and frequent houseguest, and Mike Hore for sharing a love of beer, Star Trek, and computer hardware. Outside the department, I'd like to thank Jason Strohl for going on cycling adventures with me, the Pizza Rustica crew for providing such a comfortable atmosphere so close to the LRSM, and all my other friends who have shared this time with me.

Above all, I want to thank my family. I don't remember a time when I wasn't interested in learning about the world and I have my parents to thank for that. They always nurtured my curiosity and without that sense of wonder and awe I never would have considered this path. Thank you to my siblings, Danielle and Brian, for helping to make my childhood one I remember fondly and for growing into adults that I enjoy being around more each time we see each other. And to Kristin: you are wonderful person whom I am lucky to have met, let alone spend my life with. You are the Mary J. Blige to my Method Man. And lastly to Gumbo and Clarence: your goofy faces make me smile every time I look at you and that's all I need.

- David M. Stein

ABSTRACT

STRUCTURE AND PROPERTIES OF BI-CONTAINING MIXED A-SITE PEROVSKITES

David Michael Stein
Peter K. Davies

This thesis describes a series of studies undertaken to explore the criteria for the stabilization of Bi^{3+} in a perovskite through the formation of mixed A-site solid solutions. Electronically similar to Pb^{2+} but with a smaller ionic radius, Bi^{3+} has the potential to replace and improve upon Pb-based counterparts for dielectric and piezoelectric applications.

Building off the discovery that $Bi(Zn_{1/2}Ti_{1/2})O_3$ increases the tetragonality of $PbTiO_3$, the first part of this work identified a new substituent, $Bi(Zn_{3/4}W_{1/4})O_6$, that is also able to increase the *c/a* of $PbTiO_3$. In the process, the crystal chemical criterion for enhancing the tetragonality of $PbTiO_3$ was clarified.

From there, these tetragonality-enhancing additives were introduced into lead-free perovskite chemistries in an attempt to stabilize a new generation of environmentally benign ferroelectric materials.

The final section returns to lead-containing systems by investigating ternary systems in an attempt to capture the high *c/a* of the mixed Pb-Bi systems at an MPB. Unexpected dielectric behavior was observed in some compositions, which was shown to be the result of the structure entering a region of 2-phase coexistence. A new crystal-chemical parameter is defined to describe the variance of the B-site displacement factors and used to develop an empirical model for predicting the incidence of this 2-phase coexistence region. An atomistic model similar to those of relaxor ferroelectrics was proposed to explain the behavior.

Contents

List of Tables

List of Figures

Chapter 1:

Introduction and Experimental Procedures

1.1 Introduction

1.1.1 Introduction to piezoelectric materials

Contemporary smartphones are as powerful as their desktop counterparts of less than a decade ago. While Moore's law is frequently expressed in terms of transistor counts or processing power, the processing and material improvements necessary to maintain the law also result in reduced power consumption for a given performance level. Even more striking is the number of features that smartphone manufacturers are able to squeeze into a pocket-sized package: digital camera, GPS, accelerometer, gyroscope, not to mention the wireless communications capabilities. This reduction in size has affected the flow of information in society in a profound way. With the miniaturization and commodification of semiconductor devices continuing unabated, it is now hard to name an area of life that has not yet seen the intrusion of electronic devices.

While silicon receives most of the recognition for this progress, much of the technology taken for granted today would not be possible without advanced ceramic materials. From sensors to filters, actuators and perhaps even tomorrow's non-volatile memory devices, ceramics are an important class of electronic materials. One driving force for the miniaturization of electronics has been the development of materials that can

mediate between physical and electronic systems directly. While there are many examples of similar phenomenon, this work is primarily focused on piezoelectricity.

Piezoelectric materials exhibit a form of electromechanical coupling: the polarization of the material varies in response to an applied strain. In this manner, pressure changes can be quickly and easily detected. Conversely, an electronic system can use an applied field to physically alter the shape of a piezoelectric material, thereby acting as an actuator. A simplified schematic of how the piezoelectric effect works in devices is shown in Figure 1.1.

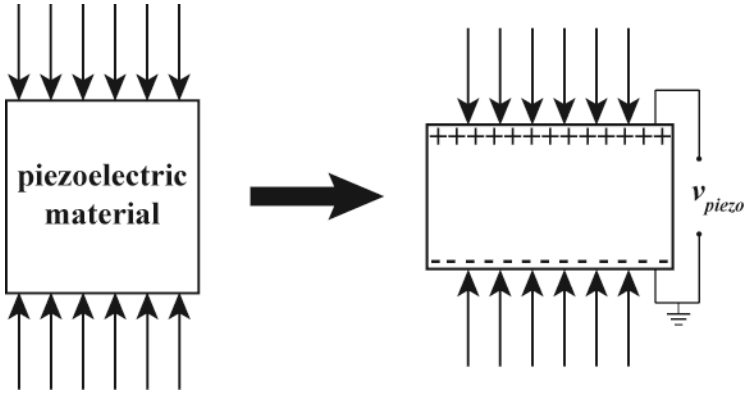

Figure 1.1: Schematic of the piezoelectric effect. Arrows represent a physical stress placed on the device.

Piezoelectric materials are used in many common and technological devices. Cigarette lighters in automobiles were an early mainstream use of piezoelectric materials, but the popularity of that feature is waning. A similar mechanism, however, is used in gas grills for push-button starting. As sensors, piezoelectrics are used in a diverse set of products from guitar pickups to sonar. Piezoelectrics are also found in applications where

precise control of physical objects over small distances is required, such as in atomic force microscopes or mirror alignment for lasers.

Piezoelectricity is observed in many materials. Indeed, all of the 20 (out of 32 total) non-centrosymmetric crystallographic point groups are capable of exhibiting piezoelectricity and other materials such as wood are able to exhibit the phenomenon due to microstructure considerations [Fukada 1955]. Some piezoelectric materials possess a permanent dipole even in the absence of an applied force while others only exhibit a polarization under an applied force. Quartz is the prototypical example of the latter, and is one of the most common piezoelectric materials in use today. Despite the popularity of quartz, the most common piezoelectric materials used today belong to the set of polar materials, in particular those materials with the perovskite structure. It is systems of this type that are the focus of this work.

1.1.2 Perovskites

The perovskite structure, of chemical formula ABX_3, consists of two distinct cation sites (A and B) and one anion site (X). A schematic of the structure is shown in Figure 1.2. Crystals of the prototypical perovskite, $CaTiO_3$, were first discovered in 1839 and structurally characterized in 1943 [Naray-Szabo 1943 A & B]. Later, as other similar materials were being characterized the name was applied to the class of materials sharing the structure [Megaw 1945]. The most frequent anion is oxygen, resulting in the ABO_3 oxide perovskites studied here. However, halide and sulfide perovskites are also known and of technological interest [Bennett 2009].

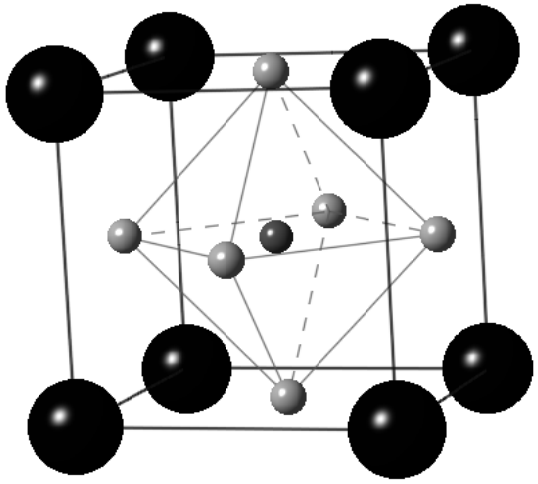

Fig. 1.2: The perovskite crystal structure.

In the perovskite structure, the larger A-site cation occupies a site with 12-fold coordination of the anion. In Figure 1.2 the large black spheres on the corners of the unit cell cube represent the A-site. The B-site cation, the smaller dark sphere at the center of the unit cell, is a part of a B-O_6 octahedral complex.

The utility of the perovskite structure derives from its ability to support a wide variety of cations on its two sites. The high symmetry cubic structure suggests tight tolerances for the ratio of A-site to B-site cation ionic radii, however wide ranges of chemistries can be accommodated by various distortions. This flexibility, both compositionally and structurally, has resulted in technological prominence for many perovskite systems. While this thesis is concerned primarily with systems that exhibit piezoelectricity many related perovskites are used in other applications. The identification and characterization of $BaTiO_3$ was the result of a war-time effort to find a high-κ replacement dielectric for muscovite as an insulator in capacitors. $SrRuO_3$ and

$LaCoO_3$, on the other hand, are widely used as conducting electrodes. $BiFeO_3$ is a promising multiferroic material with coupling of electronic and magnetic properties. Recent research into complex perovskite compositions has revealed previously unobserved periodic nanoscale features that may be useful as a template for nanostructures [Guiton 2007]. It is also believed that much of the earth's lower mantle exists in a perovskite structure [Zerr 1993].

The structures of perovskites are determined by short range attractive (bonding) and repulsive forces between nearby ions, as well as long range electrostatic interactions between unit cells. Composition determines the balance of these forces, and therefore the structure. The structure, in turn, contributes to the properties and performance of the material. The next section focuses on how compositional changes are understood to affect the structure of real perovskite materials.

1.2 Structural considerations in perovskite materials

1.2.1 Bonding

As a first approximation, ionic bonding considerations can be used to predict the perovskite structure of a given chemistry. Ideal bond lengths can be determined using ionic radii [Shannon 1976]. In the ionic limit, the high symmetry cubic structure is only stable if the A-O and B-O bond lengths properly match. The ratio of bonds is expressed by the Goldschmidt tolerance factor [Goldschmidt 1929]:

$$t = \frac{r_A + r_O}{\sqrt{2}\left(r_B + r_O\right)}$$

It is devised such that the ideal ratio of bond lengths results in a tolerance factor of unity. If instead $t < 1$ the preferred A-O bond lengths will be smaller than the cubic symmetry allows and can be accommodated by oxygen octahedral rotations around the A-site, illustrated in Figure 1.3. A systematic notation for describing and systematizing different possible tilt systems in perovskites was established by Glazer and is widely used today [Glazer 1972].

Conversely, if $t > 1$ the B-O bond lengths would be longer than preferred and the structure can compensate via a displacive distortion within the B-O_6 octahedra (Figure 1.4). This displacement of cations relative to the anion cage gives rise to a spontaneous and reversible electric dipole. Materials exhibiting these distortions are said to be ferroelectric if the dipoles align between unit cells.

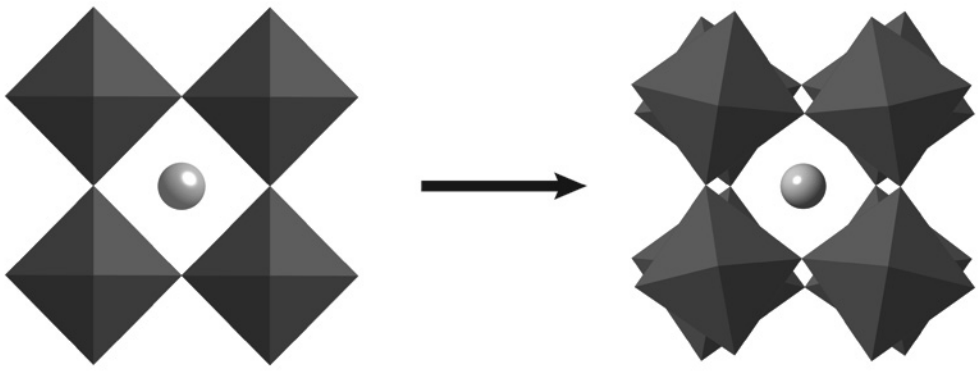

Figure 1.3: Schematic of octahedral tilting in perovskites.

The magnitude of a distortion induced by ionic bonding instabilities can be estimated using the bond-valence method [Brown 1978]. Bond-valence theory is based on the idea that the strength, or valence, of a bond in an inorganic material is related to the inverse of the bond length and that the sum of the bond valences for a given ion will approximately sum to its formal oxidation state. Calculating this sum for a Ti^{4+} cation on the ideal position within the oxygen octahedra of $PbTiO_3$ (t = 1.019) reveals that the Ti^{4+} is underbonded (bond-valence sum of 3.65); displacements along the <100> direction toward one of the oxygen ligands allows the total valence to equal the ideal value (4) [Brown 1976].

The displacive distortion of the B-site cation within the oxygen cage is generally accomplished by hybridization within the B-O_6 complex [Grinberg 2004 A]. The electronic energy of the B-O_6 complex can be reduced via a second-order Jahn-Teller

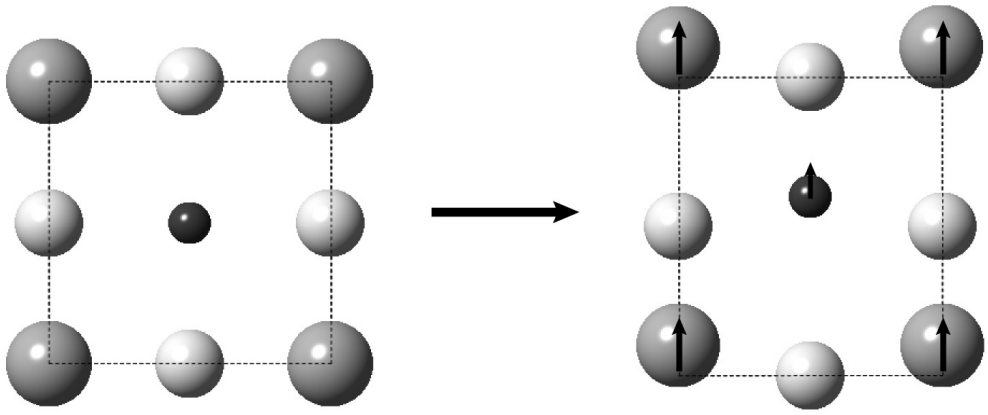

Figure 1.4: Schematic of displacive distortions in perovskites. Arrows indicate displacements of cations relative to anions.

distortion provided that the energy gap between the highest occupied states (O 2*p*) and lowest unoccupied states (generally B-cation *d* states) is small and there is a possible distortion with the same symmetry as the electronic transition [Kunz 1995]. Transition metals with d^0 electronic configuration (including Ti^{4+}) satisfy the latter condition when octahedrally coordinated; the relative energies of the electronic states in question is a function of the size and charge of the B-site cation. Cations with a larger formal charge and smaller ionic radius tend to form more strongly covalent bonds with the oxygen ligands, but the specific local electronic configuration of the cation also plays a role, as evidenced by the difference in bonding between Mg^{2+} and Zn^{2+} [Grinberg 2004 B]. While these two cations have similar radii, Zn^{2+} (0.74Å) has a filled 3*d*-shell with low-lying 4*p* states that hybridize with O 2*p* ligand states while Mg^{2+} (0.72Å) does not.

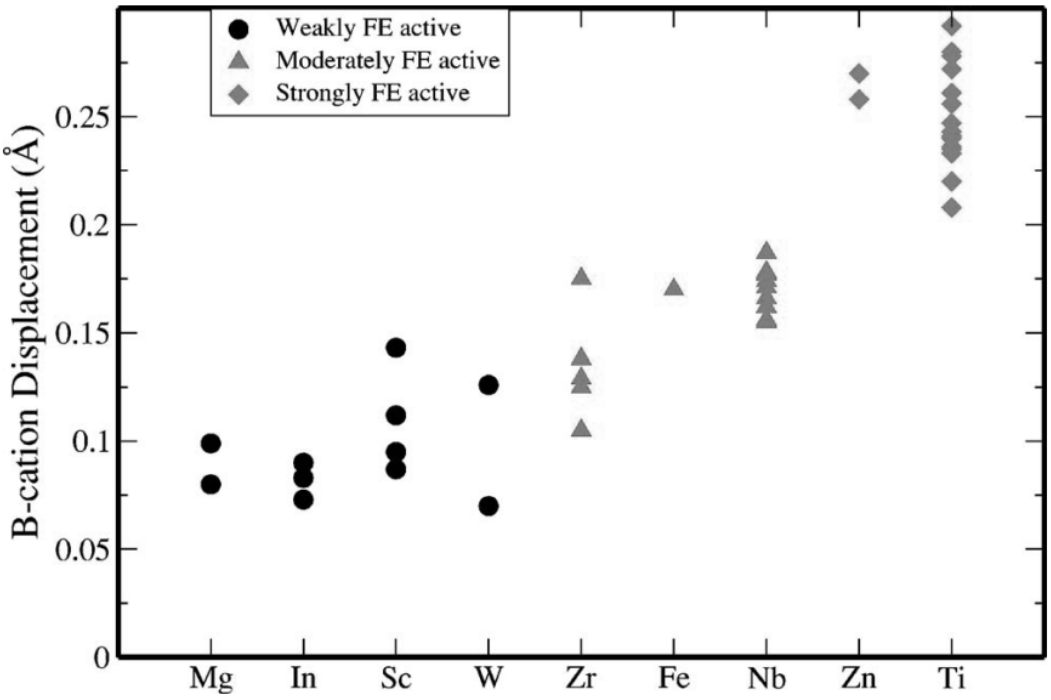

Figure 1.5: Distortion magnitudes (in angstroms) for *B* cations in PT solid solutions. Distortion magnitudes are especially large for Zn and Ti. [Reproduced from Grinberg 2005].

The magnitude of the displacive distortion of a cation depends on the local chemical environment, and therefore is non-trivial to quantify. Nonetheless, it is an important crystal-chemical parameter for predicting the behavior of ferroelectric materials. Grinberg *et al.* used first principles calculations to study the displacive behavior of common B-site cations in similar environments (reproduced in Figure 1.5) [Grinberg 2005]. This data was used to assign expected average displacements (d^0) for several cations, see Table 1.1. This table also includes d^0 values for Pb^{2+} and Bi^{3+} that were calculated in a similar manner. Higher d^0 values correspond to the ferroelectric-

Table 1.1: Table of average displacement magnitudes (d^0) for relevant A- and B-site cations

B-cation	d^0 (Å)	A-cation	d^0 (Å)
Mg^{2+}	0.08	Pb^{2+}	0.45
In^{3+}	0.07	Bi^{3+}	0.8
Sc^{3+}	0.11		
W^{6+}	0.1		
Zr^{4+}	0.13		
Fe^{3+}	0.17		
Nb^{5+}	0.17		
Zn^{2+}	0.25		
Ti^{4+}	0.25		

activity of a cation: Zn^{2+} and Ti^{4+} are considered strongly ferroelectrically-active, Mg^{2+} is essentially "not" and remains in a centro-symmetric octahedral environment.

In the Pb-containing systems of interest, octahedral rotations compete with ferroelectric displacive distortions to determine dielectric properties [Fornari 2001].

For the perovskites of interest in this thesis, particularly those containing Pb^{2+} or Bi^{3+}, covalent bonding on the A-site complex also produces ferroelectric distortions. Traditionally viewed as an accommodation of the 6*s* "inert lone pair", the extremely large displacements of Pb^{2+} (and Bi^{3+}) cations in many oxide structures has been shown to arise from hybridization of Pb/Bi 6*s* (and some 6*p*) states with the O 2*p* states [Cohen 1992, Watson 1999, Seshadri 2001]. The importance of matching the energies of the ligand and Pb/Bi states is demonstrated by comparison of the distortions in oxides to sulfides such as PbS, a cubic compound with no lone pair effect due to the difference in the electronic

configuration of oxygen and sulfur. The preference for displacement in Pb/Bi-containing perovskites is so strong that it is a primary determinant of the symmetry [Grinberg 2004 A]. Large displacements are found in all Pb-containing perovskites, including chemistries where the "average" structure has cubic symmetry and "local" displacements persist above the temperatures where the long-range structure transforms to a high-symmetry cubic state [Grinberg 2004 B, Egami 2003].

Octahedral rotations and ferroelectric displacements are not the only distortions found in perovskites. B-O_6 complexes can also distort without an increase in the covalency of the bonding through transverse distortions [Grinberg 2004 A]. In transverse off-centering, distortions of the oxygen cage polarizes the complex without forcing the B-site cation to displace. Finally, for compositions with sub-lattice compositional disorder cation ordering can induce significant alterations of the structure and properties of perovskites [Davies 1999].

1.2.2 Repulsive forces

Cation-cation repulsions, through direct repulsive forces or indirect anion-mediated repulsions, play a critical role in determining the overall structure of ferroelectric perovskites. As the corner-shared octahedra rotate, the B-O-B bond angles decrease from their ideal 180° value, reducing the distance between the B-site cations and increasing the repulsive forces felt by the cations. These cation-cation repulsions serve to moderate the tilting of the octahedra and mediate the direction of the cation off-centering to avoid displacement vectors toward neighboring cations. For example, Pb cations avoid (111) displacements in rhombohedral Zr-rich Pb(Ti,Zr)O_3 [Grinberg 2004 A]. These

direct repulsive forces can affect the structure in complex ways if there is compositional disorder on either cation sub-lattice [Dmowski 2000].

Indirect anion-mediated repulsions are also important in mediating displacive cation distortions and destabilize the formation of two short bonds by cations adjacent to the same anion, and therefore act as a repulsive force. This interaction can affect the structure in two ways. First, it affects the correlation of displacive distortions in neighboring unit cells. This is important in systems with mixed cation sub-lattices, such as $(K_{1/2}Bi_{1/2})TiO_3$, where the correlation of Bi^{3+} displacements compete with K^{+}-O-Bi^{3+} repulsions. Second, this interaction couples the displacements on the A- and B-site sub-lattices as the maximum displacement for a cation on either sub-lattice can only be realized when the movement is accommodated by a coupling of the displacements on the two sub-lattices in a way that minimizes the indirect repulsive forces [Grinberg 2002]. $PbTiO_3$ provides a good example where a large tetragonal distortion is induced through the large displacements of both the Pb^{2+} and Ti^{4+} cations.

1.2.3 Electrostatic interactions

The individual dipoles created by the short-range cation displacements within a unit cell interact over a large distances to minimize the electrostatic energy; these electrostatic interactions affect the structure in a manner similar to oxygen-mediated cation repulsions. In Pb-containing perovskites the preference for individual Pb^{2+} cation movement along {100} tends to stabilize ferroelectric phases with a tetragonal {100} distortion over those with a rhombohedral {111} displacement [Grinberg 2002].

1.2.4 Real structures

In real materials, the interactions described above compete to determine the resultant long-range crystal structure. The effect of composition on the balance of these forces is readily illustrated by the following series of simple perovskites.

In $BaZrO_3$, where the Ba^{2+} cation does not covalently bond with the oxygen ligands and the ionic radii of both species are well matched with regard to tolerance factor, the high-symmetry cubic structure is stable at all temperatures [Singh 2006]. The replacement of Zr^{4+} with the comparatively undersized and polarizable Ti^{4+} to form $BaTiO_3$ leads to the off-centering of the Ti^{4+} cations within the octahedral cage via hybridization between Ti 3*d* and O 2*p* orbitals to create individual dipoles within each unit cell. These dipoles correlate in different ways as thermal energy is increased resulting in a rhombohedral ground state that transitions to orthorhombic and then tetragonal symmetry prior to the transformation to a paraelectric cubic phase [Zhong 1994]. The magnitude of the individual dipoles also varies with temperature, giving the transitions displacive as well order-disorder character. The repulsive and dipole interactions originating from the displacement of Ti^{4+} also lead to cooperative displacement of Ba^{2+} on the A-site. The displacements of Ba^{2+} however are far smaller than the "lone-pair" driven off-centerings of Pb^{2+} in $PbTiO_3$.

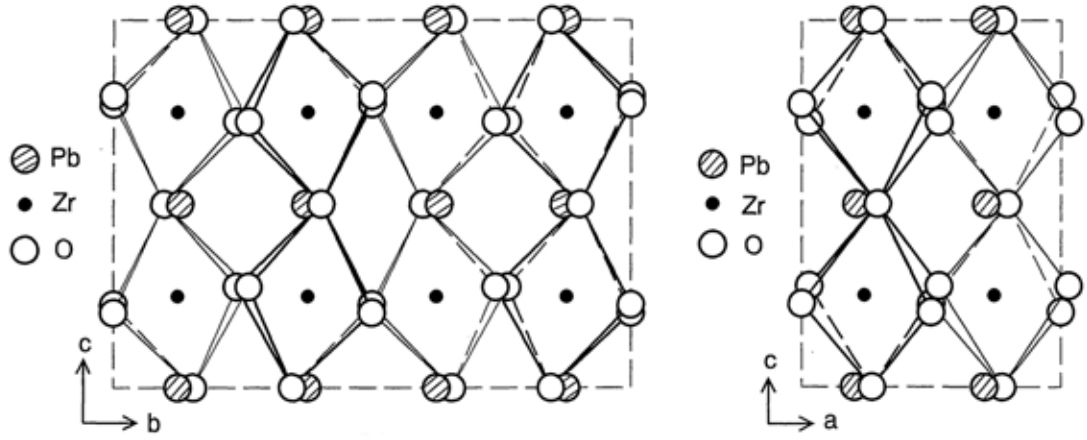

Figure 1.6: Schematic views of ZrO6 octahedra along [100] (left) and [010] (right) directions. Reproduced from [Fujishita 1997]

Replacement of the A-site cation with the highly covalent Pb^{2+} cation to form $PbTiO_3$ leads to large individual off-centerings that cooperatively displace with the B-site Ti^{4+} cations. The repulsive forces and stronger dipole interactions stabilize a (001) distorted tetragonal ground state that persists to the Curie temperature [Cohen 1992].

Materials such as $PbZrO_3$, which combine an A-site with strong displacements with a B-site cation that is unable to displace, adopt more complex structures as a result of the competition between the interactions (Figure 1.6) [Fujishita 1997]. This competition produces a complex antiferroelectric ground state that only bests the competing ferroelectric structure by less than 10% of the total energy below the high-symmetry cubic structure [Singh 1995]. This was shown to arise from avoidance of the large repulsive forces between Pb^{2+} and Zr^{4+} [Grinberg 2004 A].

1.3 Piezoelectricity in perovskite materials

1.3.1 Morphotropic phase boundaries

Strongly ferroelectric perovskites, such as $BaTiO_3$ and $PbTiO_3$, possess permanent dipoles that are affected by mechanical strain and so are inherently piezoelectric. The response, however, is very small compared to the best piezoelectric materials, as mechanical stress applied to the crystal does not strongly affect the magnitude or direction of the dipole. Enhancing the piezoelectric response necessitates a more efficient way of modifying the dipole through, for example, dipole rotation.

The common ferroelectric symmetries: rhombohedral, orthorhombic, and tetragonal, have dipole orientations along different crystallographic orientations (<111>, <110>, and <100> respectively). While stress can be used to switch the structure between the symmetries and rotate the dipole, in systems such as $PbTiO_3$ the response is comparatively small due to the large forces necessary to transform the highly stable tetragonal structure into a different symmetry. However, the barrier to polarization rotation can be reduced by introducing compositional and structural disorder.

For many years it has been recognized that the highest piezoelectric responses are observed at the so-called morphotropic phase boundary (MPB). At this boundary multiple symmetries of the structure have almost equivalent energies and only small electrical or mechanical forces are necessary to switch between them.

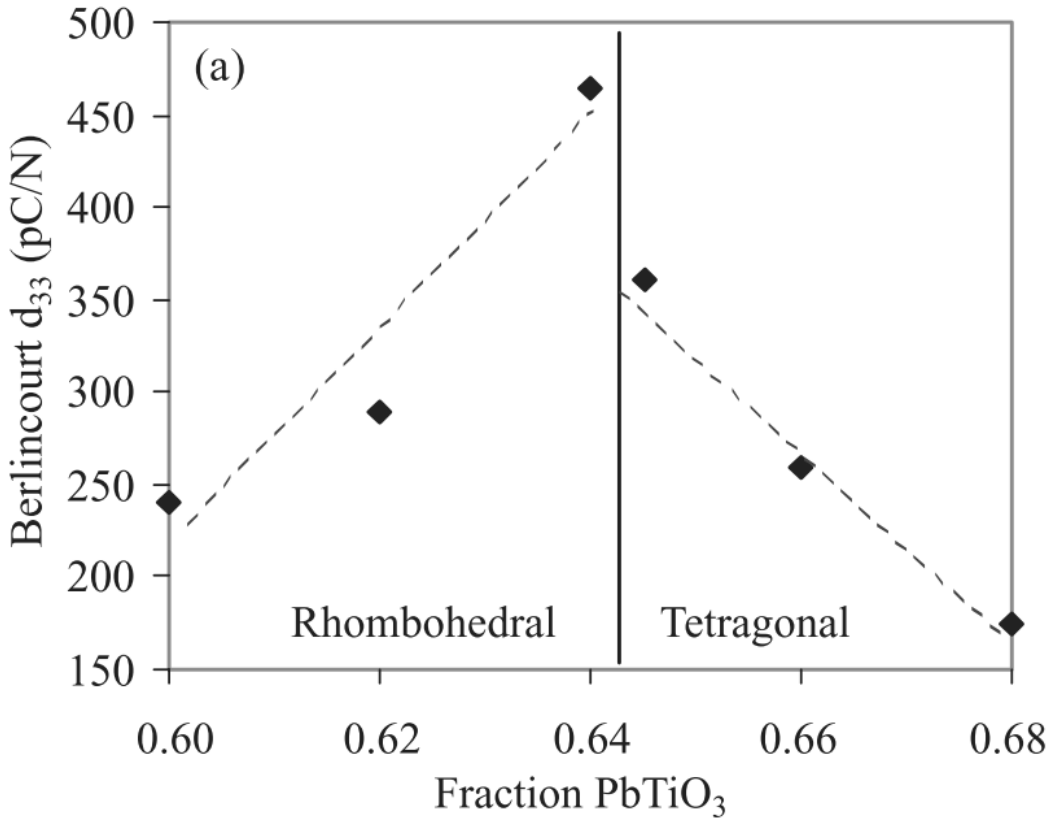

Figure 1.7: Piezoelectric response (d_{33}) as a function of fraction $PbTiO_3$ in the (x)$PbTiO_3$ - (1-x)$BiScO_3$ solid solution. Reproduced from [Eitel 2001]

The enhancement of the piezoelectric response at the MPB can be very significant compared to nearby compositions, as shown in Figure 1.7 for the PT-$BiScO_3$ system [Eitel 2001]. MPBs are found in solid-solutions where the different symmetries of the respective end-members are frustrated by the compositional disorder on the A- and B-site sub-lattice.

The introduction of cation disorder in these systems affects the structure in complex ways. For Pb(Zr,Ti)O_3 (PZT), small substitutions of Ti^{4+} into $PbZrO_3$ stabilize

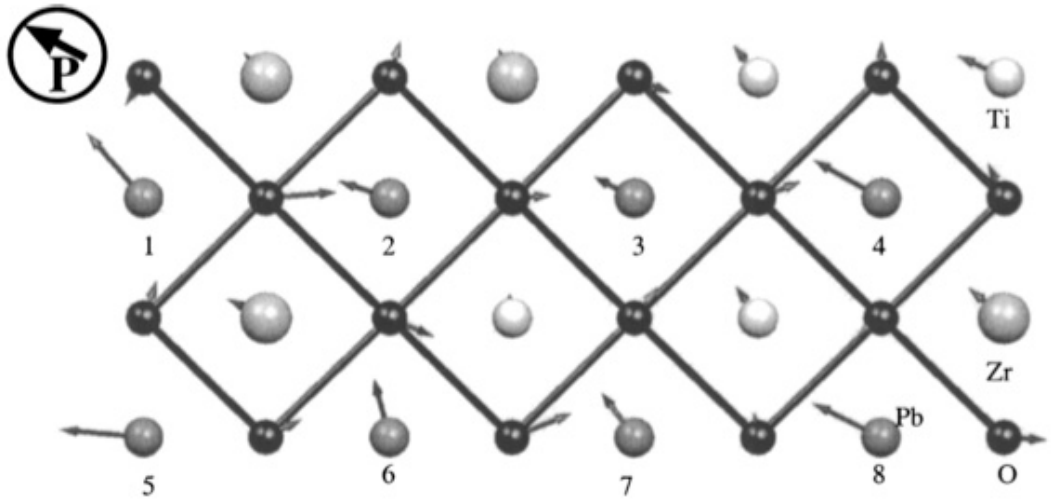

Figure 1.8: Projection of the structure of PZT in the XY plane. Arrows represent displacements from ideal perovskite positions. Reproduced from [Grinberg 2004 A]

a ferroelectric rhombohedral structure that persists up to the MPB composition ($Pb(Zr_{0.52}Ti_{0.48})O_3$). Although single-phase at the macroscopic level, the unit-cell level structure comprises the coexistence of the Ti-rich tetragonal and Zr-rich rhombohedral regions. The piezoelectric properties of PZT MPB compositions are enhanced further by the existence of a lower symmetry "bridge phase" which faciliate rotation of the polarization between the two structures that exist on either side of the boundary [Noheda 1999, Bellaiche 2000].

At an MPB the structure shows extensive local disorder and deviation from the average long-range structure [Dmowksi 2000]. Theoretical calculations suggest in PZT this is due to the Pb cations avoiding displacement towards the Zr cations (Figure 1.8) [Grinberg 2004 A].

The subtle ways in which the various bonding interactions compete with each other makes prediction of the structure and properties of new perovskite chemistries difficult without thorough and rigorous modeling. However, over the last decade advances in the first principles calculations of complex ferroelectrics have led to the successful identification of several new ferroelectric and piezoelectric systems. These calculations have been used to guide several aspects of the research in this work.

1.3.2 Lead- and Bismuth-containing perovskites

Lead based perovskite systems, based on PZT or relaxor systems such as $Pb(Mg_{2/3}Nb_{1/3})O_3$ are the dominant materials used in commercial piezoelectric systems [Swartz 1982]. While these systems have widespread applications, there is a need for new materials with increased T_C for high-temperature applications, and with increased polarization and piezoelectric constant for device miniaturization and enhanced sensitivity. Because they are based on lead containing materials there is also a strong motivation to identify systems that comply with recent environmental restrictions.

In 2003, the European Union adopted the Restriction of Hazardous Substances Directive (RoHS). This directive called for the elimination of certain hazardous substances, including lead, in products manufactured or sold in the EU. Thus far, lead-containing piezoelectric materials are exempt from this directive due to the lack of competitive replacement materials, but this exemption is subject to periodic review. In the United States, the state of California has passed legislation mirroring its EU counterpart, though no action has been taken at the federal level.

The most promising replacement for Pb in ferroelectric perovskites is Bi. The Bi^{3+} cation has the same 6*s* "lone-pair" electronic configuration responsible for the large ferroelectric distortion of Pb^{2+} and has the potential for enhanced properties due to its smaller ionic radius (1.36Å v. 1.49Å). While both cations have a large degree of covalency in their bonding with oxygen, the smaller ionic radius of Bi^{3+} can reduce the repulsive forces with neighboring cations, allowing for larger cooperative displacements. First principle calculations have also shown the stronger hybridization of the Bi^{3+} orbitals with oxygen induces larger off-centering and the properties of Bi-based perovskites have been predicted to be better than their Pb-based counterparts [Iniguez 2003, Baettig 2005].

The major impediment to the replacement of lead by bismuth in piezoelectric applications is the instability of many, if not most, Bi-based A-site perovskites. $BiFeO_3$, $Bi(Mn^{4+}_{1/3}Mn^{3+}_{1/2}Ni^{2+}_{1/3})O_3$, $Bi(Ti_{3/8}Fe_{2/8}Ni_{3/8})O_3$, and $Bi(Ti_{3/8}Fe_{2/8}Mg_{3/8})O_3$, are the only known pure Bi compositions that can be synthesized at ambient pressure in a single-phase perovskite structure [Filip'ev 1960, Hughes 2005, Bridges 2007]. Even these compositions are more susceptible to impurity formation issues than lead-based perovskites. Small deviations from the stable compositions, even while maintaining charge neutrality, result in multi-phase assemblages. Most other Bi-based "ABO_3" perovskite formulations are multi-phase when synthesized under ambient pressure, usually due to the formation of the $Bi_2B_2O_7$ pyrochlore structure. Therefore, most recent research on bismuth systems has focused on synthesis of thin films, high-pressure synthesis, or the use of mixed A-site solid solutions to stabilize the perovskite structure. High-pressure synthesis has been successful in stabilizing single-phase perovskite forms

of $BiMnO_3$, $BiCoO_3$, and $BiAlO_3$ whose existence was predicted by theoretical work [Atou 1999, Belik 2006 A, Belik 2006 B]. However, ceramics attainable only via high-pressure synthesis tend to decompose at moderate temperatures under ambient pressure conditions, which limits their commercial potential. High-pressure synthesis also does not lend itself to the high volume production required by industry. This thesis focuses on Bi-containing, mixed A-site solid solutions as a route for investigating the dielectric properties of Bi-based perovskites.

The central goal of this work is to increase the fundamental understanding of the conditions under which A-site driven ferroelectric bismuth-based oxides can be stabilized in the perovskite structure. The systems investigated sought to stabilize bismuth in novel Pb-containing and Pb-free solid solutions to enhance the properties and reduce the lead-content of ferroelectric and piezoelectric materials. Chapter 2 investigates a family of solid solutions between PT and $Bi(Zn_{3/4}W_{1/4})O_3$ (BZW), a novel additive predicted to exhibit enhanced tetragonality. The successful synthesis of PT-BZW and observation of enhanced tetragonality provided validation of an empirical model for prediction of new enhanced tetragonality high *c/a* perovskites. Chapter 3 describes studies aimed towards stabilizing enhanced tetragonality in lead-free systems. Solid solutions between $Bi(Zn_{1/2}Ti_{1/2})O_3$ (BZT) and a variety of lead-free perovskite systems are investigated in an attempt to stabilize tetragonalities and polarizations similar to PT. Chapter 4 focuses on a series of investigations of MPB formation in the high *c/a* Bi-based perovskites. Ternary systems between PT, an enhanced tetragonality additive such as BZT, and a Bi-based MPB-forming additive such as $Bi(Mg_{1/2}Ti_{1/2})O_3$ are explored. The observation of

unusual multiple dielectric transitions in these systems stimulated a series of studies to characterize the structural changes accompanying the dielectric transitions. This chapter also includes investigation of other Bi-containing tetragonality enhancing and MPB-forming additives and introduces a predictive empirical model based on crystal-chemical parameters. A summary of the work performed and knowledge gained in the course of this work is provided in chapter 5, together with proposals for future work.

1.4 Experimental Procedures

1.4.1 Synthesis and sample preparation

All of the systems discussed in this work were synthesized and characterized using standard experimental techniques. This section will explain the experimental procedures common to all the samples, leaving specific details unique to a specific system for the appropriate section.

The solid state synthesis method utilizes standard reagent-grade oxide and carbonate powders. A table of the suppliers and grades of the precursors is given in Table 1.2.

The precursor powders were dried at appropriate temperatures prior to their use to remove absorbed moisture. Stoichiometric mixtures of the precursor materials were mixed by ball milling for no less than 2h in ethanol with yttrium-stabilized ZrO_2 grinding media. After removing the ethanol through the application of moderate heat, the mixed precursor powders were calcined in alumina crucibles in air at atmospheric pressure. After initial calcination the resulting powders were ground by hand under ethanol with a mortar and pestle to prepare the powder for further processing or characterization. Typically multiple calcination steps were required to achieve single phase samples. For certain systems, the columbite synthesis method was required. In this method, stoichiometric mixtures of the precursor powders corresponding to the B-site cations were calcined separately from the A-site precursor powders and then mixed afterwards.

Table 1.2: Table of suppliers and grades of the starting precursor materials used in the synthesis of systems investigated in this work.

Material	*Supplier & Grade*	*Material*	*Supplier & Grade*
Ag_2O	Fisher 99%	NiO	Aldrich 99.99%
$Ba(CO)_3$	Cerac 99.9%	PbO	Cerac 99.95%
Bi_2O_3	Cerac 99.99%	Sc_2O_3	Cerac 99.99%
CuO	J. T. Baker 99.9%	$Sr(CO)_3$	Cerac 99.5%
Fe_2O_3	Cerac 99.95%	TiO_2	Cerac 99.95%
$K_2(CO)_3$	J. T. Baker 99.9%	WO_3	Cerac 99.99%
MgO	Cerac 99.9%	ZnO	Cerac 99.995%
$Na_2(CO)_3$	J.T. Baker 99.8%	ZrO_2	Cerac 99.95
Nb_2O_5	Cerac 99.95%		

Calcination temperatures varied from 600°C to 1100°C for lead-containing systems and up to 1350°C for lead-free systems. System specific temperatures are described in the appropriate section.

Pellets of single-phase calcined samples were formed using a die and uniaxial press for dielectric measurement. To improve the quality and ultimate density of the pellets, pellets taken from the die were then isostatically pressed at 550MPa prior to sintering. Sintering temperatures varied by composition, but generally were within the 1000°C to 1200°C range. To minimize the volatilization of Pb and Bi, pellets containing these species were buried in a sacrificial powder of the same composition inside the alumina crucible. Single phase pellets were sintered until their relative density had achieved at least 90% of theoretical maximum. Sample pellets were then cut with a diamond blade rotary saw to an appropriate thickness and rough polished with 400 grit polishing paper to obtain parallel top and bottom surfaces. Electrodes were applied to the

pellet by coating the surfaces with silver paint (Heraeus ST1601-14 type). Paint was dried and sintered at 750°C to provide a dense electrical contact. Platinum lead wires, necessary for dielectric characterization, were attached using the same silver paint. Electrical characterization samples without platinum lead wires had their silver electrodes rough polished with 400 grit polishing paper to ensure proper electrical contact.

1.4.2 Sample characterization

X-ray diffraction (XRD) was used to determine the phase content and structure of sample powders and pellets. Sample powders were affixed to frosted microscrope slides for insertion into the diffractometer. Room temperature patterns were collected on a Rigaku DMax B diffractometer using Cu K_α radiation generated at 45 kV and 30 mA. Most data was collected as a continuous scan using scan speeds of 2-3 °/min. Lattice parameters were calculated by the CELREF software using a least-squares refinement method.

High temperature laboratory XRD scans were obtained on a Siemens D500 X-ray Diffractometer using Cu K_α radiation generated at 40 kV and 40 mA. Data was collected as a continuous scan using a scan speed of 3 °/min. Samples were loaded onto the platinum heating strip and the temperature monitored by a thermocouple attached to the platinum strip. Lattice parameters were also calculated by the CELREF software using a least-squares refinement method. Certain patterns were also analyzed using the Rietveld refinement technique by the GSAS+EXPGUI package [Larson 2000, Toby 2001].

Selected compositions described in chapter 4 required more detailed structural data at elevated temperature. These samples were studied by neutron and synchrotron diffraction to obtain temperature dependent structural data. Neutron powder diffraction (NPD) data were collected under ambient pressure and varying temperature using the BT-1 32 detector neutron powder diffractometer at the NIST Center for Neutron Research. A Cu(311) monochromator with a 90° takeoff angle, λ = 1.5405 Å, and an in-pile collimation of 15 min of arc were used. Samples were loaded in a vanadium cylinder container with a stainless steel lid. Data were collected over the range 3-165° 2θ with a step size of 0.05°. Rietveld structural refinements were conducted using the GSAS+EXPGUI package.

High resolution synchrotron powder diffraction data were collected using beamline 11-BM at the Advanced Photon Source (APS), Argonne National Laboratory using an average wavelength of 0.41363 Å. Discrete detectors covering an angular range from -6 to 16 º 2θ wre scanned over a 34º 2θ range, with data points collected every 0.001º 2θ and scan speed of 0.01º/s.

The 11-BM instrument uses x-ray optics with two platinum-striped mirrors and a double-crystal Si(111) monochromator, where the second crystal has an adjustable sagittal bend [Wang 2008]. Ion chambers monitor the incident flux. A vertical Huber 480 goniometer, equipped with a Heidenhain encoder, positions an analyzer system comprised of twelve perfect Si(111) analyzers and twelve Oxford-Danfysik $LaCl_3$ scintillators, with a spacing of 2º 2θ [Lee 2008]. A three-axis translation stage holds the sample mounting and allows it to be spun, typically at ~5400 RPM (90 Hz). A Mitsubishi

robotic arm was used to mount and dismount samples on the diffractometer [Preissner 2009].

The diffractometer is controlled via EPICS and data were collected while continually scanning the diffractometer 2θ arm [Dalesio 1994]. A mixture of NIST standard reference materials, Si (SRM 640c) and Al_2O_3 (SRM 676) were used to calibrate the instrument, where the Si lattice constant determines the wavelength for each detector. Corrections were applied for detector sensitivity, 2θ offset, small differences in wavelength between detectors, and the source intensity, as noted by the ion chamber before merging the data into a single set of intensities evenly spaced in 2θ.

Dielectric properties above room temperature were measured as a function of frequency (100 Hz to 1 Mhz) and temperature using a high-precision impedance-capacitance-resistance meter (Hewlett-Packard Model 4284A) and a high temperature thermal chamber. The sample temperature was monitored by an S-type thermocouple positioned near the pellet. Low temperature dielectric properties were obtained using the same LCR meter and a Delta 9023 thermal chamber. Hysteresis measurements of electric field versus polarization were performed via the Radiant RT66A Ferroelectric Test System interfacing with an RT66A USB interface to utilize the Vision software package. Piezoelectric testing was conducted in collaboration with Professor Wei-Heng Shih of Drexel University.

Thermal analysis, via Differential Scanning Caliometry (DSC), was performed on a Perkin-Elmer model computer controlled instrument. Scans were performed under ambient atmospheric conditions with heating and cooling rates of 5-20°C/min with the samples loaded into standard aluminum cans.

Chapter 2:

Enhanced Tetragonality Systems: $PbTiO_3$-$Bi(Zn_{3/4}W_{1/4})O_3$

2.1 Introduction

Bi-containing perovskites have been known since at least the 1960s, though very few stable single-phase Bi^{3+} end-members are known. For the rest of the century, Pb-based systems dominated piezoelectric research because of their stability and excellent properties, particularly in $Pb(Zr,Ti)O_3$-type systems.

A resurgence in interest in bismuth for piezoelectric applications occurred a decade ago when empirical correlations were developed to relate the tolerance factor of end-members forming solid solutions with $PbTiO_3$ to the Curie temperature at the MPB [Eitel 2001]. It was shown that a lower tolerance factor for the non-PT end-member correlated with a higher T_C at the MPB for the resultant solid solution system. Because Bi^{3+} has a smaller ionic radius than Pb^{2+}, it was predicted that lower tolerance factor Bi-containing additives could produce higher T_C MPB ferroelectrics. Using this correlation, a new family of $BiScO_3$-substituted lead titanate solid solutions were discovered with a T_C of 450°C at the MPB composition (36% $BiScO_3$), significantly higher than the PZT system (385°C). Following that work other Bi^{3+} end-members in the $Bi(B^{2+}_{1/2}B^{4+}_{1/2})O_3$ perovskite family were investigated and, for example, the substitution of $Bi(Mg_{1/2}Ti_{1/2})O_3$

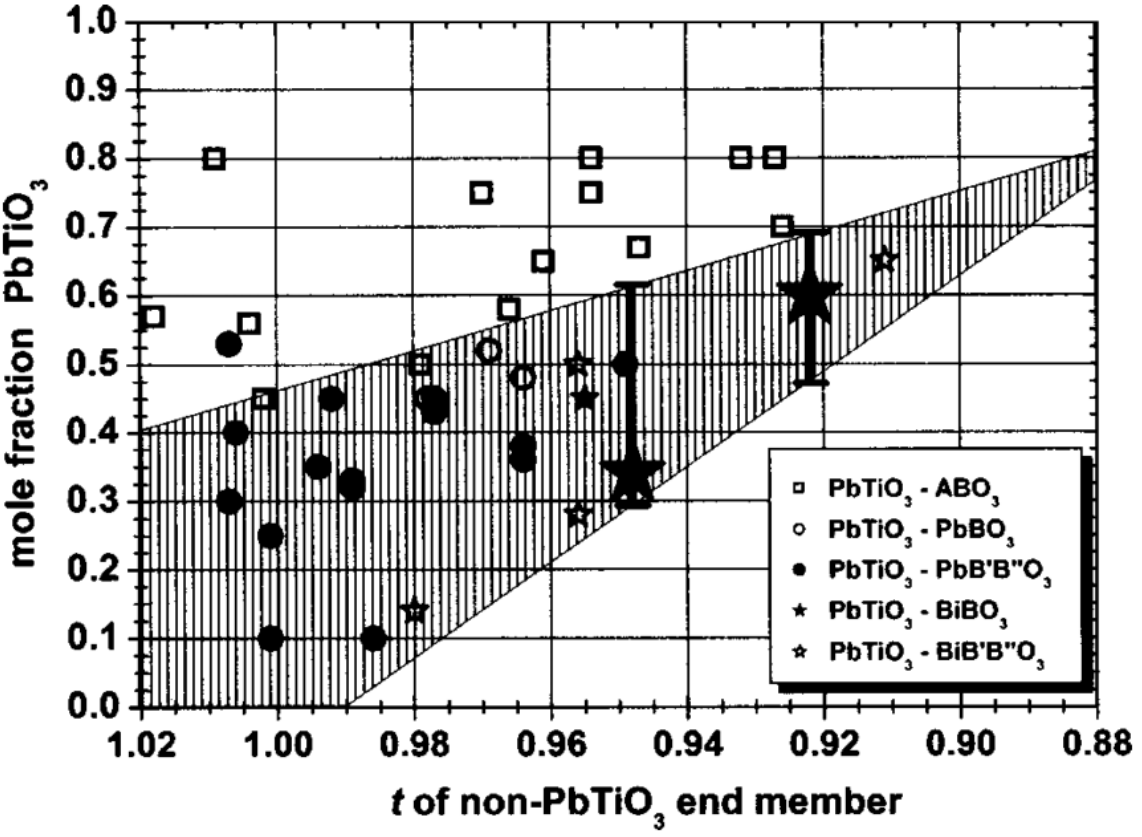

Figure 2.1: Plot of the compositional position (in mole fraction $PbTiO_3$) of the MPB vs the end member (*t*) in $PbTiO_3$ based solid solution systems. Reproduced from [Suchomel 2004]

(BMT) into PT yielded a MPB composition (63% BMT) with a T_C (425°C) approaching the PT-$BiScO_3$ system [Suchomel 2004].

This later work was guided by a new series of correlations (Figure 2.1) relating the composition of the MPB in $PbTiO_3$-based solid solution systems to the tolerance factor of the non-$PbTiO_3$ end-member. This work demonstrated the composition of the MPB becomes increasingly PT-rich as the tolerance factor of the additive is reduced. The resultant increase in T_C is therefore associated with the proximity of the MPB to PT.

These correlations also led to the subsequent identification of other high T_C systems such as PT-$Bi(Mg_{1/2}Zr_{1/2})O_3$.

Although these empirical correlations enabled the design of new high T_C MPB systems, they suggest the Curie temperature could not exceed that of pure PT (490°C). However, in 2005, Suchomel and Davies discovered that certain Bi-based additives produced unexpected large and sustained increases in the tetragonality and T_C [Suchomel 2005]. One such additive, $Bi(Zn_{1/2}Ti_{1/2})O_3$ (BZT), enhanced the T_C of PT to above 700°C at its solubility limit (40% BZT). The *c/a* ratio correspondingly increased to a maximum of 1.11. First principles calculations suggest this "enhanced tetragonality" behavior is induced by Bi^{3+} and Zn^{2+} cation displacements that exceed those of Pb^{2+} and Ti^{4+} [Grinberg 2007].

The observation of enhanced tetragonality behavior was surprising, as it stands in contrast to most additives to PT and was not predicted by existing correlations. The tolerance factor of BZT is similar to the MPB-forming BMT additive (0.942 v. 0.946) and existing correlations predicted similar behavior.

Prior to the discoveryof BZT, only two systems had been reported to increase the *c/a* of PT: $BiFeO_3$ and $Bi(Zn_{2/3}Nb_{1/3})O_3$ [Fedulov 1961, Nomura 1982]. The PT-$BiFeO_3$ system exhibits complete solubility; the MPB is formed at (0.34)PT – (0.66)$BiFeO_3$ and the *c/a* of the tetragonal phase at the MPB is ~1.17. However, like most Fe-containing perovskites, this system is unsuitable for ferroelectric applications because of high relative conductivity. The PT-$Bi(Zn_{2/3}Nb_{1/3})O_3$ system was also reported to exhibit high conductivity as well as a solubility range that limits the maximum *c/a* ratio to 1.08. Small

increases in tetragonality have also been reported in the PT-$BiInO_3$ and PT-$BiYbO_3$ systems, however the solubility is limited and neither system exhibited the sustained increases in the tetragonality observed in PT-BZT [Eitel 2001, Duan 2004].

Compared to the other additives capable of enhancing the tetragonality of PT, BZT possesses the best combination of high solubility, low conductivity, and high T_C. The discovery of BZT also provides strategies for stabilizing new perovskites with enhanced tetragonalities. While cation radii data and tolerance factor are sufficient to predict the position of an MPB for those additives that reduce the *c/a* of PT, they are not effective in rationalizing the increase in T_C and *c/a* in BZT. It was clear that new crystal-chemical parameters were necessary to understand the behavior of that system. It was proposed that the average displacement magnitude of the B-site (d^0_b) was critical in understanding the behavior of BZT.

First principles calculations predict high *c/a* ratios in Bi-containing systems where B-site cations cooperatively displaced to minimize repulsions between cations [Baettig 2005]. BZT is fully occupied by B-site cations that are known to strongly displace whereas MPB-forming additives such as $BiScO_3$ and BMT are not [Grinberg 2007]. The contrasting behavior of these additives suggests that enhanced tetragonality is induced by B-sites that are fully-occupied by strongly ferroelectrically-active cations. In this work, another additive with full B-site occupancy of ferroelectrically-active cations, $Bi(Zn_{3/4}W_{1/4})O_3$ (BZW), was designed and its behavior was compared to its Mg-containing counterpart: $Bi(Mg_{3/4}W_{1/4})O_3$. The results of this chapter were published in 2006 [Stein 2006].

2.2 Investigation of $PbTiO_3$-$Bi(Zn_{3/4}W_{1/4})O_3$ system

Samples of the (x)PT - (1-x)BZW solid solutions were prepared by the methods detailed in Chapter 1. Compositions near the solubility limit were prepared using a modified method involving pre-reaction of the oxides of the B-site components (Ti, Zn, W), known as the columbite method. Stoichiometric mixtures of the starting B-site reagents were ball-milled in ethanol with YSZ zirconia balls for 5 hours. To avoid impurities at compositions with x = 0.85 and x = 0.80 the titanium, zinc and tungsten containing reagents were calcined at 1100°C prior to the addition of the lead and bismuth components. Calcination temperatures for the combined system were between 850°C and 1100°C. After forming the pellets in the usual manner, they were sintered for 5 hours between 1000°C and 1100°C depending on the composition. Powder x-ray diffraction (XRD) patterns of calcined powders were recorded in the 2θ scan range of 15° - 60°; lattice parameters were calculated via the least-squares method using CELREF. Ferroelectric phase transition temperatures were monitored by differential scanning calorimetry (DSC) at heating and cooling rates of 10°C/min from 350°C to 700°C. Dielectric properties were investigated using the method detailed in Chapter 1.

The room temperature XRD scans for selected compositions in the (x)PT - (1-x) BZW system in Figure 2.2 indicate that a single phase tetragonal perovskite region exists between $1.0 \geq x > \sim 0.80$; for lower values of x the patterns contained additional peaks associated with pyrochlore-related impurity phases. Similar to the PT-BZT system, the enhanced tetragonality of the BZW-containing solid solution was clearly exhibited by the increased splitting of the {200} reflections. Figure 2.3 highlights the change in the lattice

parameters, as well as the *c/a* ratio, for the substitution of BZW into PT. The enhanced tetragonality, which reaches ~1.08 for $x = 0.8$, is associated with an increase in the *c*-lattice parameter, while the *a*-parameter decreases slightly across the solid solution. The molar volume increases with the concentration of BZW consistent with the increase in the average radius of the B-site cations ($\{0.75r(Zn^{2+}) + 0.25r(W^{6+})\} = 0.705$Å, $r(Ti^{4+}) = 0.605$Å). Compared to PT-BZT, the PT-BZW system shows a similar increase in *c/a* for equal substitution, but with a much more limited range of solid solubility. The effect of BZW on the structure of $PbTiO_3$ should be contrasted to the behavior of its magnesium counterpart, $Bi(Mg_{3/4}W_{1/4})O_3$, which has similar crystal-chemistry (cation radius and tolerance factor) but reduces the tetragonality of $PbTiO_3$.

Dense sintered pellets of all compositions with $x<0.95$ were obtained by using slow heating and cooling rates through the ferroelectric-paraelectric transition to avoid strain induced cracking. Dielectric data was obtained at various frequencies between 100Hz and 1MHz; no evidence for frequency dispersion was observed and the 100kHz data is used in the plot of the temperature dependence of the real part of the permittivity in Figure 2.4. Consistent with the enhancement in tetragonality, the T_C of PT increases with BZW substitution, though the limited solubility prevents the gains from being more than moderate (~ 525°C for 20% substitution). Similar to the PT-BZT system there is an increasing thermal hysteresis with BZW substitution, likely due to the kinetics of the nucleation and growth of the highly distorted tetragonal phase [Suchomel 2005].

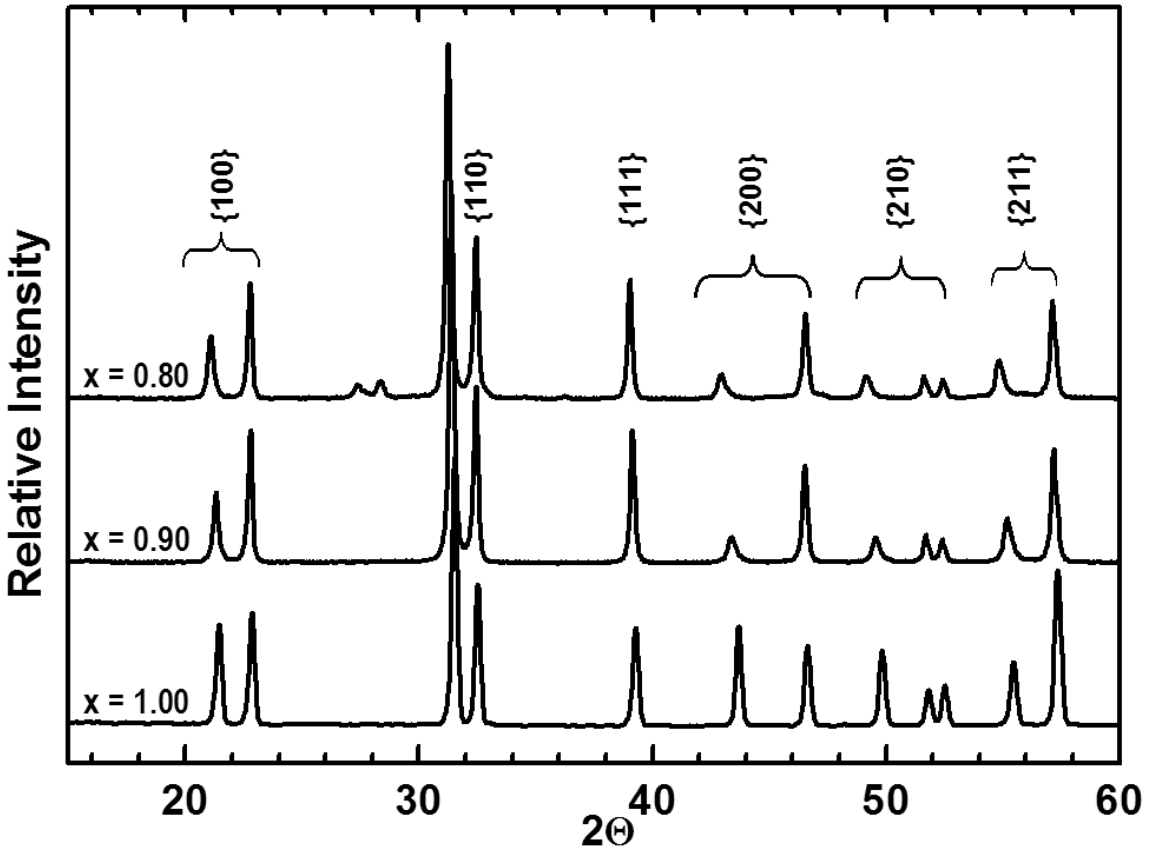

Figure 2.2: XRD patterns of compositions in the $(x)PbTiO_3$ - $(1\text{-}x)Bi(Zn_{3/4}W_{1/4})O_3$ system. Enhanced tetragonality is highlighted by increased {200} splitting.

DSC data was used to corroborate the T_c data from the dielectric measurements and to obtain data for compositions with higher *x* that could not be sintered. The combined dielectric and DSC data for T_c is shown as a function of BZW substitution in Figure 2.5. The plotted points reflect the average T_c values and the error bars represent the extent of the thermal hysteresis. For the largest substitution of BZW, there is an increase in T_C of 30-40°C, depending on the measurement technique. While the rate of increase of the *c/a* ratio with substitution of PT is nearly equal in both the PT-BZT and PT-BZN systems,

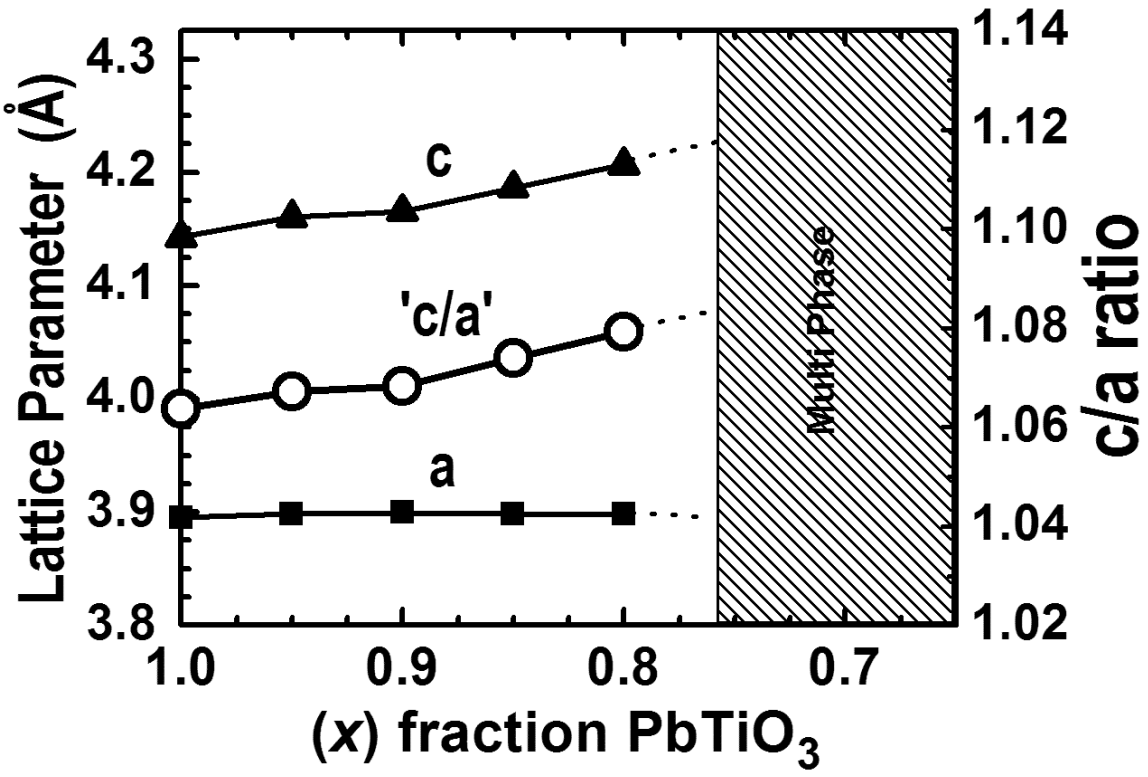

Figure 2.3: Lattice parameters and '*c/a*' ratio as a function of composition in the $(x)PbTiO_3$-$(1-x)Bi(Zn_{3/4}W_{1/4})O_3$ (PT-BZW) system.

the rate of increase of T_C is smaller for PT-BZW, illustrating that the Curie temperature is a function of the specific chemistry and ionic displacements and not just the structure. To further illustrate this point, the enhancements in tetragonality and T_C of $Bi(Zn_{3/4}W_{1/4})O_3$, $Bi(Zn_{1/2}Ti_{1/2})O_3$, $BiFeO_3$ and $Bi(Zn_{2/3}Nb_{1/3})O_3$ lead titanate solid solutions are compared in Figure 2.6. Although the range of solubility in PT-$BiFeO_3$ is complete, and $BiFeO_3$-rich compositions induce formation of an MPB and a rhombohedral phase region, the rate of increase of *c/a* with replacement of PT is much

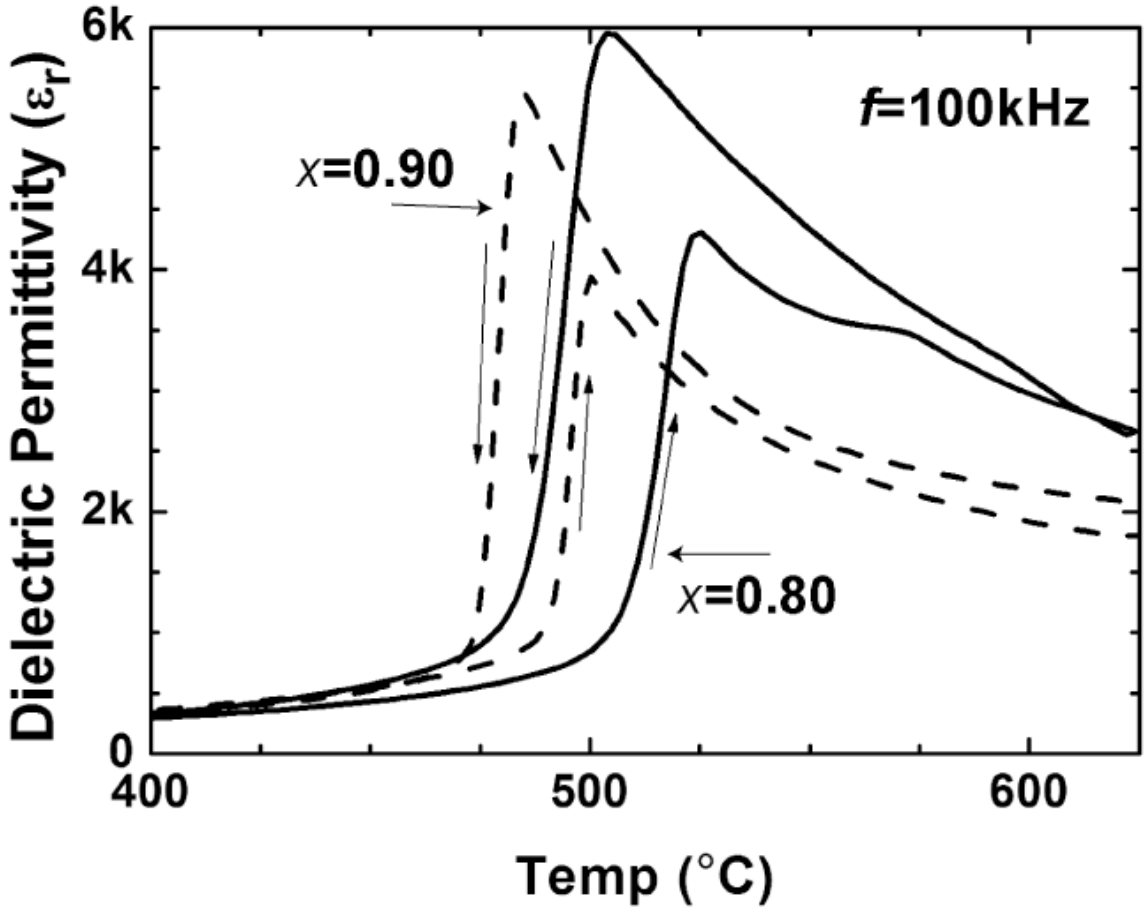

Figure 2.4: Dielectric permittivity (ε_r) vs. temperature in the (x)$PbTiO_3$-(1-x)$Bi(Zn_{3/4}W_{1/4})O_3$ system (f = 100kHz). Arrows indicate direction of thermal ramp.

higher in the BZT- and BZW-containing systems. It is believed to be due to the larger B-site displacements and increased cooperative Bi/B-site coupling for the [Zn,Ti] and [Zn,W,(Ti)] combinations. The data in this figure also reinforce the absence of a direct correlation between the actual magnitude of *c/a* and T_c with the increase in the latter being higher for the Zn-based systems, again presumably because of larger ionic displacements on the B-site. Figure 2.6 also includes a limited selection of data for

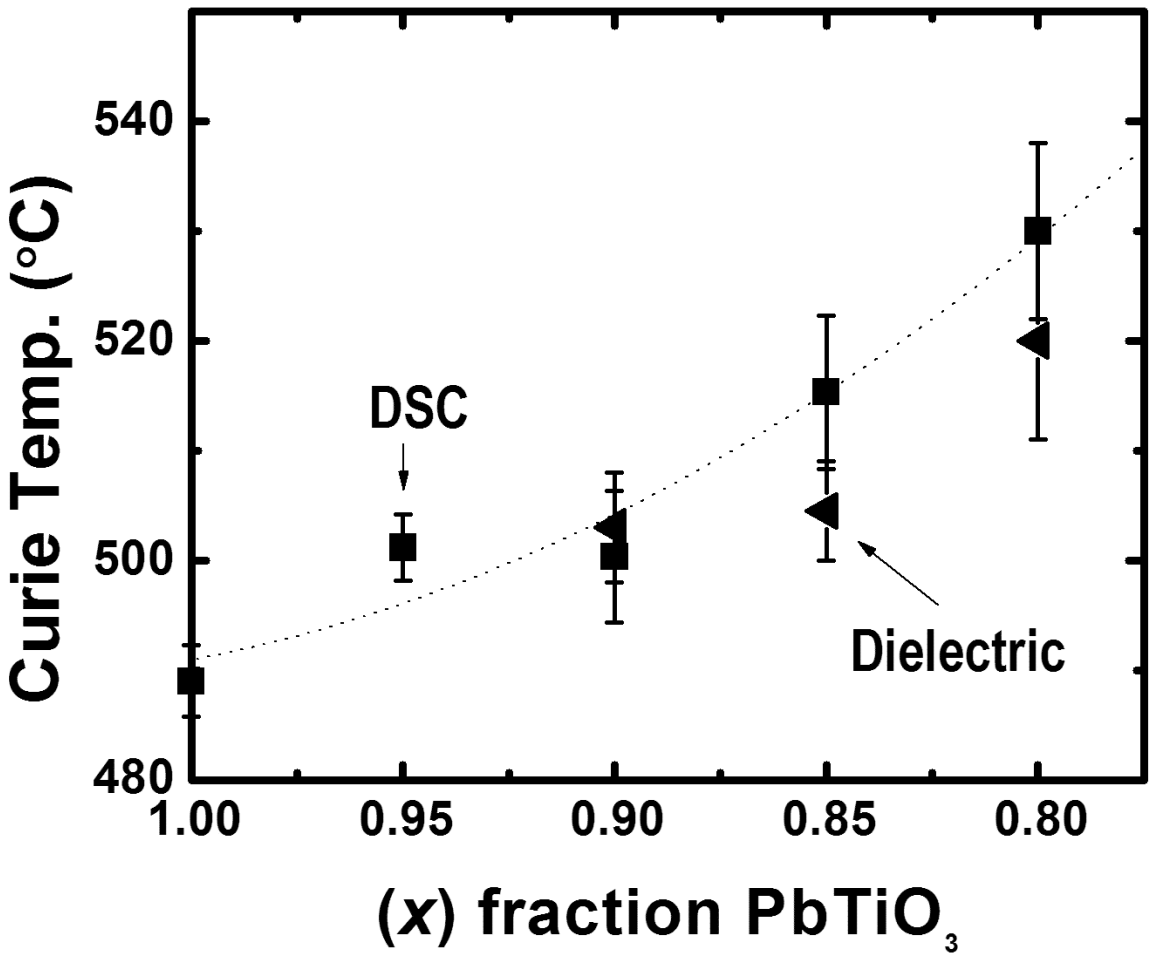

Figure 2.5: Compositional dependence of Curie temperature (T_C) in the (x)$PbTiO_3$ - (1-x)$Bi(Zn_{3/4}W_{1/4})O_3$ system. The dotted line is a polynomial fit of the average T_C values, as measured by DSC.

additives that exhibit "normal" behavior and reduce the tetragonality to induce an MPB; in particular $BiScO_3$ and the Mg- containing $Bi(Mg_{3/4}W_{1/4})O_3$, $Bi(Mg_{1/2}Ti_{1/2})O_3$ systems [Eitel 2001, Suchomel 2004, Stringer 2005]

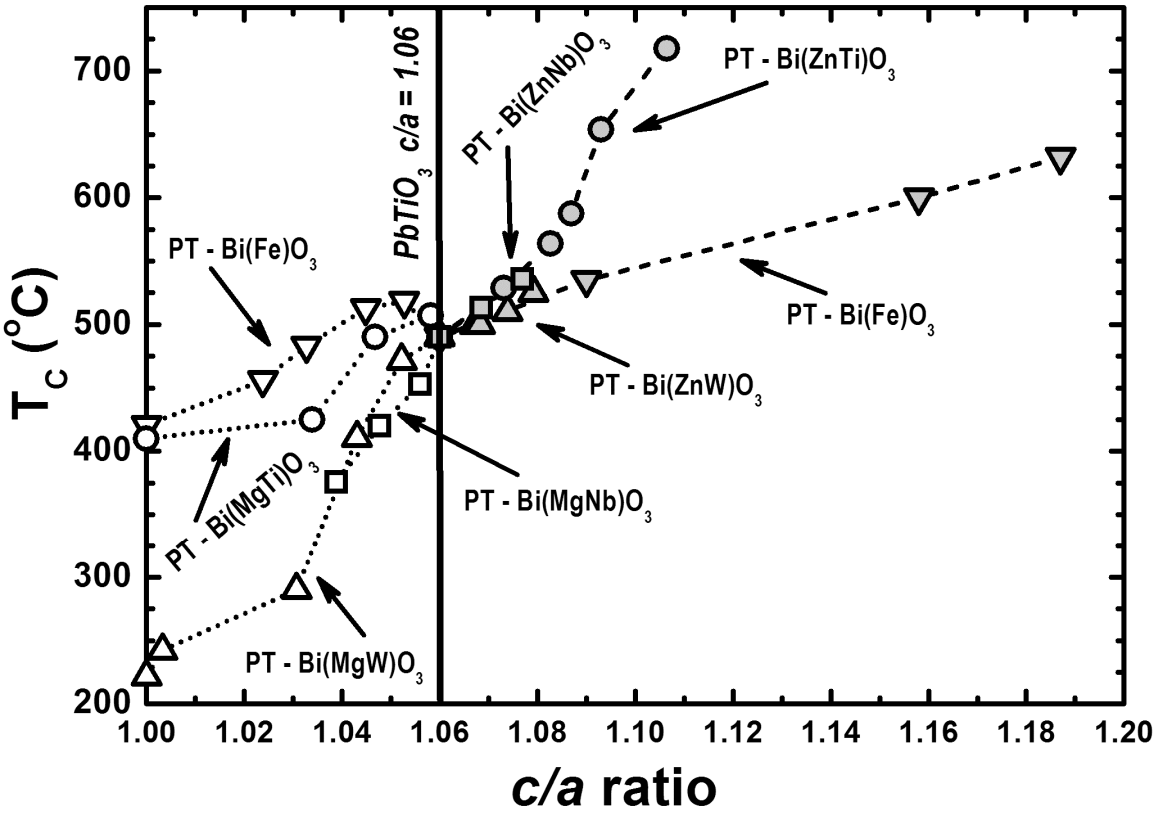

Figure 2.6: Dependence of the Curie temperature (T_C) on the *c/a* ratio in various $(x)PbTiO_3$-$(1-x)Bi(B'B'')O_3$ systems. Right hand panel contains systems with enhanced tetragonality, left hand panel systems with reduced tetragonality.

2.3 Conclusions

The identification of $Bi(Zn_{3/4}W_{1/4})O_3$ as a new tetragonality enhancing additive to $PbTiO_3$ allowed clarification of the crystal chemical criteria required to increase the *c/a* of $PbTiO_3$. While the biggest driver of this behavior is the partial occupancy of the A-site by Bi^{3+}, the enhanced tetragonality can only be stabilized when the B-site is occupied by cations capable of undergoing large cooperative displacements to minimize the Bi^{3+} - B-cation repulsive forces.

In addition to $Bi(Zn_{3/4}W_{1/4})O_3$, $Bi(Zn_{1/2}Ti_{1/2})O_3$, $BiFeO_3$, and $Bi(Zn_{2/3}Nb_{1/3})O_3$ are the only substituents known to increase the *c/a* of $PbTiO_3$. In each case the B-site lattice contains high levels of ferroelectrically-active cations. In contrast, additives such as $BiScO_3$, where Sc^{3+} has a low d^0 value, destabilize the tetragonal phase. The activity of $Bi(Zn_{3/4}W_{1/4})O_3$ is due to the high concentration of Zn^{2+}. Typically, W^{6+} displacements do not arise from hybridization of the valence *d*-orbitals and anion 2*p* orbitals and are due almost entirely to its small ionic radius. Despite this limitation, BZW is able to substitute into PbTiO and enhance the tetragonality of the crystal as well as the Curie temperature, though with less solubility than BZT.

The next chapter explores the potential of these additives in enhancing the tetragonality of lead-free perovskite end-members.

Chapter 3:

Lead-free Systems

3.1 Introduction

The discovery of PT-BZT and the subsequent synthesis of the PT-BZW system provides a rational strategy for enhancing the tetragonality of lead titanate. This chapter explores whether these additives can be used to stabilize larger tetragonalities in a lead-free perovskite.

The large displacement of Pb^{2+} cations are responsible for the excellent ferroelectric and piezoelectric properties of PZT and related systems. While lead-free perovskites can also exhibit piezoelectric properties, their performance is considerably lower as they are primarily B-site driven, and the displacements of even the most ferroelectrically-active B-site cations, Ti^{4+} and Zn^{2+}, are significantly less than Pb^{2+} (d^0 = 0.25Å v. 0.45Å). The introduction of Bi^{3+} would potentially allow the A-sublattice to contribute to the piezoelectric performance of these materials, but only if those displacements can correlate in a manner that stabilizes a ferroelectric symmetry.

The systems investigated were designed to maintain full occupancy of the B-site by strongly ferroelectrically-active cations, which in the last chapter was shown to be critical in enabling the enhanced tetragonality of the Pb-Bi perovskites described earlier. To seek high tetragonality in a lead-free framework the $PbTiO_3$ component was replaced by $BaTiO_3$, $(K_{1/2}Bi_{1/2})TiO_3$, $(Na_{1/2}Bi_{1/2})TiO_3$, and $(Na_{1/2}K_{1/2})NbO_3$.

3.2 Results

3.2.1 $BaTiO_3$-$Bi(Zn_{1/2}Ti_{1/2})O_3$

Barium Titanate ($BaTiO_3$) is perhaps the best known lead-free ferroelectric perovskite with a T_C of 120°C and a spontaneous polarization of 0.15 C/m^2 [Kingery 1976]. At room temperature $BaTiO_3$ has a B-site driven ferroelectric tetragonal symmetry but other symmetries are stablized at lower temperatures. The decreased T_C and smaller *c/a* relative to $PbTiO_3$ is directly attributable to the inability of 5*p* Ba^{2+} orbitals to hybridize with the O^{2-} 2*p* orbitals in stabilizing an A-site ferroelectric distortion [Cohen 1992].

Compositions in the $(1-x)BaTiO_3 - (x)Bi(Zn_{1/2}Ti_{1/2})O_3$ solid solution were synthesized using standard solid state techniques at temperatures between 800°C and 1000°C. The XRD patterns for the synthesized compositions are plotted in Figure 3.1. Single-phase XRD patterns were obtainable only for the $x = 0.2$ composition and pure $BaTiO_3$. Nonetheless, a slight shift in the perovskite peak positions is noticeable for $x = 0.3$ relative to $x = 0.2$ composition, indicating that the solubility limit for BZT into $BaTiO_3$ falls somewhere between the two. The structure for both BZT-containing compositions is pseudocubic (possibly rhombohedral), as evidenced by the lack of the peak splitting observed in the pure $BaTiO_3$ pattern. No evidence was found for the formation of a structure with enhanced tetragonality.

The dielectric behavior of the $x = 0.2$ composition was investigated and is shown in Figure 3.2. The addition of BZT to $BaTiO_3$ introduces a strong relaxor characteristic to

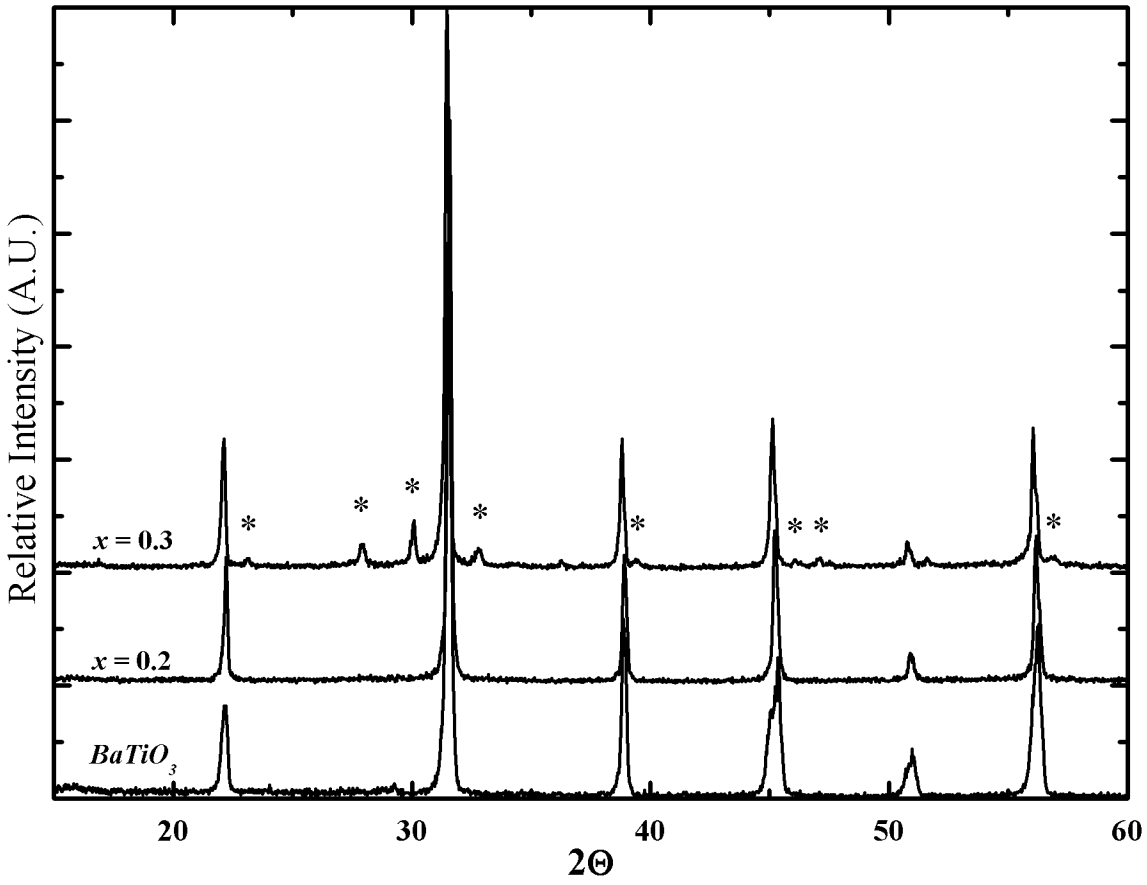

Figure 3.1: XRD patterns of compositions in the (1-x)$BaTiO_3$ – (x)$Bi(Zn_{1/2}Ti_{1/2})O_3$ solid solution. Starred peaks in the x = 0.3 composition indicate impurities. Tetragonal peak splitting in the pure $BaTiO_3$ pattern is indicated by significant peak broadening.

the dielectric response. The relatively sharp dielectric peak centered around the Curie temperature (120°C) in pure $BaTiO_3$ is transformed with modest BZT substitution into a broad, frequency-dependent peak between 90°C and 175°C. The increase in the permittivity at higher temperatures (>350°C) and associated increase in the dielectric loss (Figure 3.3) is believed to originate from an increase in the conductivity of the sample.

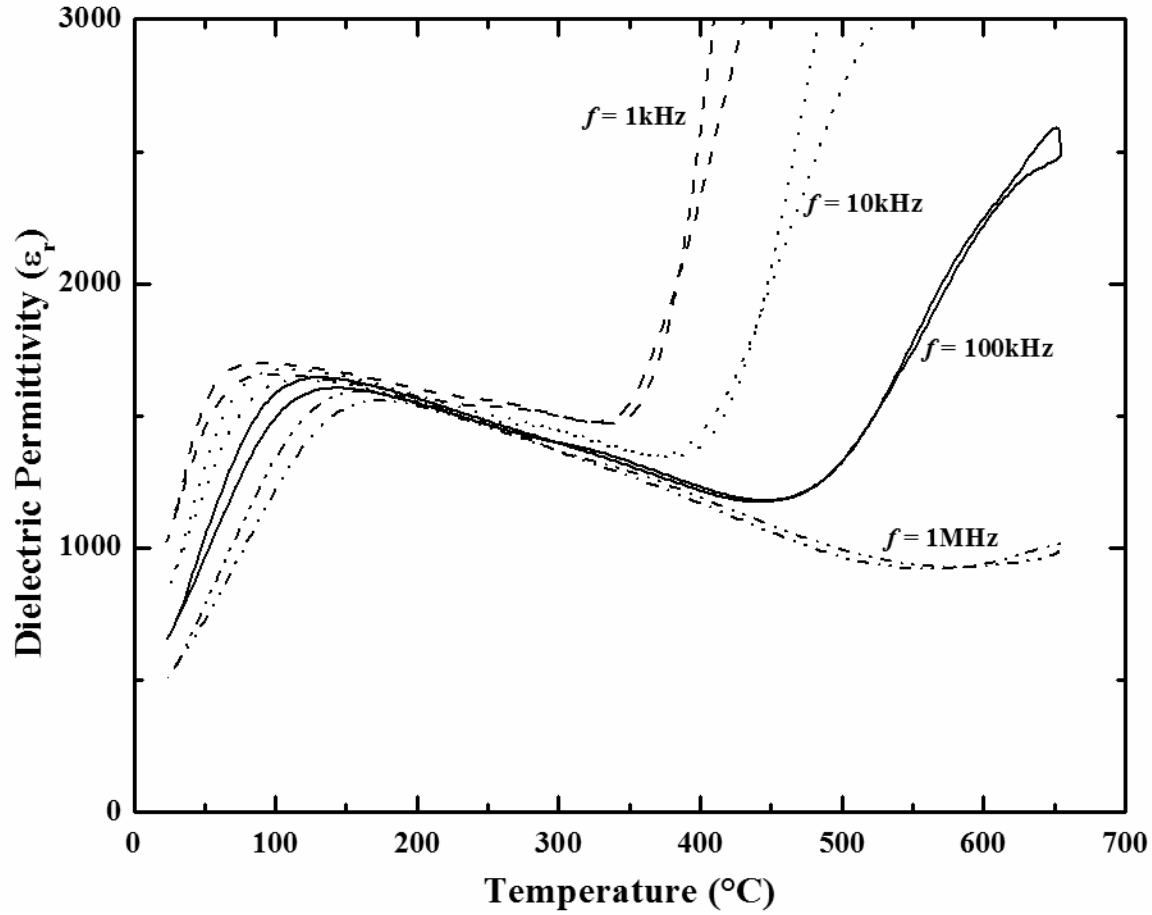

Figure 3.2: Dielectric response as a function of frequency and temperature for $(0.8)BaTiO_3$-$(0.2)Bi(Zn_{1/2}Ti_{1/2})O_3$.

The $BaTiO_3$-BZT system appears to be unable to allow correlation of the displacements of the substituted Bi^{3+} cations. At these low BZT substitution levels, the large and immobile Ba^{2+} cations presumably suppress the correlation of Bi^{3+} displacements, and the exploration of higher Bi^{3+} contents is restricted through the formation of multiple secondary phases.

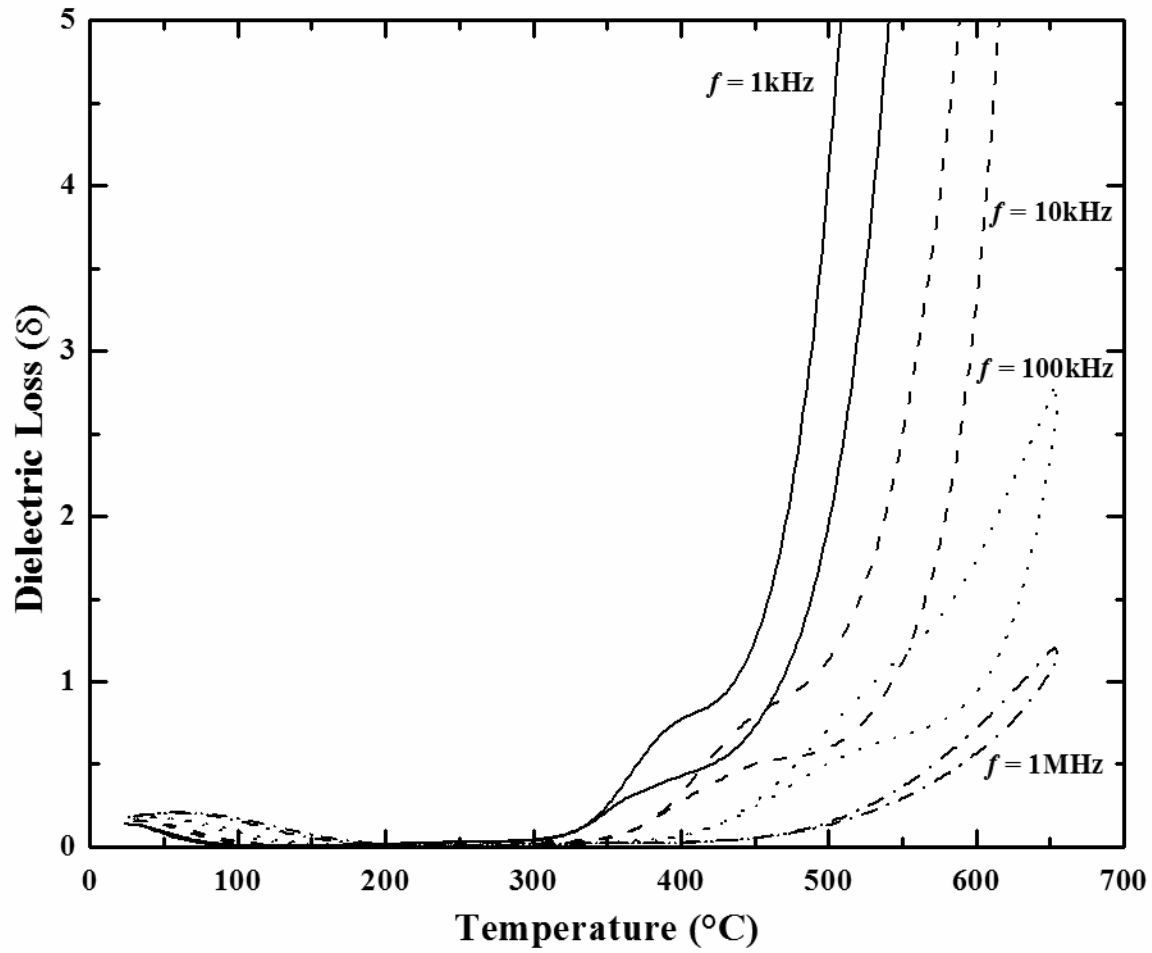

Figure 3.3: Dielectric loss tangent as a function of frequency and temperature for $(0.8)BaTiO_3$-$(0.2)Bi(Zn_{1/2}Ti_{1/2})O_3$.

These results were largely corroborated by a study that appeared during the course of this work [Huang 2008]. The solubility range was found to be somewhat more extensive (single-phase for BZT substitutions less than 34%), perhaps a function of higher calcination temperatures. That work confirmed the crystal structure of compositions between 5% BZT and the solubility limit was rhombohedral, and the dielectric response and relaxor characteristics were the same as reported here.

3.2.2 $(K_{1/2}Bi_{1/2})TiO_3$-$Bi(Zn_{1/2}Ti_{1/2})O_3$

Because the limited solubility of BZT in $BaTiO_3$ hampered the correlation of the Bi^{3+} displacements, substitution into $(K_{1/2}Bi_{1/2})TiO_3$ (KBT) was investigated to increase the Bi-occupancy. While the K^+ cation is approximately the same size of Ba^{2+} (1.64Å v. 1.61Å), KBT has an A-site that is already occupied by 50% Bi^{3+}. Even if KBT-BZT has a similarly limited solubility region, the A-site will still contain significant bismuth concentrations.

Tetragonal in structure with a T_C significantly higher than $BaTiO_3$ (270°C), KBT was first identified in the 1960s [Smolenskii 1961, Buhrer 1962]. First principles studies have shown that the Bi^{3+} cations in KBT do displace strongly, though their displacements are not correlated [Shuvaeva 2005]. The small tetragonal distortion (c/a = 1.024) in KBT is therefore B-site driven like $BaTiO_3$. Solid solutions of KBT with rhombohedral $(Na_{1/2}Bi_{1/2})TiO_3$ (NBT) have attracted considerable attention as a lead-free piezoelectric system, though their maximum piezoelectric response (d_{31} = 46.9 pC/N) is significantly lower than PZT-based systems [Sasaka 1999].

Compositions in the $(1-x)(K_{1/2}Bi_{1/2})TiO_3$-$(x)Bi(Zn_{1/2}Ti_{1/2})O_3$ solid solution were explored using calcination temperatures between 800°C and 1050°C. XRD patterns of these compositions are plotted in Figure 3.4. The x = 0.4 composition is clearly multi-phase, though traces of the main pyrochlore impurity peak at ~30° are visible starting with the x = 0.3 composition which is considered the solubility limit. Peak broadening in the x = 0.1 composition is consistent with a small tetragonal distortion in the structure,

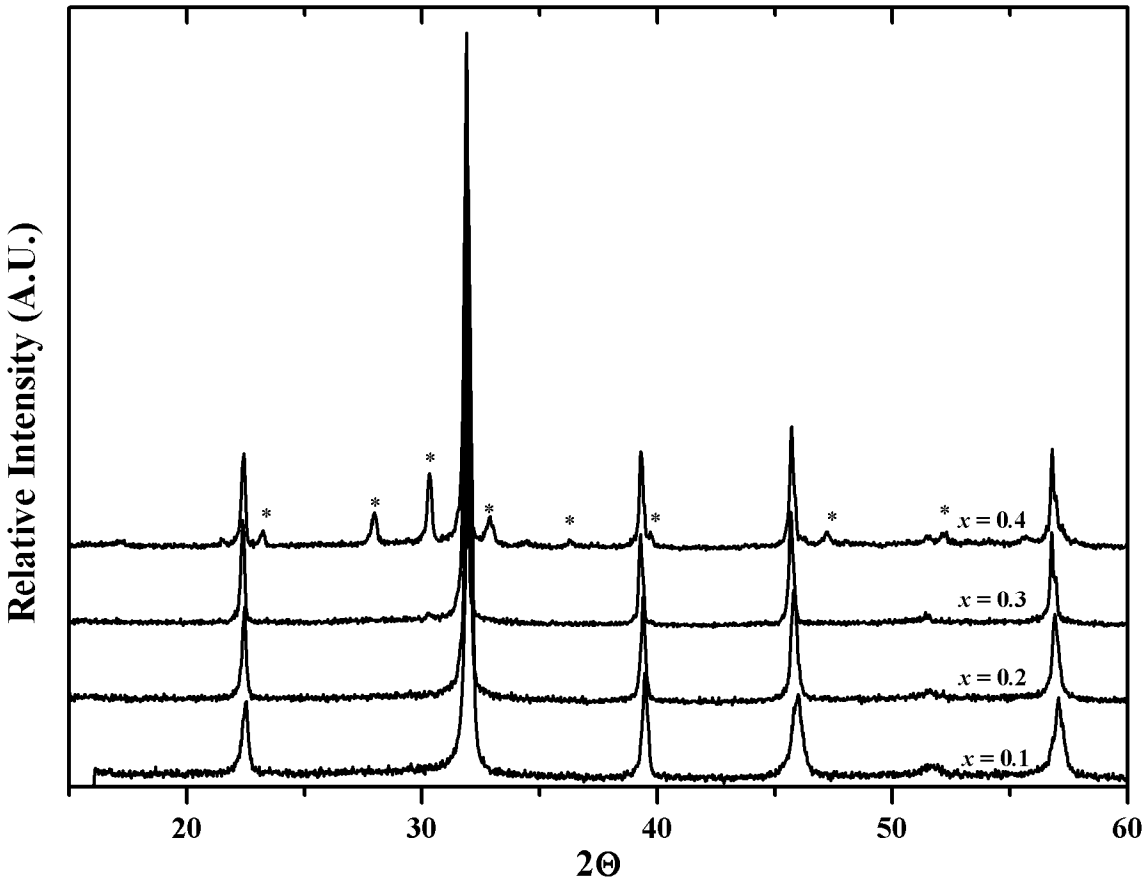

Figure 3.4: XRD patterns of compositions in the $(1\text{-}x)(K_{1/2}Bi_{1/2})TiO_3 - (x)Bi(Zn_{1/2}Ti_{1/2})O_3$ solid solution. Starred peaks in the x = 0.4 composition indicate impurities.

however higher-level substitutions show no such broadening. The broadening was quantified by comparing the width of the (200) peak located at approximately 46° in the single phase compositions. The width of this peak in the x = 0.1 sample is significantly larger than the x = 0.2 and 0.3 compositions (0.507° v. 0.292° and 0.226°, respectively). The substitution of BZT slightly increases the volume of the unit cell, consistent with the larger size of the B-site cations in BZT.

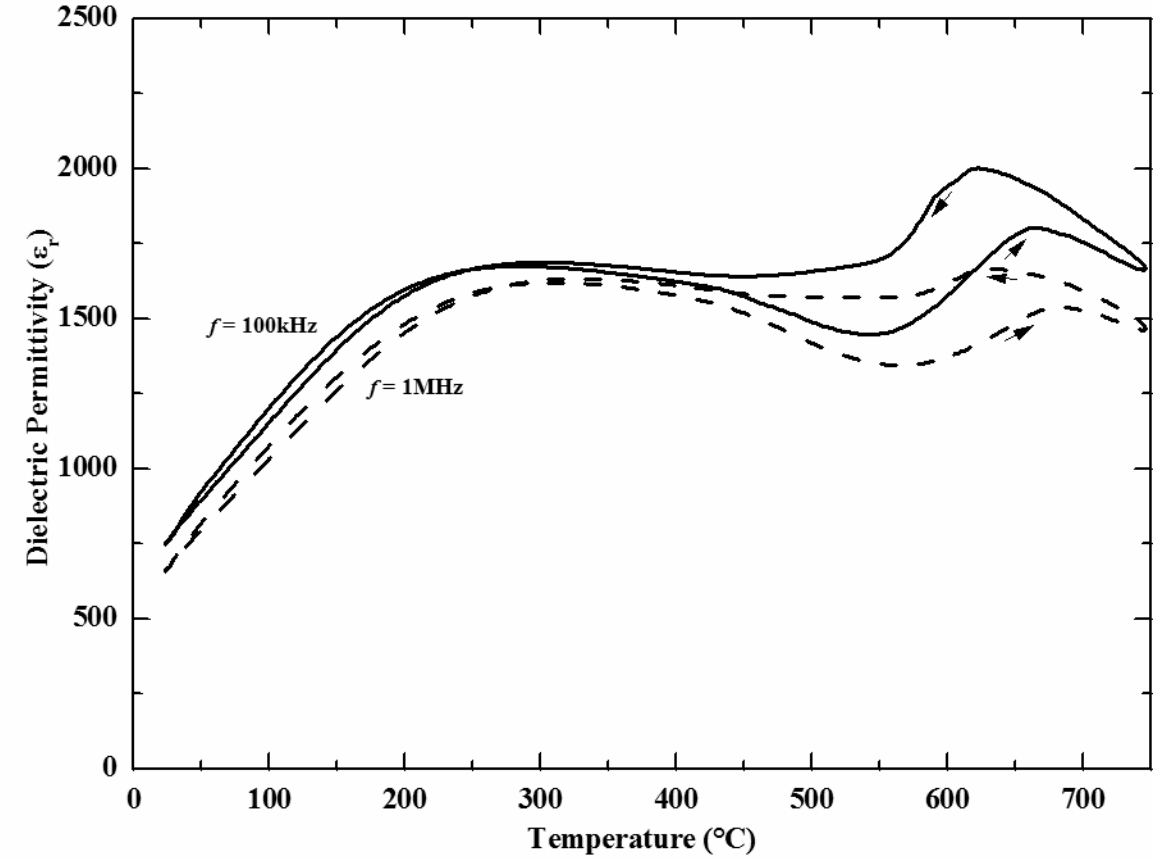

Figure 3.5: Dielectric response as a function of temperature for the $(0.7)(K_{1/2}Bi_{1/2})TiO_3 - (0.3)Bi(Zn_{1/2}Ti_{1/2})O_3$ composition. Arrows indicate the direction of thermal ramp.

The dielectric response of single-phase KBT-BZT compositions (x = 0.1 – 0.3) was investigated as a function of temperature. Figure 3.5 shows the data collected for the x = 0.3 composition and is representative of the series. Consistent with the previously discussed $BaTiO_3$-BZT system, the substitution of BZT induces relaxor behavior, as indicated by the broad frequency-dependent peak in the 200-300°C range.

While the KBT-BZT system shows no evidence for any increase in tetragonality it is interesting to note the system shows evidence for a second higher temperature dielectric transition close to 650°C. The observed hysteresis is also consistent with a

ferroelectric transition. This dielectric feature will be discussed further in chapter 4. Although these solid solutions contain more than 50% Bi on the A-site, any long-range correlations to produce enhanced tetragonality are apparently suppressed by the large K^+ cations.

3.2.3 $(Na_{1/2}Bi_{1/2})TiO_3$-$Bi(Zn_{1/2}Ti_{1/2})O_3$

Because $BaTiO_3$ and KBT were able to suppress the correlation of Bi^{3+} displacements in their solid solutions with BZT, substitutions into $(Na_{1/2}Bi_{1/2})TiO_3$ (NBT), where the Na^+ cations are significantly smaller (1.39Å v. 1.64Å), were explored.

NBT was first reported by Smolenskii and Buhrer and received little attention until recently [Smolenskii 1961, Buhrer 1962]. At room temperature, the stable structure is a rhombohedral perovskite (*R3c* crystal structure); with increasing temperature the structure transitions to a tetragonal phase (*P4bm*, dissimilar to $PbTiO_3$ and $BaTiO_3$) before a transformation to the prototypical cubic structure [Jones 2002].The rhombohedral structure is ferroelectric and NBT has a high Curie temperature (325°C) for a lead-free perovskite.

Samples in the $(1-x)(Na_{1/2}Bi_{1/2})TiO_3$-$(x)Bi(Zn_{1/2}Ti_{1/2})O_3$ solid solution were synthesized between 800°C and 1050°C and the XRD patterns are shown in Figure 3.6. The solubility of BZT into NBT was found to be even more limited than KBT with a single phase perovskite only extending to between $x = 0.1$ and 0.2. The structure remains rhombohedral throughout the solubility range as evidenced by the peak broadening in the

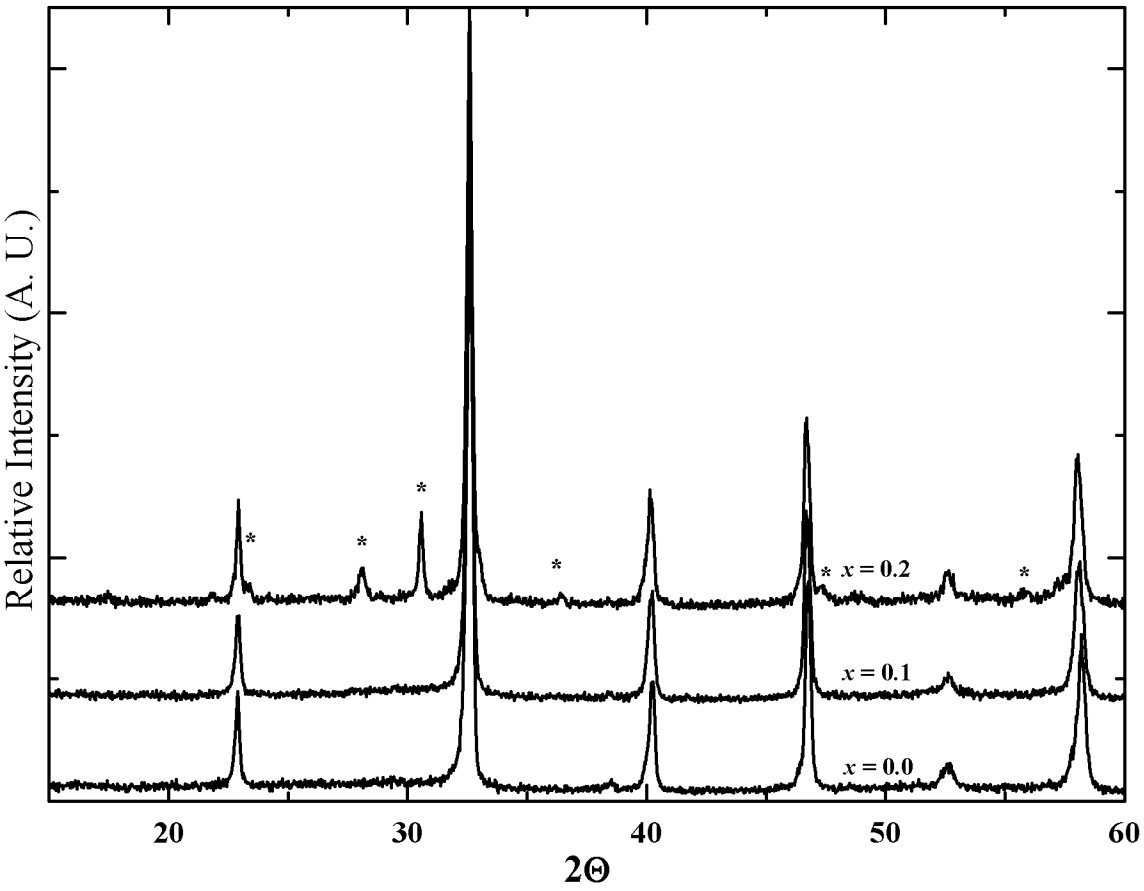

Figure 3.6: XRD patterns of compositions in the (1-*x*)($Na_{1/2}Bi_{1/2}$)TiO_3 – (*x*)Bi($Zn_{1/2}Ti_{1/2}$)O_3 solid solution. Starred peaks in the x = 0.2 composition indicate impurities.

(111) family of peaks, the result of unresolved splitting from the rhombohedral distortion.

As in $BaTiO_3$ and KBT, the limited solubility of BZT into NBT prevents investigation of how the structure would respond to higher levels of BZT. In all these solid solutions, high fractions of Bi^{3+} (and Ti^{4+}) cations stabilize a $Bi_2Ti_2O_7$ pyrochlore or other related phases.

3.2.4 $(Na_{1/2}K_{1/2})NbO_3$-$Bi(Zn_{1/2}Ti_{1/2})O_3$

While there are a variety of secondary phases that compete with perovskite in Bi-containing compositions, $Bi_2M_2O_7$ pyrochlores, in particular where M includes Ti^{4+}, is the most prevalent observed in the systems investigated in this work. The stability of this phase can be reduced by avoiding compositions with 4+ cations. Because Nb^{5+} is the most ferroelectrically active 5+ cation and can be paired with the K^+ and Na^+ to form a stable perovskite, we attempted to substitute BZT into $(Na,K)NbO_3$ ferroelectric end-members.

$(Na_xK_{1-x})NbO_3$ forms a complete range of solid solutions. $KNbO_3$ and $NaNbO_3$ were first reported in 1949, and after preliminary studies of the solid solution in 1954, a detailed phase diagram including the tilt systems was reported in 1976 [Matthias 1949, Shirane 1954, Ahtee 1976]. While the room temperature structure is nominally orthorhombic across the entire solid solution, the structure undergoes transitions between different tilt systems at different points within the solution.

Despite the existence of octahedral tilting, the solution remains ferroelectric across most of the compositional range with Curie temperatures remaining at or above 400°C. Compositions near (within 10%) the $NaNbO_3$ end member are antiferroelectric.

While $KNbO_3$ ceramics exhibit a weak bulk piezoelectric response, $(Na_{1/2}K_{1/2})NbO_3$ (NKN), which lies near the transition between the $KNbO_3$-type "simple" orthorhombic structure and a tilted orthorhombic structure has been reported to exhibit much better piezoelectric performance (d_{33} = 160 pC/N) [Jaeger 1962]. Densification

issues have limited the commercial applicability of NKN as advanced sintering techniques such as hot pressing or spark plasma sintering are necessary to achieve high density [Li 2006].

Concurrent with the work in this thesis, the substitution of $BiScO_3$ into NKN was investigated [Zuo 2007, Sun 2009]. The resultant ceramics could be sintered at temperatures (up to 1150°C) low enough to avoid melting and the piezoelectric performance was enhanced to >200 pC/N at the MPB composition. The goal of our study was to stabilize a high *c/a* tetragonal structure of NKN at room temperature through the substitution of BZT.

Compositions in the $(1-x)(Na_{1/2}K_{1/2})NbO_3$-$(x)Bi(Zn_{1/2}Ti_{1/2})O_3$ solid solution were synthesized using solid-state precursors using calcination temperatures between 800°C and 1100°C. The XRD patterns are shown in Figure 3.7. The solubility limit for BZT into NKN was found to be between $x = 0.3$ and 0.4. The crystal structure for all investigated compositions is cubic, though peak broadening in the $x = 0.1$ composition suggests unresolved peak splitting consistent with a rhombohedral or orthorhombic structure. During our work this behavior was confirmed by another study [Sutapun 2009]. In that work it was found that the structure transitions from the orthorhombic structure of NKN to rhombohedral and then cubic within the first 3% of BZT substitution. $Bi_2Ti_2O_7$ was the first reported impurity phase at $x = 0.25$ compared to a combination of $Bi_2Ti_2O_7$ and other phases at $x = 0.4$ here.

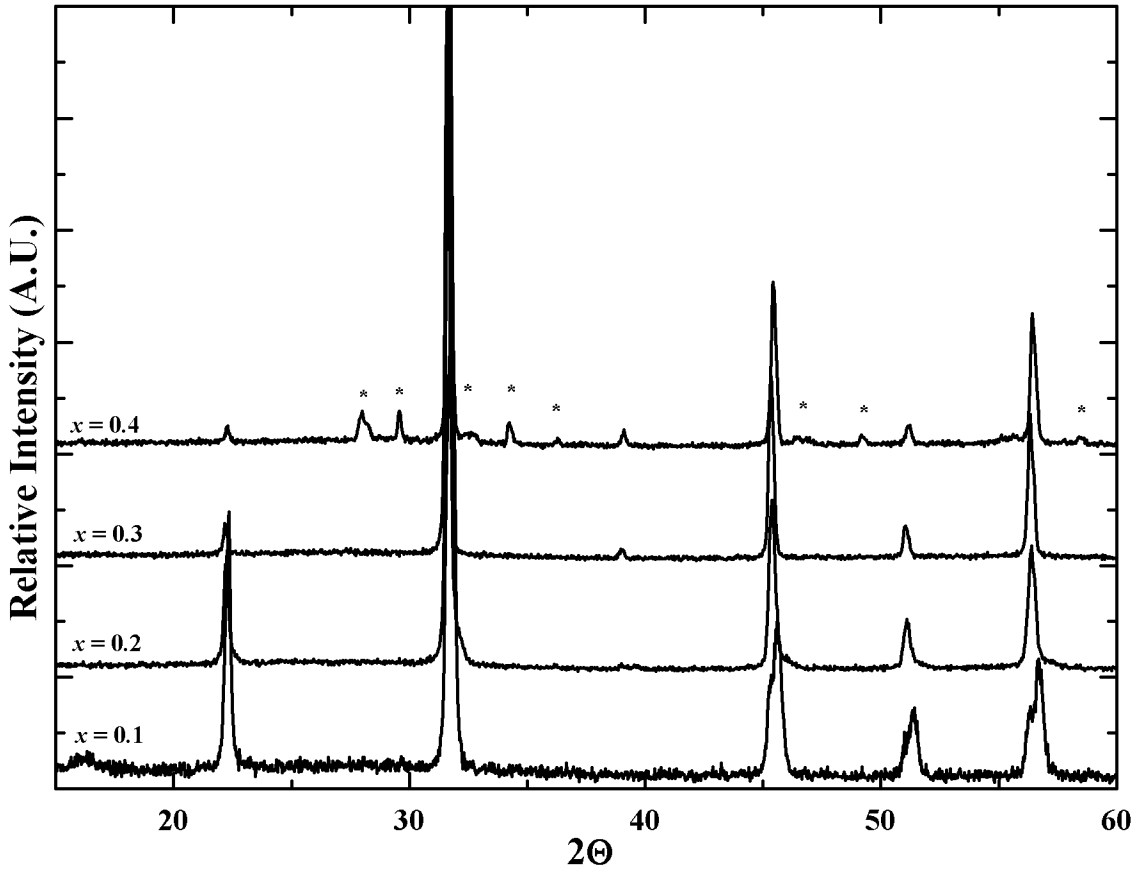

Figure 3.7: XRD patterns of compositions in the (1-*x*)($Na_{1/2}K_{1/2}$)NbO_3 – (*x*)Bi($Zn_{1/2}Ti_{1/2}$)O_3 solid solution. Starred peaks in the x = 0.4 composition indicate impurities.

Measurements of the dielectric response of the compositions investigated here were consistent with the observed cubic structure and revealed no dielectric maximum or any evidence for a ferroelectric transition above room temperature.

3.3 Conclusions

The research presented in this chapter attempted to stabilize tetragonally distorted ferroelectric lead-free perovskite systems through the substitution of $Bi(Zn_{1/2}Ti_{1/2})O_3$. The ranges of solubility in all systems investigated were limited to less than 40% substitution and no evidence was found for any enhanced tetragonality.

Apparently the co-occupancy of the A-site by ferroelectrically inactive cations (e.g. K, Ba, Na) is sufficient to suppress any correlated displacements of Bi^{3+} through cation-cation repulsive forces.

These systems are also complicated by the formation of secondary Bi-containing titanate pyrochlores which severely limit the range of perovskite stability. The impurity formation is suppressed to larger substitutions of BZT in the niobate based NKN system, however the resultant perovskites had cubic symmetry.

Although the KBT-BZT system did not show enhanced tetragonality and correspondingly only showed a weak relaxor-type transition in the permittivity at temperatures similar to the T_C of pure KBT, evidence for a second dielectric maximum of ~650°C was found for a sample containing 30% BZT. This is discussed further in chapter 4.

The next chapter returns to mixed Pb/Bi A-site perovskites to attempt to capture the large correlated Bi^{3+} displacements at an MPB to enhance piezoelectric response.

Chapter 4:

Enhanced Tetragonality in Ternary Systems

4.1 Introduction & Motivation

Bismuth has been intensely investigated as a replacement for lead in piezoelectric perovskite systems. The Bi^{3+} cation possesses the 6*s* electron pair responsible for the large displacements of Pb^{2+} in piezoelectric systems such as $Pb(Zr,Ti)O_3$ and lacks the environmental and health concerns of lead [Cohen 1992]. Furthermore, theoretical and experimental work has shown that A-site displacements and polarization magnitudes can be significantly larger in Bi-based perovskite systems than in their Pb-based counterparts [Baettig 2005, Belik 2006 A, Belik 2006 B, Grinberg 2007]. Despite this, most Bi-based additives to $PbTiO_3$ (PT) behave similarly to $PbZrO_3$: with increasing substitution, the tetragonality of the structure decreases until a morphotropic phase boundary (MPB) is formed. MPBs are crucial for piezoelectric applications, as the energy necessary to reorient the macroscopic polarization is drastically reduced relative to nearby compositions in a solid solution.

Compared to their Pb-based counterparts, Bi-based substitutions in PT can induce higher transition temperatures at the MPB (e.g. T_C = 425°C for (0.37)PT-(0.63)$Bi(Mg_{1/2}Ti_{1/2})O_3$ (BMT), 450°C for (0.64)PT – (0.36)$BiScO_3$). However, the larger displacements of Bi^{3+} do not enhance the macroscopic polarizations of PT [Randall 2004, Eitel 2001]. Correlated displacements are possible when the B-site contains a high

fraction of ferroelectrically-active cations capable of cooperatively displacing to minimize repulsive forces between the A- and B-sub-lattice [Grinberg 2005, Grinberg 2007]. Consequently additives such as $Bi(Zn_{1/2}Ti_{1/2})O_3$ (BZT) and the newly discovered additive discussed in chapter 2, $Bi(Zn_{3/4}W_{1/4})O_3$, allow for the correlation of individual cation displacements when added to PT by combining Bi^{3+} with known ferroelectrically-active (FE-active) B-site cations [Suchomel 2005, Stein 2006, Fedulov 1964, Nomura 1982]. The (1-*x*)PT - (*x*)BZT solid solution has solubility up to $x = 0.4$ with a *c/a* ratio of 1.11 and a T_C that exceeds 700°C at that composition. In contrast to almost all other additives, these substituents induce a sustained increase in the tetragonality of the structure until the solubility limit is reached. The increased *c/a* ratio is accompanied by significant increases in the Curie temperature (T_C). The next step toward using these tetragonality enhancing additives for piezoelectric applications is to capture the enhanced polarization at an MPB to improve the piezoelectric response and to raise the ferroelectric to paraelectric transition temperature.

To date, this potential has not been realized in known Bi-containing MPB-forming systems. The piezoelectric responses reported in PT-$BiScO_3$ (≈450 pC/N) and the PT-BMT (≈225 pC/N) systems do not exceed those observed in PZT compositions [Eitel 2002, Randall 2004]. Both systems, however, do exhibit high T_Cs at the MPB. The enhanced tetragonality PT-BZT system was found to have Bi^{3+} displacements significantly larger than Pb^{2+} cations (0.82-0.90Å v. 0.44-0.56Å respectively) [Grinberg 2007]. Furthermore, displacement of the Zn^{2+} cations is even larger than Ti^{4+}. Capturing these displacements at an MPB could result in improved piezoelectric performance.

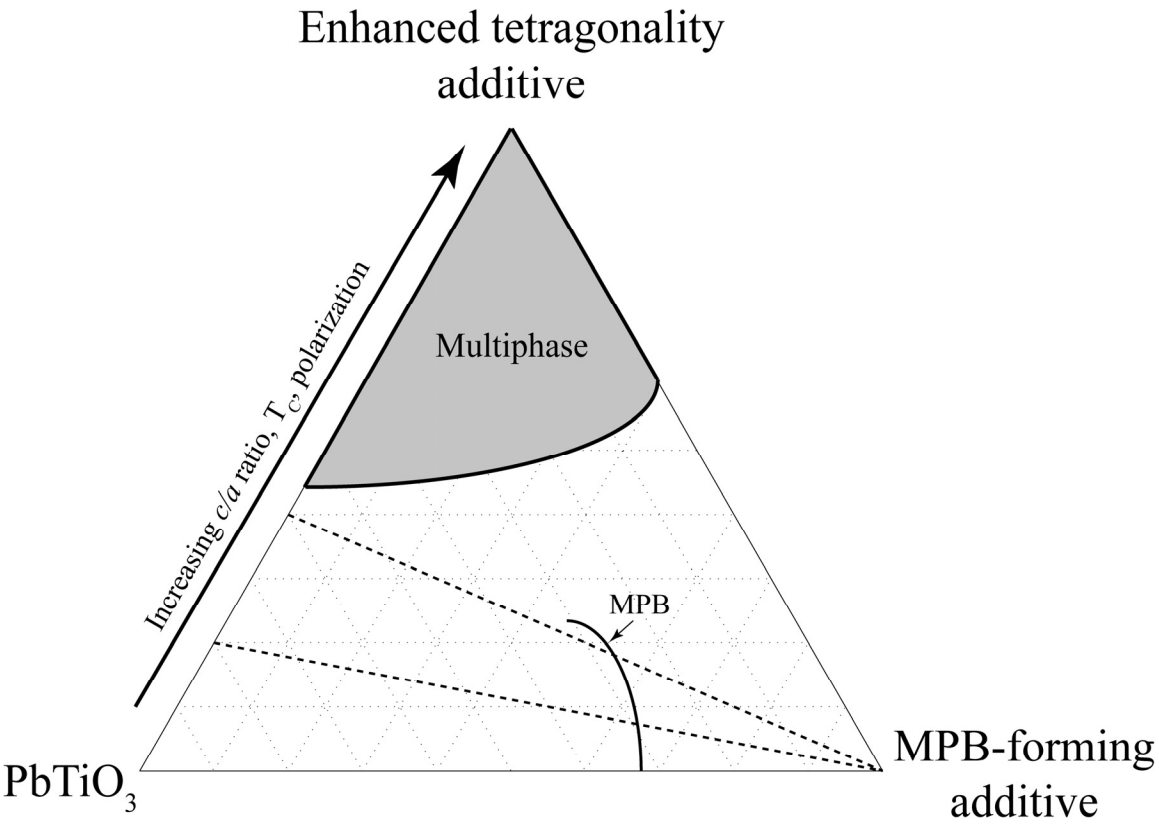

Figure 4.1: Abstract schematic of ternary systems between $PbTiO_3$, enhanced tetragonality additives and MPB-forming additives. Dotted lines represent binary solid solutions between enhanced tetragonality pseudo-end-members and the MPB-forming additive.

This chapter will present work that attempts to capture these larger displacements by investigating ternary systems. The generalized approach is illustrated in Figure 4.1. An enhanced tetragonality pseudo-binary end-member is formed between PT and a Bi-based *c/a* enhancing additive such as BZT. This pseudo-end-member can be tailored for specific *c/a* ratios, bismuth content, or other relevant properties. Solid solutions between this end-member and an MPB-forming additive are then investigated with a view towards stabilizing an MPB with a higher *c/a* ratio than reported in pure PT-based systems.

Capturing these displacements at an MPB will ideally manifest as both increased Curie temperatures and improved piezoelectric response. The next two sections of this chapter examines BZT-based ternaries with a variety of MPB-forming additives. The fourth explores ternaries where $BiFeO_3$ is utilized instead of BZT to enhance *c/a*. The data from both sections are discussed in the last section.

4.2 $PbTiO_3 - Bi(Zn_{1/2}Ti_{1/2})O_3 - Bi(Mg_{1/2}Ti_{1/2})O_3$

4.2.1 Synthesis details

Compositions in the $(1-x)[(1-y)PbTiO_3 - (y)Bi(Zn_{1/2}Ti_{1/2})O_3] - (x)Bi(Mg_{1/2}Ti_{1/2})O_3$ ternary system were synthesized at temperatures between 800°C and 1100°C. The locations of the compositions investigated within the ternary system are shown in Figure 4.2. Most compositions fall along one of two pseudo-binary solid-solution lines: $(1-x)[(0.9)PbTiO_3 - (0.1)Bi(Zn_{1/2}Ti_{1/2})O_3] - (x)Bi(Mg_{1/2}Ti_{1/2})O_3$ [90/10] and $(1-x)[(0.75)PbTiO_3 - (0.25)Bi(Zn_{1/2}Ti_{1/2})O_3] - (x)Bi(Mg_{1/2}Ti_{1/2})O_3$ [75/25]. These lines are differentiated by the concentration of BZT the binary end-member (0.1 and 0.25). These end-members have *c/a* ratios of 1.073 and 1.087, respectively, compared to 1.065 of $PbTiO_3$ and T_C's of 535°C and 590°C compared to 490°C for $PbTiO_3$.

Neither of the Bi-based end-members are stable single-phase perovskites at ambient pressure; consequently a large region of the ternary diagram near those end-members is multiphase. Single-phased compositions surrounding the PT end-member are tetragonal at room temperature. The *c/a* ratio of this structure increases with BZT substitution and decreases with BMT substitution. A morphotropic phase boundary between the tetragonal phase and a rhombohedral phase exists in the single-phase region in the PT- and BMT-rich part of the diagram.

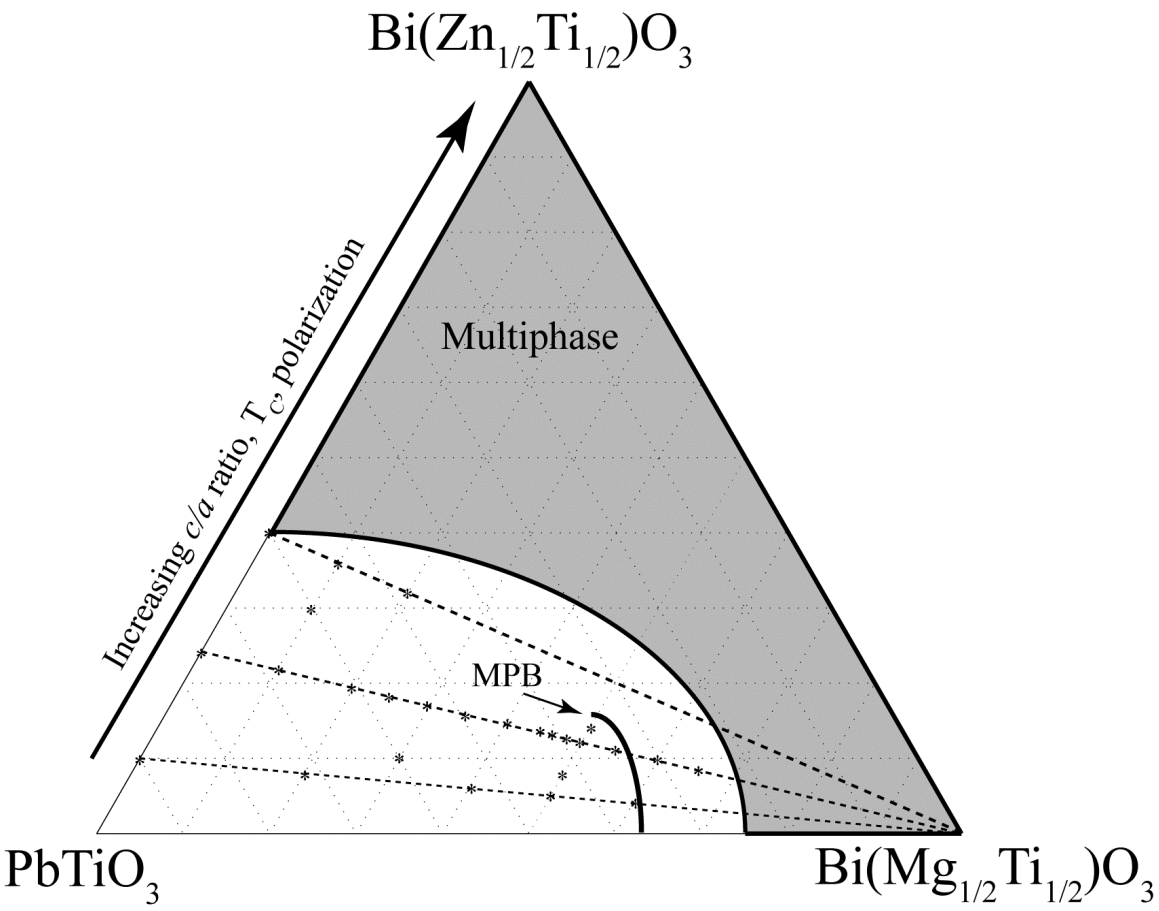

Figure 4.2: Ternary phase diagram for the PT-BZT-BMT system. Dotted lines represent enhanced tetragonality binary solid-solutions. Compositions investigated are denoted by a '*'. The heavy dark line represents the approximate position of the morphotropic phase boundary.

4.2.2 Room temperature structural properties

Solid solutions of the [75/25] end-member could be formed up to ~60% substitution of BMT. XRD patterns of these compositions are shown in Figure 4.3. The structure of the solid solution behaves as expected: from a starting c/a ratio of 1.087 at the [75/25] end-member the tetragonal distortion decreases with increasing BMT content until an MPB is reached at x = 0.55. Typical of Bi-containing compositions, small

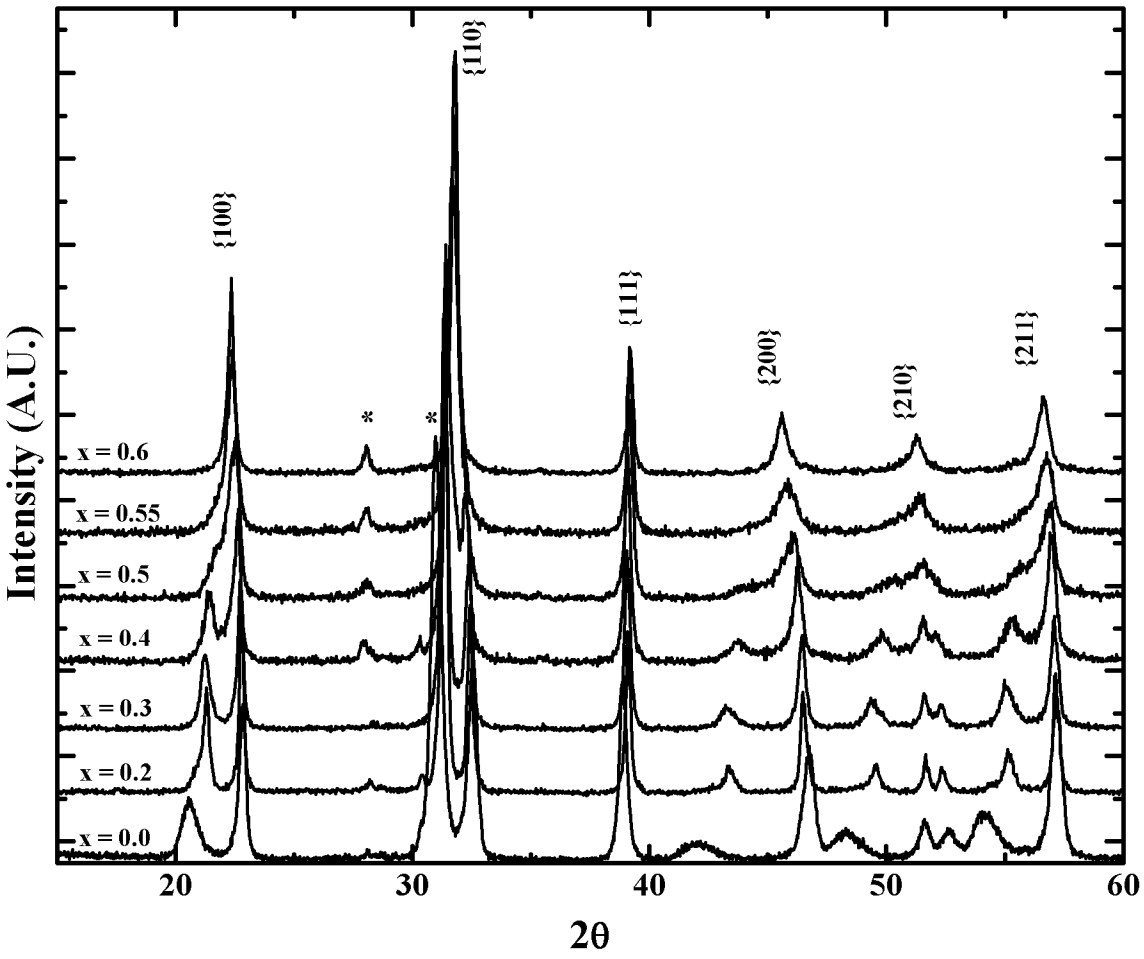

Figure 4.3: XRD patterns of compositions in the (1-*x*)[(0.75)$PbTiO_3$ – (0.25)$Bi(Zn_{1/2}Ti_{1/2})O_3$] – (*x*)$Bi(Mg_{1/2}Ti_{1/2})O_3$ solid solution. Families of perovskite peaks are labeled. Peaks denoted with a '*' represent impurity phases.

amounts of impurities are observed in the XRD patterns. The solid-solution with the [90/10] end-member reveals similar behavior (Figure 4.4). Unlike the [75/25] solid-solution, patterns in the [90/10] solution are free of peaks from impurity phases. Again the *c/a* of the PT-BZT end-member is reduced with increasing levels of BMT and an MPB is formed near a substitution of 60%. The amount of BMT required form an MPB for the [90/10] line is less than that reported for the binary PT-BMT system (63% BMT)

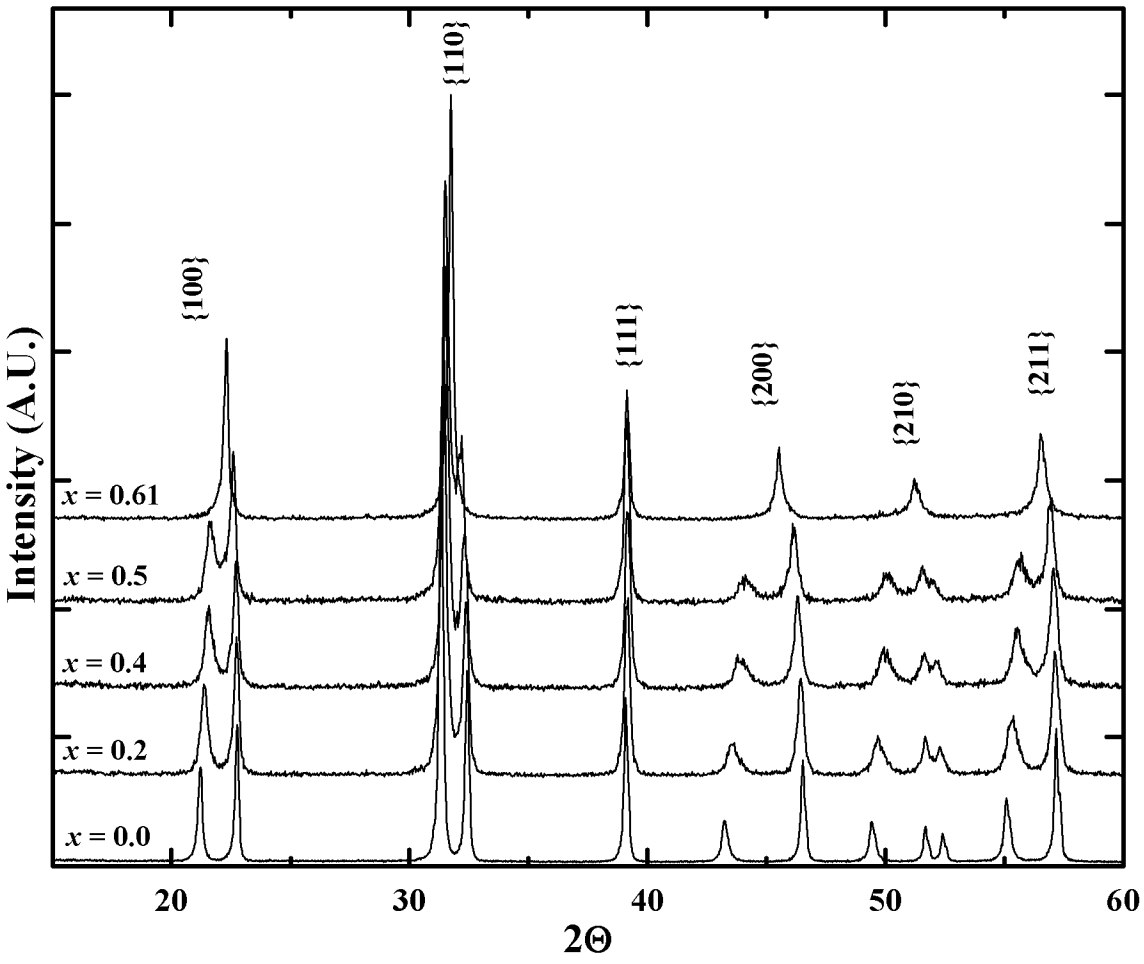

Figure 4.4: XRD patterns of compositions in the (1-*x*)[(0.9)$PbTiO_3$ – (0.1)$Bi(Zn_{1/2}Ti_{1/2})O_3$] – (*x*)$Bi(Mg_{1/2}Ti_{1/2})O_3$ solid solution. Families of perovskite peaks are labeled.

and more than in the [75/25] solid solution (55%). The lattice parameters for these two pseudo-binary solid solutions are shown in Figure 4.5, which also includes data from the PT-BMT binary system [Randall 2004, Suchomel 2004].

Figure 4.5 reveals that as the tetragonality of the PT-BZT end-member increases the concentration of the BMT additive required to induce the formation of an MPB is reduced. A similar observation was reported in the studies of the PT-BZT-$BiScO_3$ system

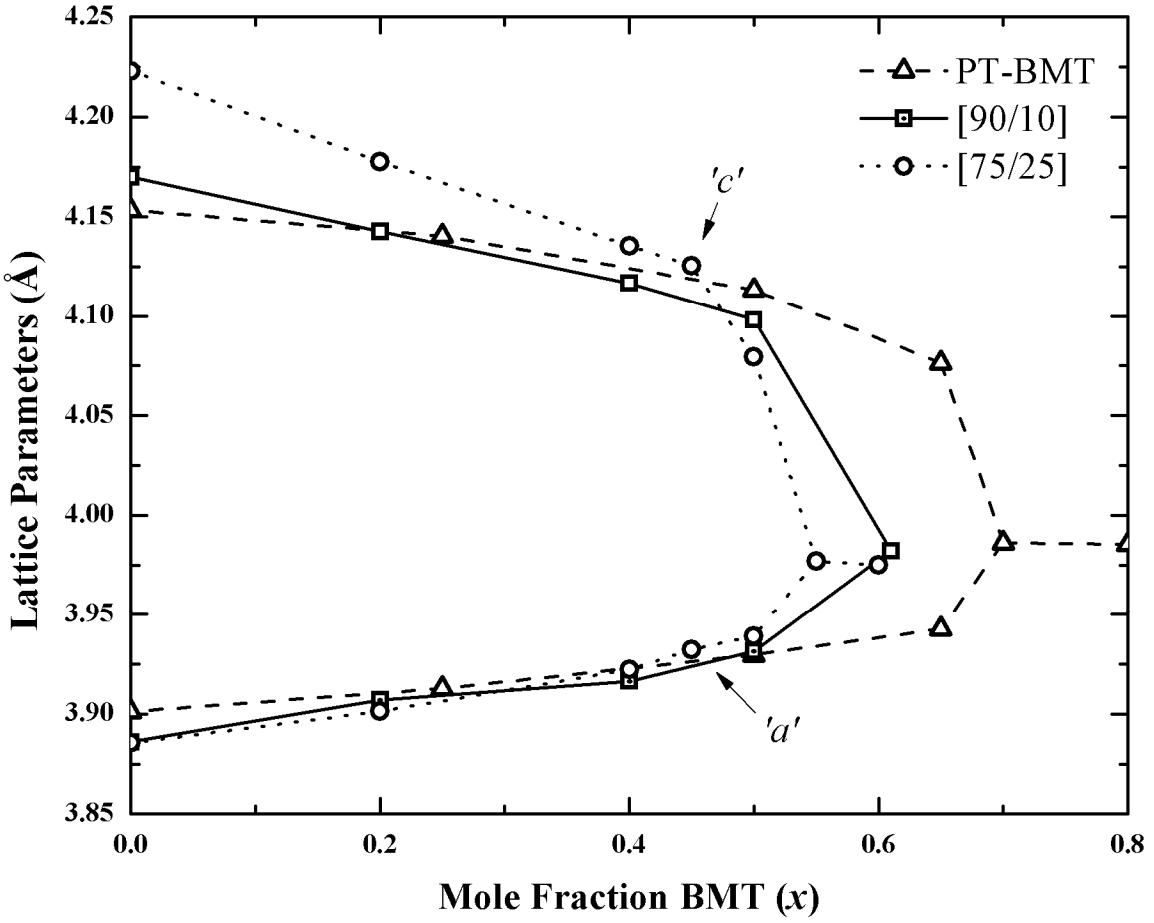

Figure 4.5: Lattice parameters as a function of BMT substitution for the (1-*x*)[90/10]-(*x*)BMT and (1-*x*)[75/25]-(*x*)BMT solid solutions. Data from PT-BMT is also included [Suchomel 2004]. Convergence of the lattice parameters indicates the approximate MPB position.

[Suchomel 2005]. This result is somewhat surprising as it might be expected that end-members with a higher *c/a* would require increasing concentrations of the MPB-forming additive (BMT) to reduce the tetragonality and form an MPB. These results, coupled with those reported by Suchomel, clearly demonstrate the opposite is true in these systems. This trend might also imply that if the *c/a* of the tetragonal end-member is reduced to a

value below that of PT the substitution of BMT would stabilize an MPB closer to that end-member. This effect will be discussed further in a subsequent section.

4.2.3 Dielectric properties

In all known MPB-forming systems the T_C at the MPB is lower than the Curie temperatures of the tetragonal end-member, we would expect to observe the same in PT-BZT-BMT. However, as shown in Figure 4.6 and 4.7 for the [90/10]-BMT and [75/25]-BMT solid-solutions, respectively, we did not observe any significant reduction in T_C over the range of the investigated compositions. Remarkably, the T_C at the MPB composition (x = 0.55) for the [75/25]-BMT system is 585ºC, similar to the enhanced tetragonality end-member (590ºC). More strikingly, T_Cs in the [90/10]-BMT system actually increase over the range of substitution. These transition temperatures are significantly higher than the MPB compositions in the PT-$BiScO_3$ (450ºC) and PT-BMT (425ºC) systems [Suchomel 2005, Eitel 2001, Randall 2004]. The high T_C values in this ternary system suggest the presence of large, stable cation displacements, and possibly enhanced piezoelectric properties.

However, the permittivities of ternary PT-BZT-BMT ceramics exhibit some unusual features. Usually, tetragonal PT-based perovskite solid solutions show a single dielectric maximum at the Curie temperature associated with the transition to a cubic paraelectric phase. This is not the case for many compositions in both the [90/10]-BMT and [75/25]-BMT solid solutions. Compositions with $x \geq 0.4$ in the (1-x)[90/10]– (x)BMT solid solution and $0.2 \geq x \geq 0.35$ in the (1-x)[75/25]– (x)BMT solid solution exhibit

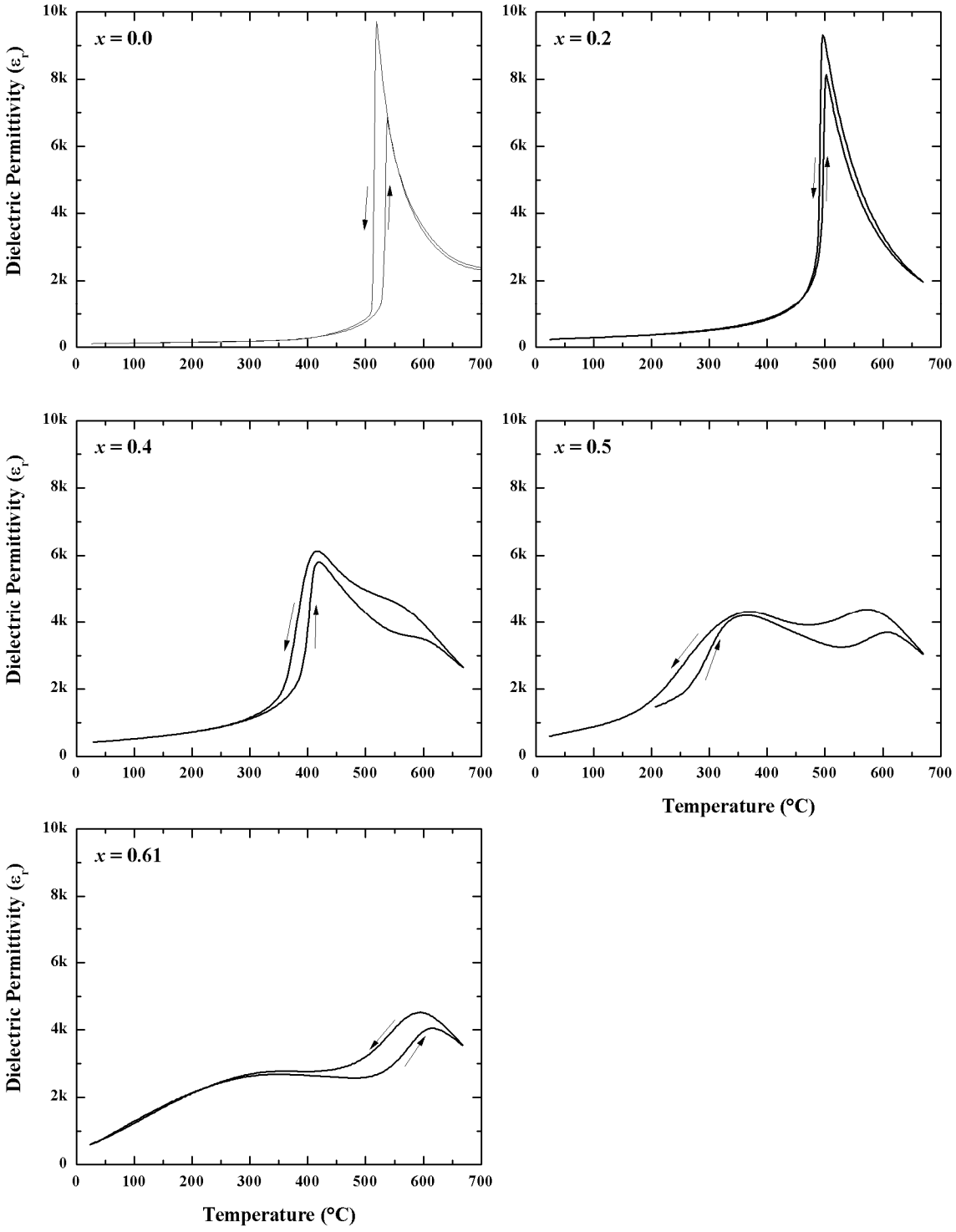

Figure 4.6: Dielectric response (f = 100kHz) for compositions in the (1-*x*)[90/10]–(*x*)BMT solid solution. Arrows indicate the direction of thermal ramp.

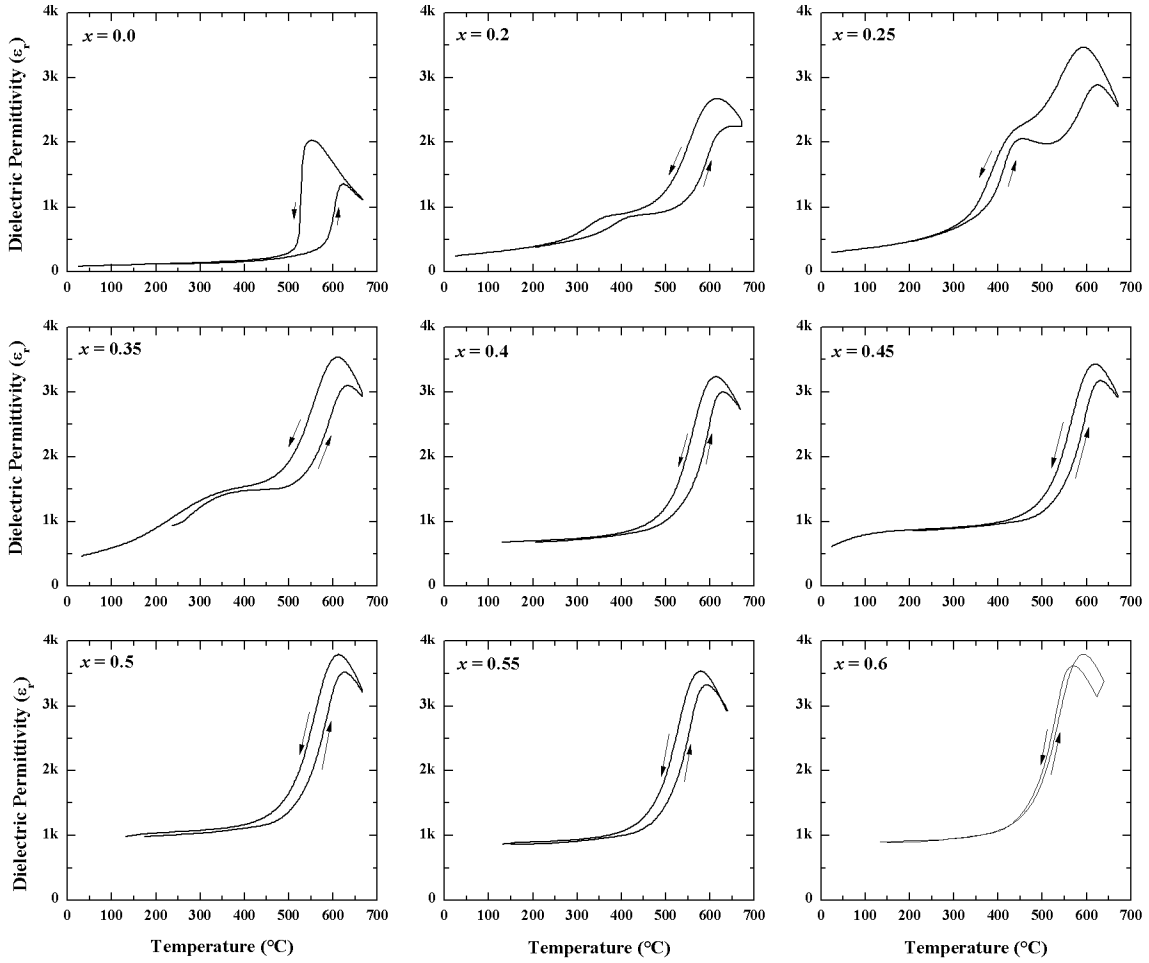

Figure 4.7: Dielectric response (f = 100kHz) for compositions in the (1-x)[75/25] – (x)BMT solid solution. Arrows indicate the direction of thermal ramp.

multiple dielectric transitions. In these compositions, one high-temperature transition is observed near 600°C while the other decreases in temperature as BMT levels increase. Thermal hysteresis is observed in both sets of dielectric transitions, suggesting a structural origin necessitating a nucleation process. In the [75/25]-BMT line the permittivity in the near room-temperature region increases by almost an order of magnitude as BMT levels increase, suggesting that some dielectric transition has shifted

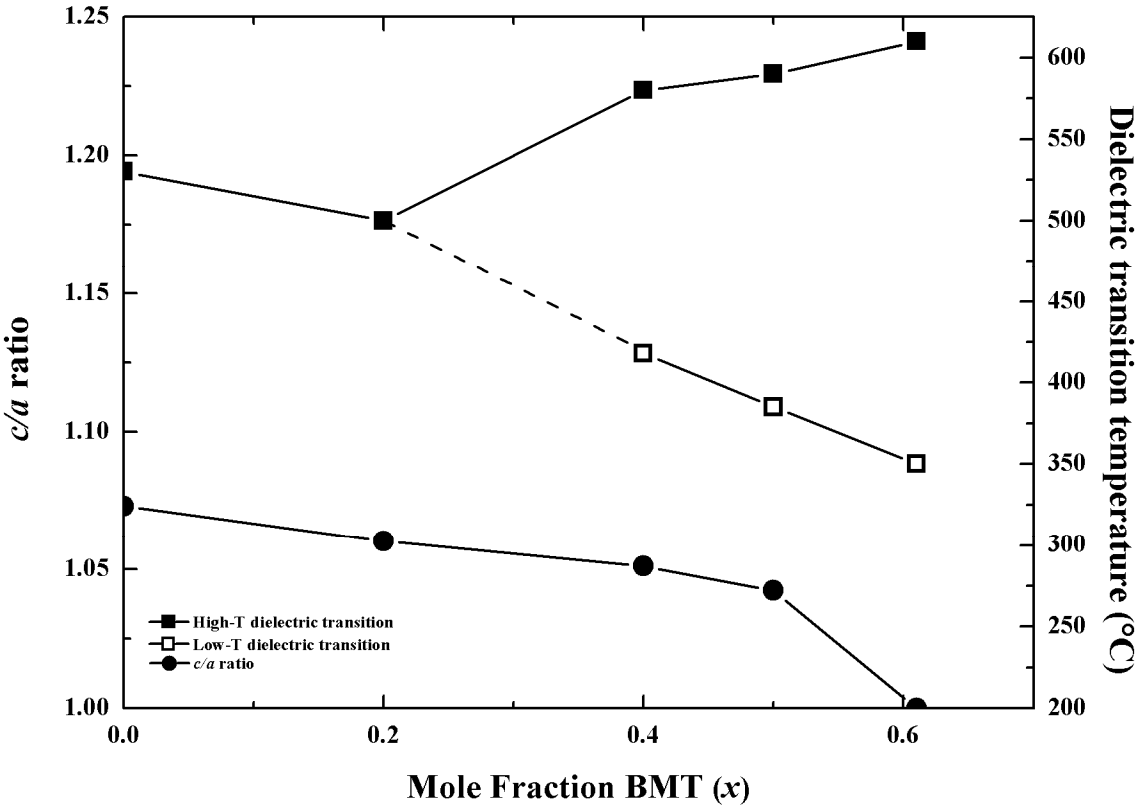

Figure 4.8: *c/a* ratio and dielectric transition temperatures as a function of composition in the (1-*x*)[90/10] – (*x*)BMT solid solution.

to below room temperature. The systematic variance of these dielectric transitions with BMT substitution is shown for the [90/10]-BMT and [75/25]-BMT solid solutions in Figures 4.8 and 4.9, respectively.

In the [90/10]-BMT solid solution, the T_C decreases consistent with *c/a* ratio as BMT concentration is increased to 20%. However, at greater BMT substitutions the single dielectric transition seemingly splits into two, with the lower temperature transition continuing to decrease with *c/a* ratio while the higher temperature transition increases to temperatures higher than the [90/10] end-member.

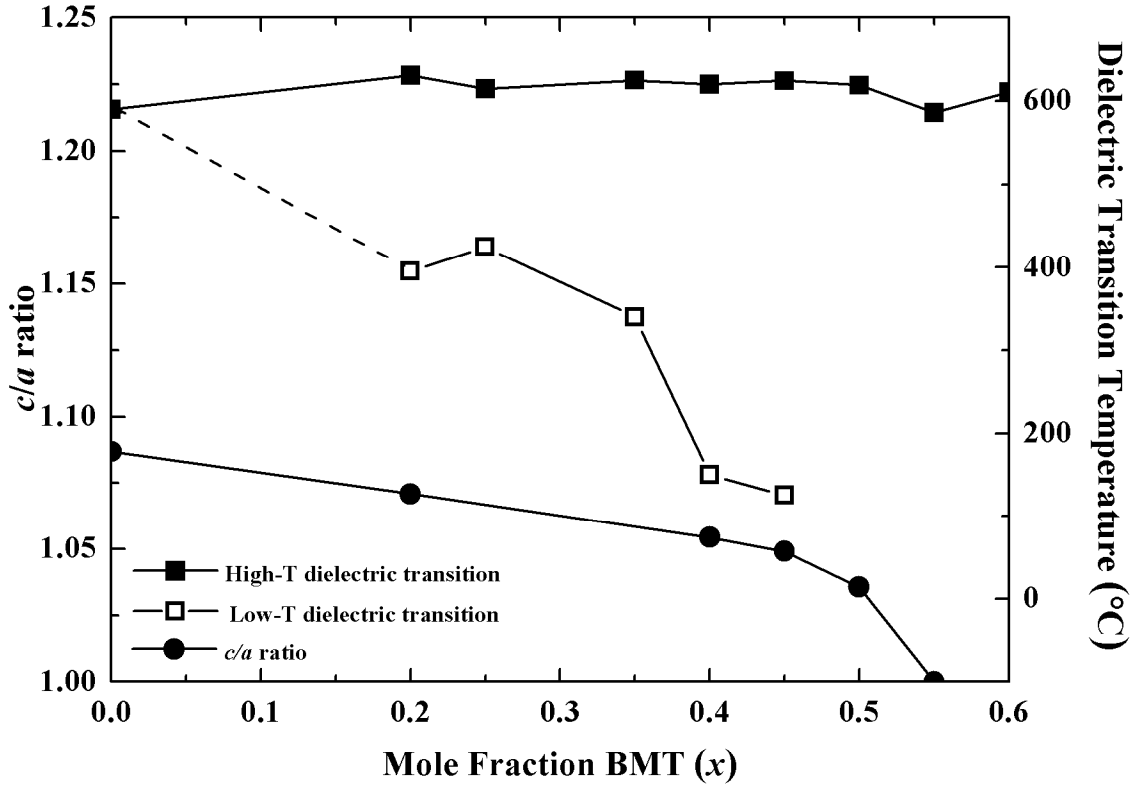

Figure 4.9: *c/a* ratio and dielectric transition temperatures as a function of composition in the (1-*x*)[75/25] – (*x*)BMT solid solution.

In the [75/25]-BMT line, the single transition of the tetragonal end-member splits into two transitions at a lower substitution than observed in the [90/10]-BMT solution (*x* = 0.2). The higher temperature transition stays nearly constant (~600°C) while the lower temperature decreases with increasing BMT levels. Beyond *x* = 0.45, only the higher temperature maximum is observed.

The multiple dielectric transitions in the PT-BZT-BMT system are observed in a region characterized by a large occupancy of Bi cations on the A-site as well as a majority of FE-active B-site cations (Ti^{4+} + Zn^{2+}), shown in Figure 4.10. Consistent with

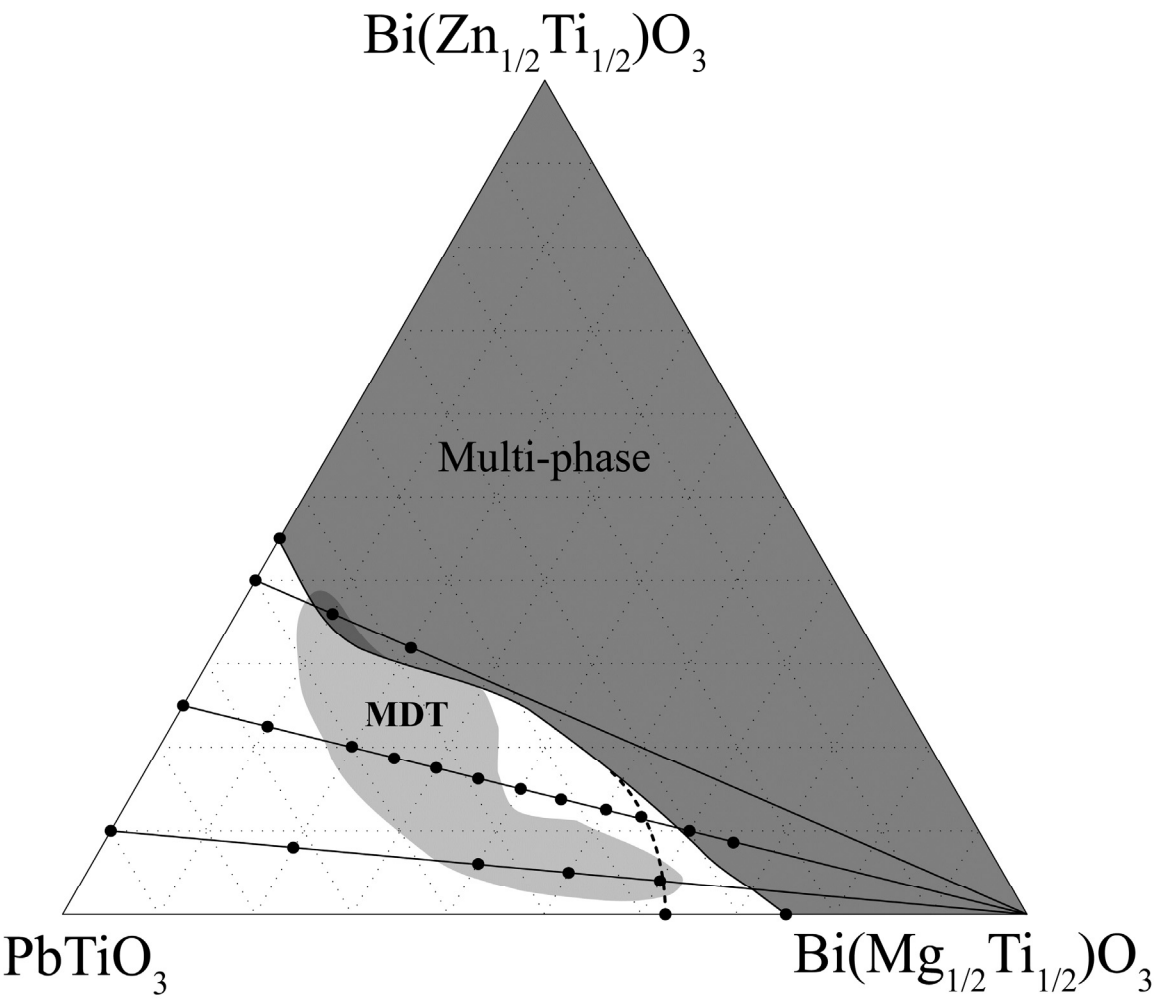

Figure 4.10: Ternary diagram of the PT-BZT-BMT system. Multiple dielectric transitions are observed in the light gray shaded region labeled MDT.

this characterization, pseudo-binary solid solutions with higher BZT content exhibited the behavior at a lower concentration of BMT. There is also some evidence of this behavior in the (1-*x*)PT-(*x*)BMT binary system (*x* = 0.65) published elsewhere [Randall 2004].

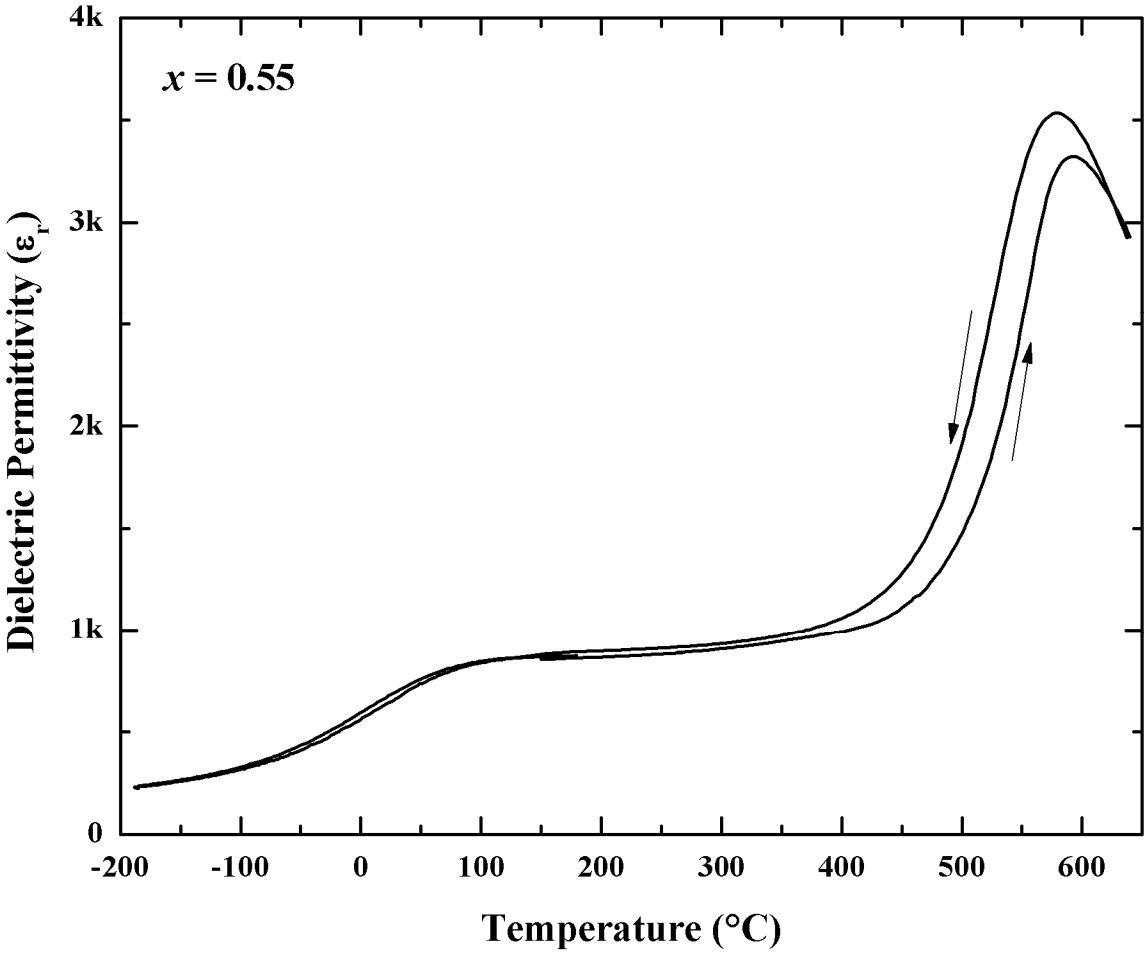

Figure 4.11: Dielectric permittivity of MPB composition (x = 0.55) in the (1-x)[75/25]-(x)BMT solid solution. Both high-temperature and low-temperature dielectric data is included.

4.2.4 Ferroelectric properties and the nature of the MPB

As the study of these ternary systems was undertaken with a view to enhance piezoelectric response, the MPB composition (x = 0.55) in the (1-x)[75/25] – (x)BMT solid solution was investigated further. Low-temperature dielectric response was measured and is shown combined with the high-temperature response data in Figure 4.11. The broad lower temperature dielectric transition is observed at just above room

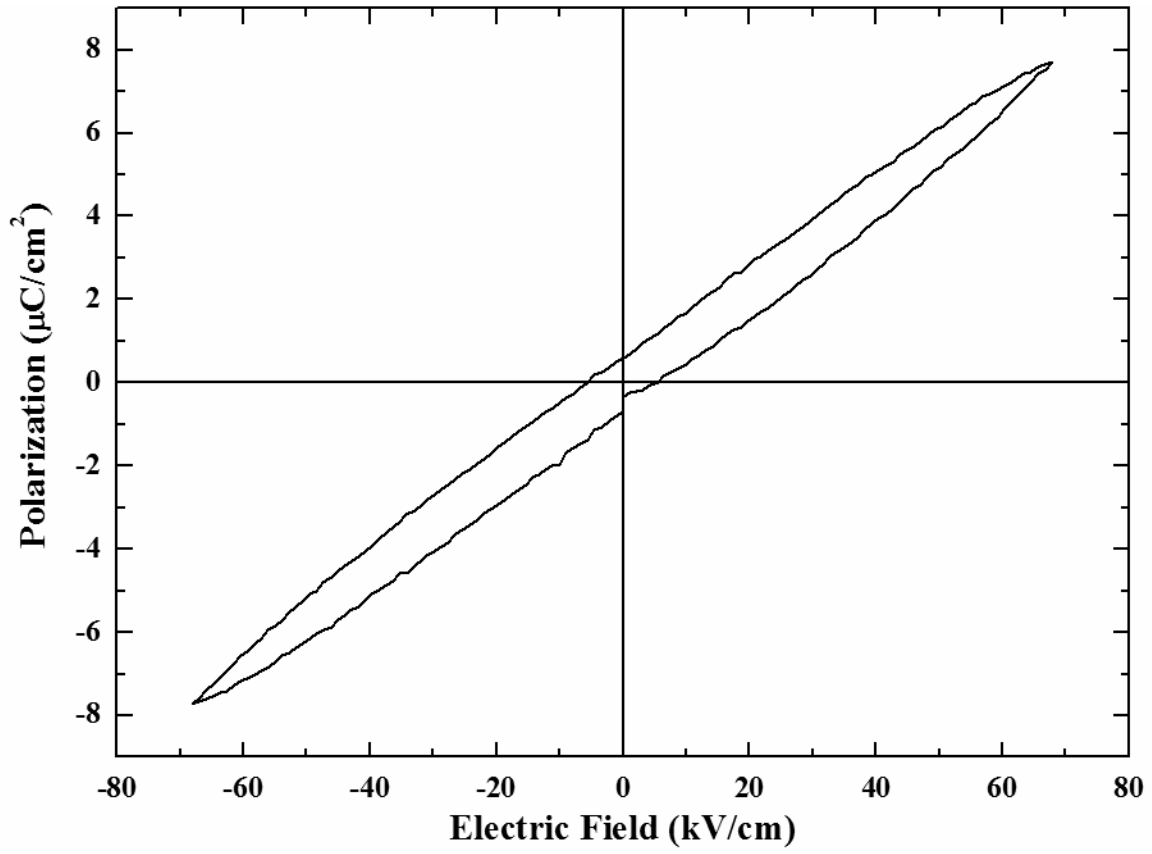

Figure 4.12: Field v. polarization ferroelectric hysteresis curves measured at room temperature for the composition (0.45)[(0.75)PT-(0.25)BZT] – (0.55)BMT.

temperature in the added temperature data. A polarization loop of this composition is shown in Figure 4.12. No significant remnant polarization is observed in the sample and a saturation field was not obtainable experimentally. This behavior is more consistent with relaxor ferroelectrics than traditional ferroelectrics.

It is relatively common to observe relaxor behavior in Bi-containing perovskite systems [Guo 2008, Salak 2008]. However, very little frequency dispersion is observed in this composition at the T_C (<5°C of dispersion between 1kHz and 1Mhz) and relaxor behavior was not expected. This suggested that the lower-temperature dielectric transition

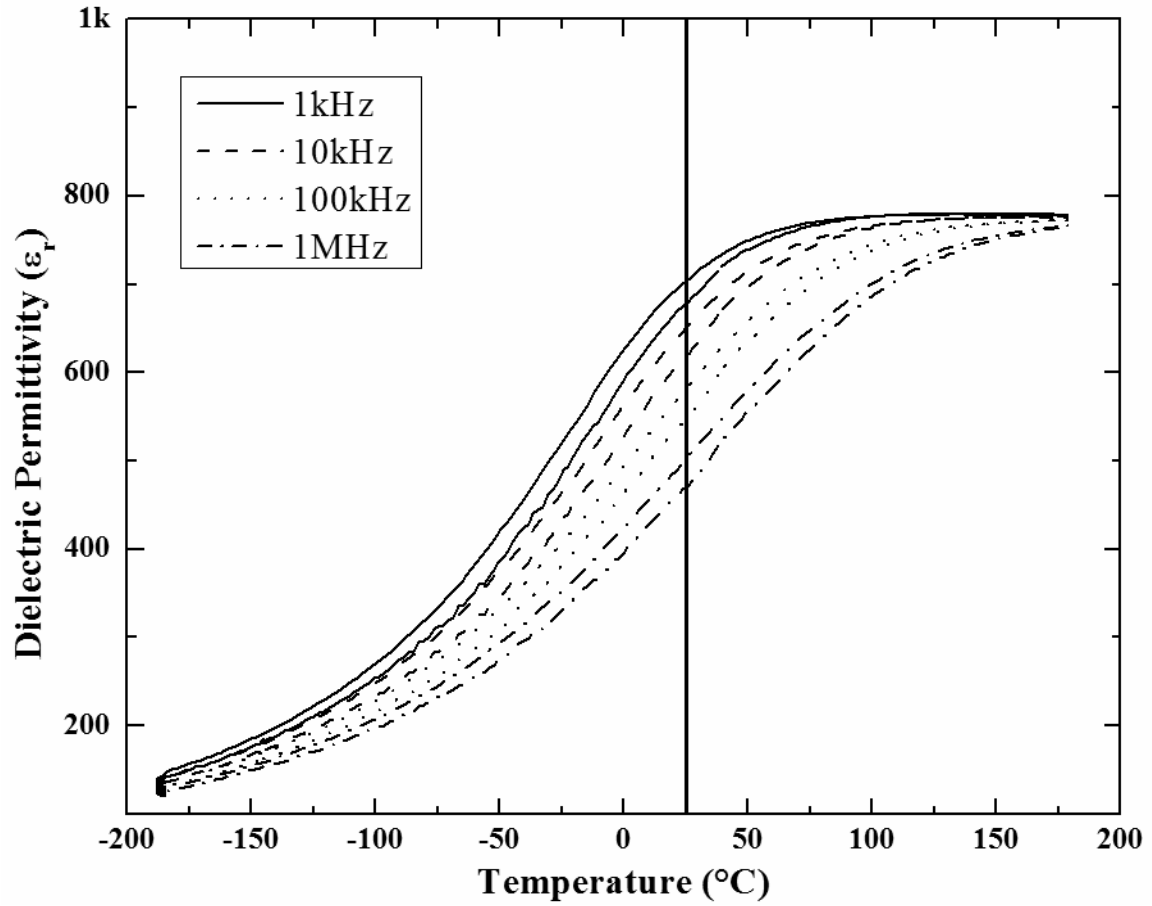

Figure 4.13: Dielectric permittivity response as a function of temperature for the composition (0.45)[75/25] – (0.55)BMT. The vertical black line represents room temperature.

may be associated with a relaxor transition. Indeed, the low-temperature dielectric response (Figure 4.13) exhibits significant frequency dispersion. Dielectric loss data (Figure 4.14) exhibits a maximum at the same temperature ranges, allowing the frequency dispersion to be quantified (45°C between 1kHz and 1MHz). This relaxor-type transition was observed in the other compositions of the [75/25]-BMT line and is plotted as a function of composition in Figure 4.15.

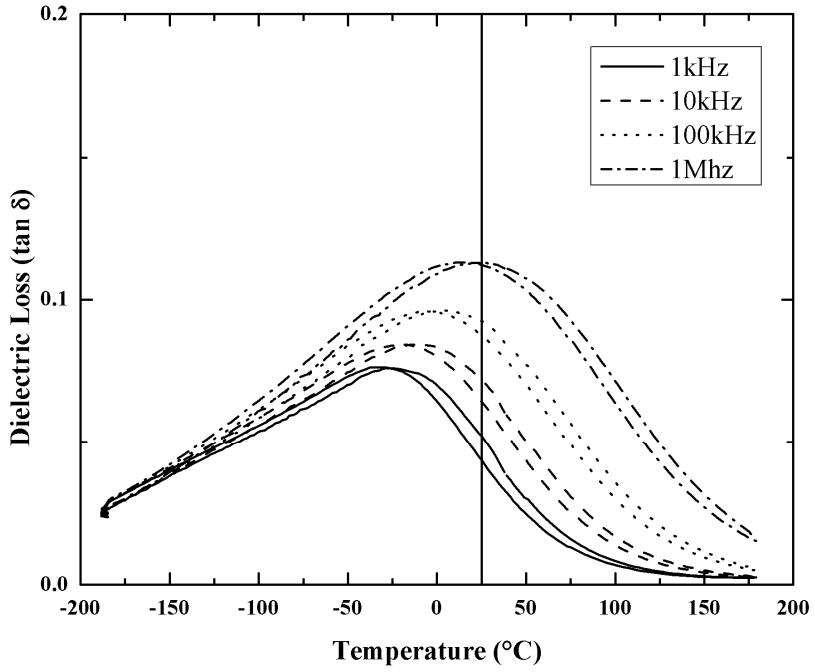

Figure 4.14: Dielectric loss response as a function of temperature for the (0.45)[75/25] – (0.55)BMT composition. The vertical black line represents room temperature.

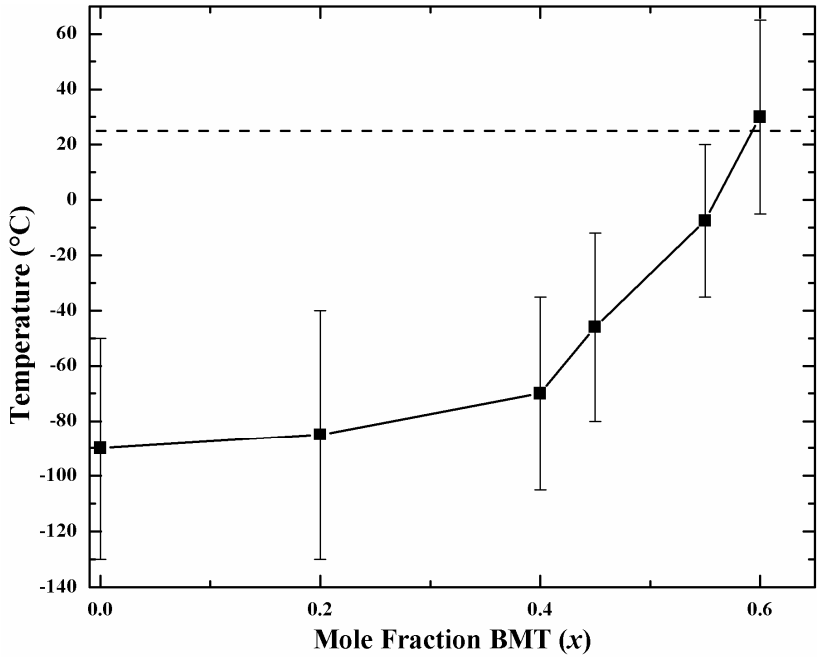

Figure 4.15: Average relaxor-type transition temperature as a function of composition in the (1-*x*)[75/25]-(*x*)BMT solid solution. Whiskers represent the dielectric loss peak temperature at 1kHz and 1Mhz. Dashed horizontal line represents room temperature.

The relaxor-type transition in the (1-*x*)[75/25] – (*x*)BMT solid solution is well below zero for much of the tetragonal (low BMT concentration) portion of the solution but increases to near room-temperature between $x = 0.55$ and 0.6. This is approximately the same range where the MPB is observed via XRD. This suggests that the MPB in the [75/25]-BMT solid solution is between a traditional tetragonal ferroelectric and a relaxor ferroelectric rather than a traditional rhombohedral or orthorhombic ferroelectric. Similar MPB systems between traditional and relaxor ferroelectrics, such as the $PbTiO_3$ – $Pb(Zn_{1/3}Nb_{2/3})O_3$, have exhibited excellent piezoelectric performance [Park 1997]. However, attempts to measure the piezoelectric response in the (0.45)[75/25]-(0.55)BMT composition resulted in no significant response.

4.2.5 High-temperature structural properties

Maxima in the dielectric permittivity are usually associated with a structural transition, however the compositions that exhibit multiple dielectric transition behavior in the PT-BZT-BMT system do not have an obvious structural explanation as the room-temperature structure is tetragonal and only one symmetry transition is accessible (to the paraelectric cubic phase). Still, the observation of thermal hysteresis in these compositions suggests that an unknown structural transition is occurring.

To investigate the structural properties of this ternary system above room-temperature, two compositions with well-spaced dielectric maxima and relatively large maximum permittivities were selected for temperature-dependent diffraction studies. The first composition, (0.5)[90/10] – (0.5)BMT, is tetragonal at room temperature with a *c/a*

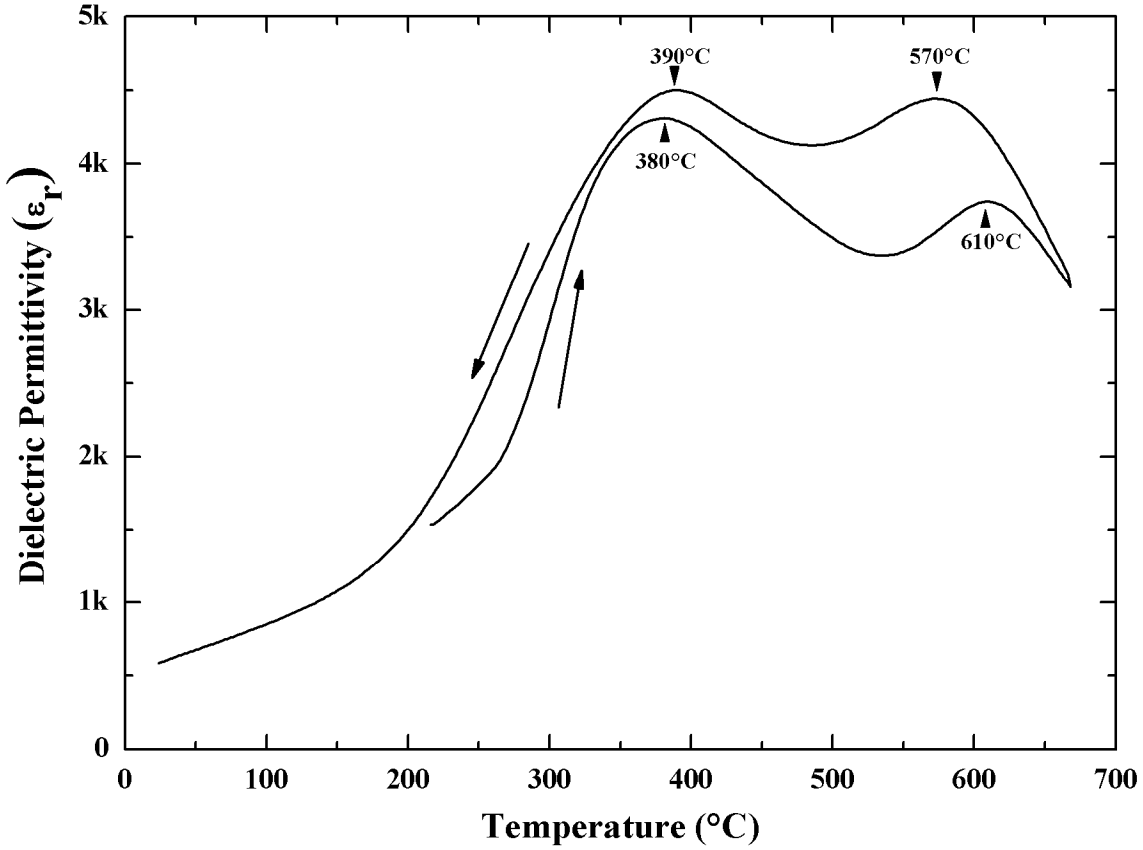

Figure 4.16: Dielectric permittivity response as a function of temperature for [90/10]-BMT50 composition (f = 100kHz). Arrows indicate direction of thermal ramp and dielectric permittivity maxima positions are labeled.

ratio of 1.054. The dielectric response for this composition is shown in Figure 4.16. Dielectric permittivity maxima are located at T = 385ºC and 590ºC with a small hysteresis between heating and cooling cycles (ΔT = 40ºC for the higher temperature maxima). The structural behavior of this composition was studied by neutron powder diffraction from 25 - 900°C, see Figure 4.17. Peaks associated with the stainless steel cap of the sample holder are visible in the patterns at all temperatures. No new peaks were detected from symmetries other than the tetragonal or cubic form of the perovskite.

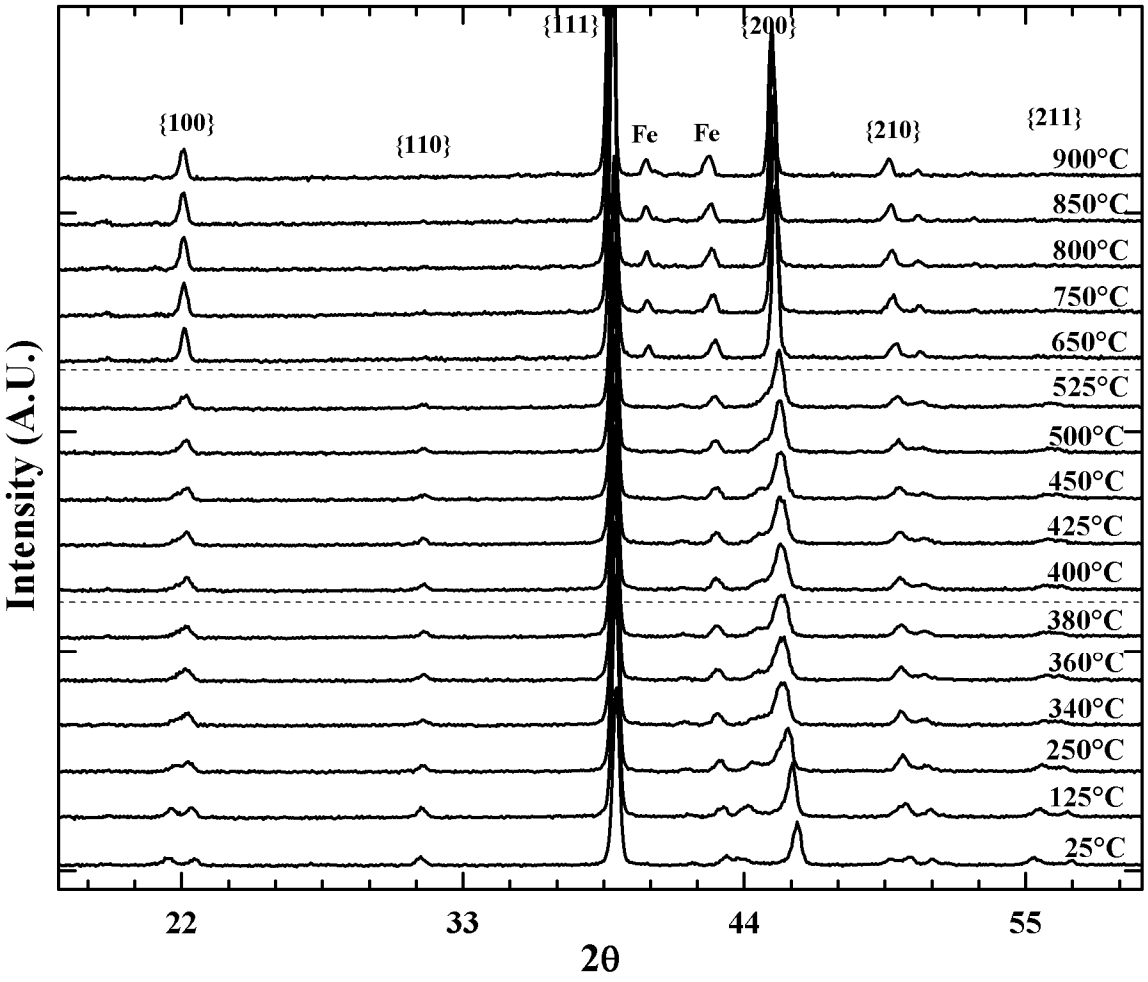

Figure 4.17: Neutron powder diffraction patterns for the (0.5)[90/10]-(0.5)BMT composition for temperatures between 25°C and 900°C. The positions of the dielectric transitions (385ºC and 590ºC) in this composition are represented by the horizontal dashed lines.

The neutron diffraction patterns were modeled using Rietveld refinement techniques. Above the second maximum the diffraction data clearly show the structure is cubic (Pm3m-type). Below the first dielectric maximum, the scattering data can be refined with a P4mm lead titanate-type tetragonal structure, though asymmetric peak

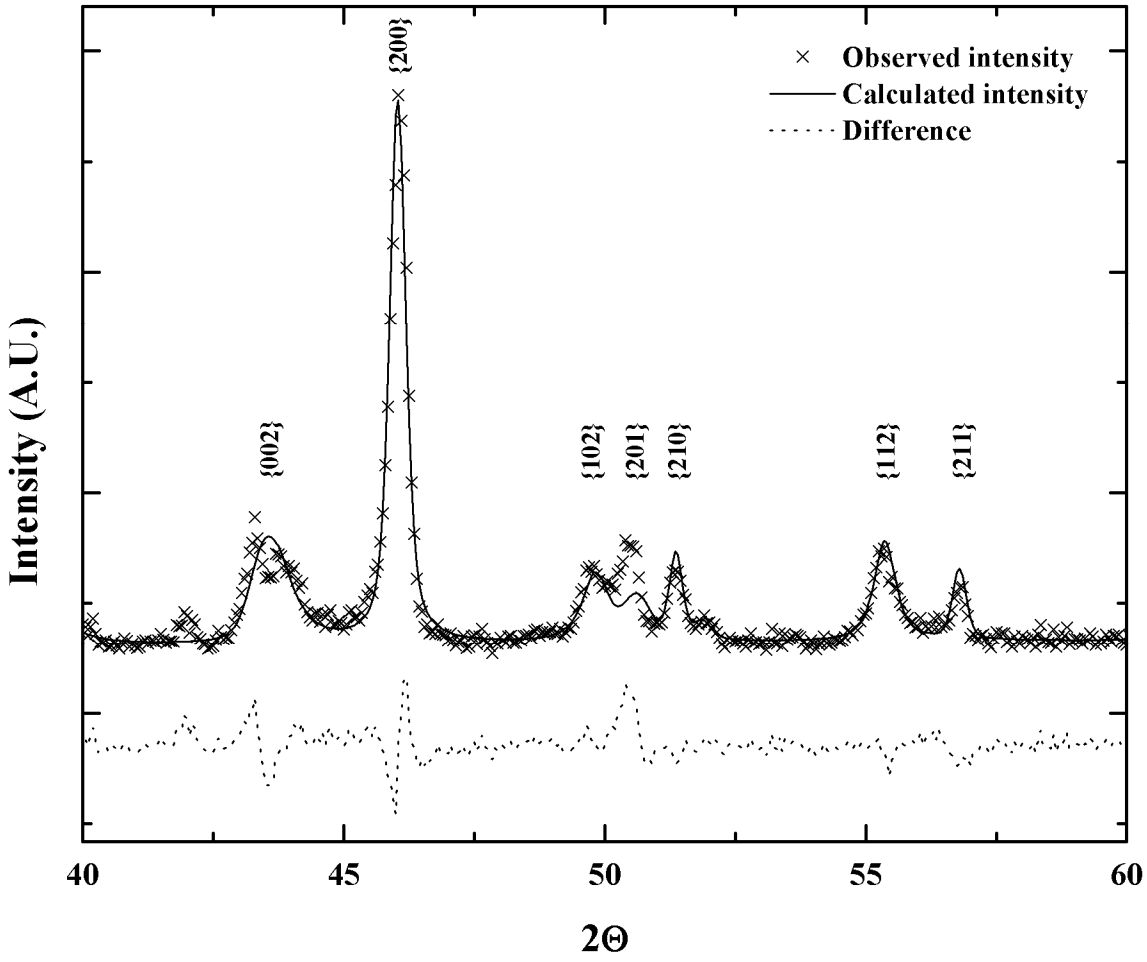

Figure 4.18: Comparison of the observed neutron intensity and the calculated intensities from the Rietveld analysis of the room temperature data from (0.5)[90/10] – (0.5)BMT. Dotted line at the bottom of the figure is the difference plot.

broadening reduced the quality of the fit relative to the high temperature cubic phase (χ^2 = 1.998 at 250ºC v. χ^2 = 1.678 at 800ºC). Figure 4.18 illustrates this broadening in the room temperature neutron data. The model is unable to properly account for observed intensity found between peaks in families split due to the tetragonal symmetry. This broadening is often observed in these highly tetragonal systems and complicates the fitting process particularly in the intermediate temperature range, between the two

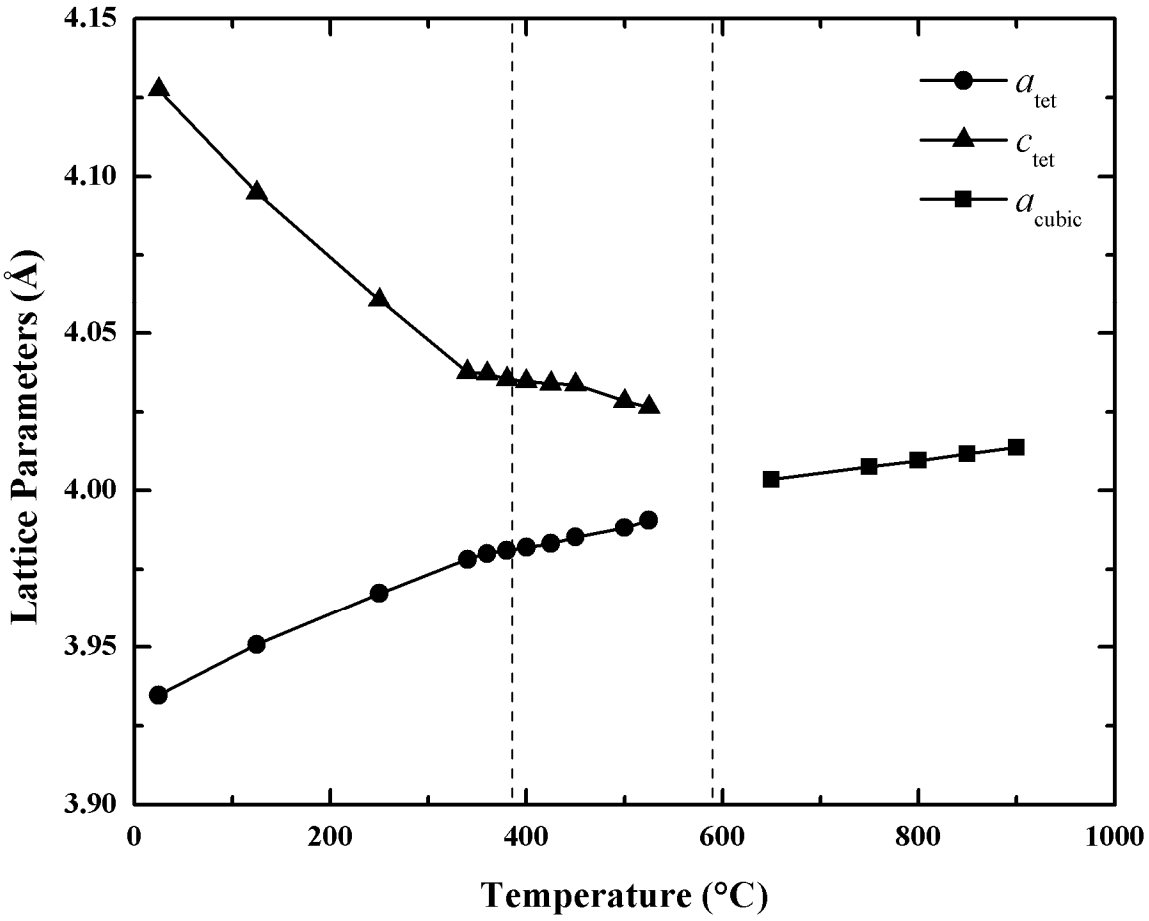

Figure 4.19: Lattice parameters as a function of temperature for the [90/10]-BMT50 composition. Vertical dashed lines represent the dielectric transition temperatures.

dielectric maxima, where it contributes to peak overlap [Grinberg 2007]. Various models (space groups: P4mm, R3c, R3m, Pm3m and 2-phase combinations) were fit to the data, but the best quality of fit was obtained for a single-phase structure with a small tetragonal distortion. The structural parameters and reliability statistics from the Rietveld analysis are listed in Table 4.1 and the lattice parameters derived from these structures are plotted in Figure 4.19 as a function of temperature. With increasing temperature, the *a* and *c* lattice parameters converge (*c/a* decreases) with increasing temperature to approximately

Table 4.1: Refined structural and reliability parameters for the (0.5)[(.9)PT-(0.1)BZT]-(0.5)BMT composition using neutron data.

T	a_{tet} (or a_{cubic})	c_{tet}	U_A	U_B	U_{O1} (or U_O)	U_{O2}	R_F^2	χ^2
°C	Å	Å	x100 Å^2	x100 Å^2	x100 Å^2	x100 Å^2		
25	3.9346	4.1240	0.03360	0.00978	0.03348	0.02556	0.0642	1.454
125	3.9507	4.0930	0.03756	0.01485	0.03520	0.03208	0.0832	1.684
250	3.9665	4.0587	0.04262	0.01348	0.03045	0.03847	0.0731	1.998
340	3.9775	4.0351	0.05033	0.02026	0.03218	0.04230	0.0869	1.868
360	3.9788	4.0342	0.05162	0.01466	0.04055	0.03850	0.0809	1.791
380	3.9803	4.0329	0.05910	0.01639	0.03334	0.04264	0.0908	1.785
400	3.9813	4.0325	0.04955	0.01317	0.04876	0.04052	0.0915	1.732
425	3.9827	4.0323	0.05193	0.01086	0.05606	0.03798	0.0969	1.690
450	3.9847	4.0321	0.06004	0.00398	0.03113	0.04272	0.0759	1.655
500	3.9882	4.0283	0.07467	0.00972	0.03698	0.04159	0.0996	1.597
525	3.9905	4.0264	0.00763	0.00897	0.02837	0.05009	0.1047	1.573
650	4.0035	-	0.10578	0.07758	0.04664	-	0.1528	2.006
750	4.0076	-	0.11211	0.08868	0.04714	-	0.1292	1.780
800	4.0095	-	0.11365	0.09375	0.04800	-	0.1333	1.678
850	4.0116	-	0.11408	0.08993	0.04832	-	0.1286	1.578
900	4.0136	-	0.11691	0.08515	0.04695	-	0.1073	1.638

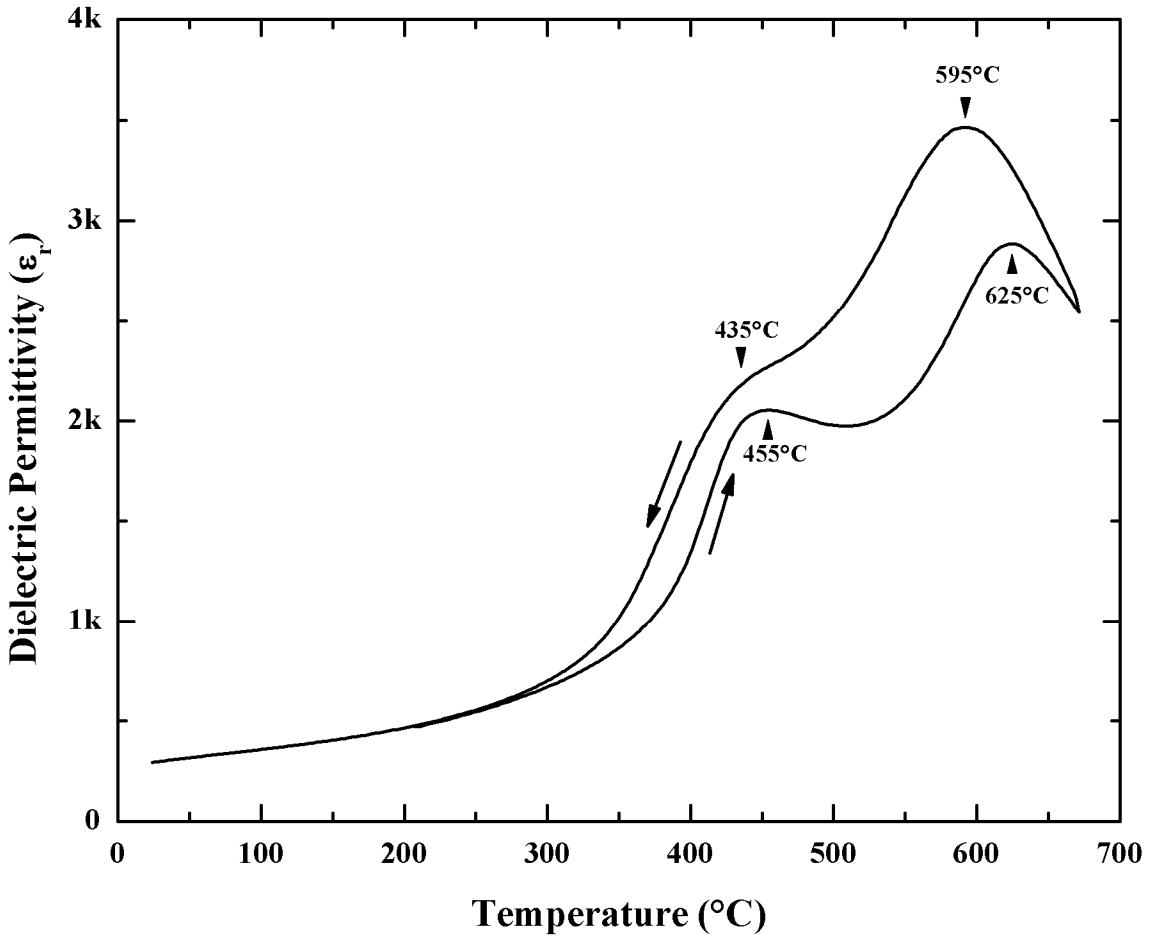

Figure 4.20: Dielectric permittivity as a function of temperature for the composition [75/25]-BMT25 (*f* = 100kHz).

the first dielectric transition. There the structure enters what appears to be a frustrated region of "persistent tetragonality" where the effect of temperature on the contraction of *c* is much weaker. Beyond the higher temperature dielectric maxima the structure transforms to a well-fit cubic phase.

The high-temperature structure of a second composition, (0.75)[75/25]-(0.25)BMT, was also investigated, in this case using synchrotron X-rays rather than neutrons. This composition has a higher concentration of Zn^{2+} and lower concentration of

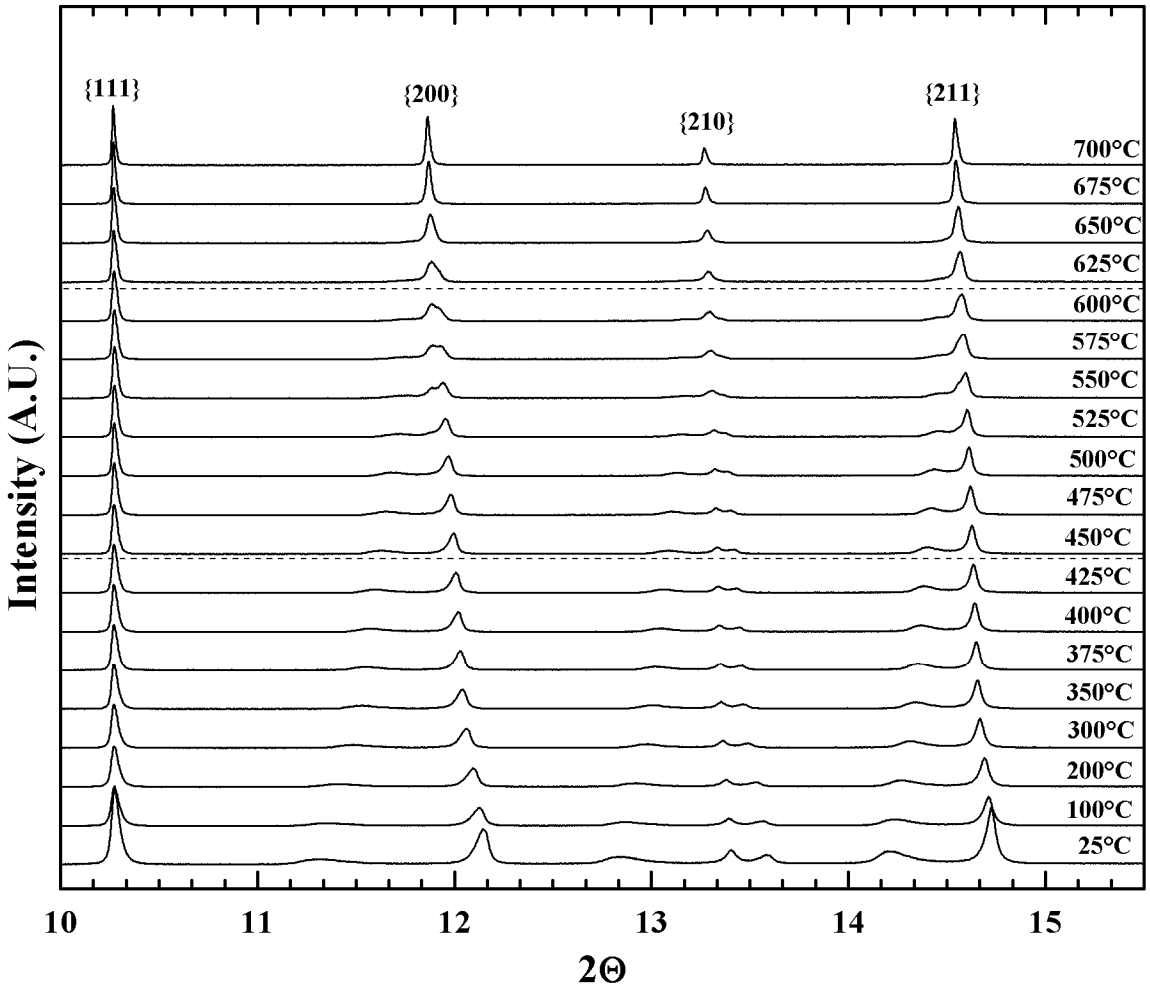

Figure 4.21: Synchrotron powder diffraction patterns for the (0.75)[75/25]-(0.25)BMT composition for temperatures between 25°C and 700°C. The positions of the dielectric transition in this composition (445ºC and 610ºC) are represented by the horizontal dashed lines.

Bi^{3+} relative to the (0.5)[90/10] – (0.5)BMT composition. At room temperature the sample has a larger *c/a* ratio (1.070 v. 1.054) and dielectric transitions at 445ºC and 610ºC, see Figure 4.20. The diffraction data is shown in Figure 4.21. Similar to the previous composition, (0.75)[75/25]-(0.25)BMT is free from non-perovskite phases at all temperatures.

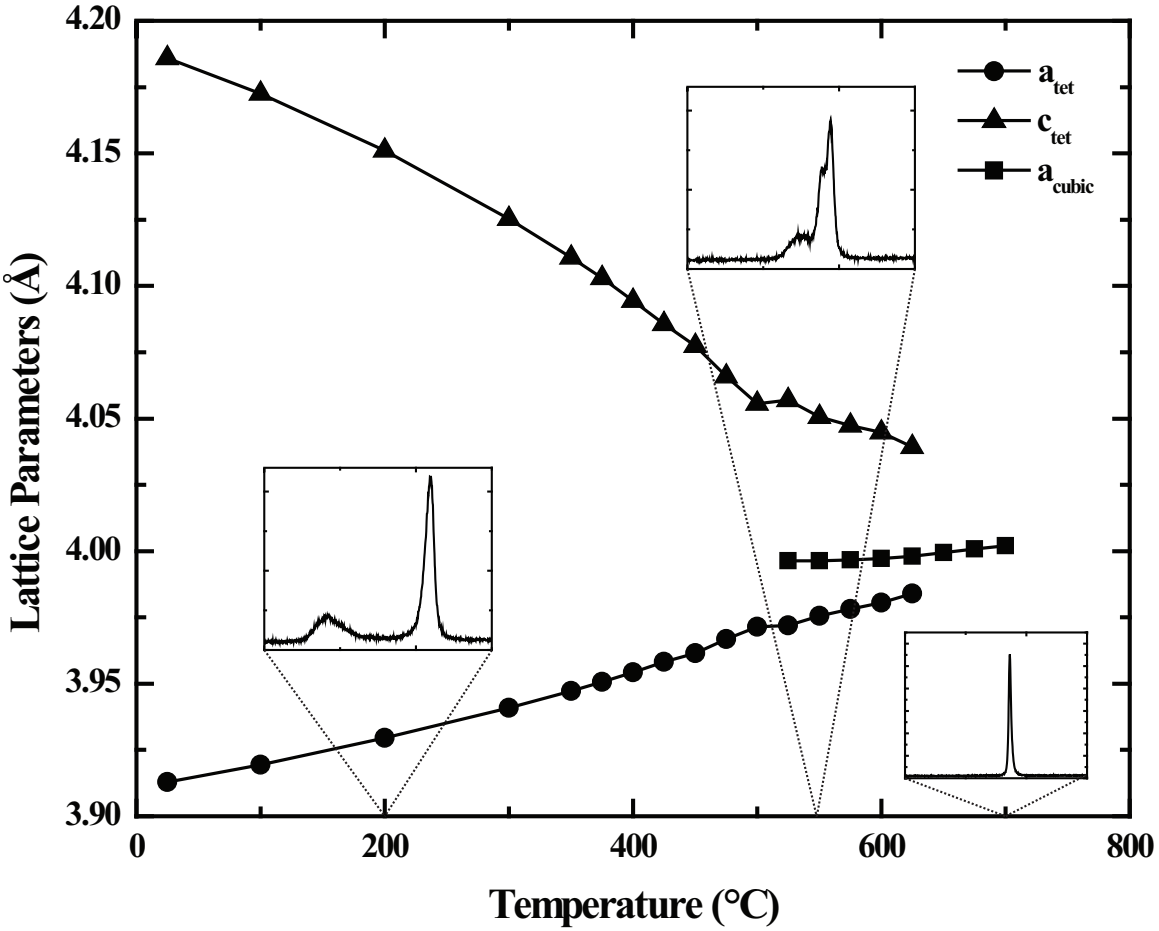

Figure 4.22: Lattice parameters as a function of temperature for the [90/10]-BMT50 composition. Insets plot the evolution of the {200} family of peaks at representative temperatures.

Rietveld refinement analysis of the diffraction data revealed that all temperatures the structure can be well modeled by tetragonal (P4mm) and cubic (Pm3m) perovskites or a combination of the two. Temperature-dependent lattice parameters for (0.75)[75/25]-(0.25)BMT are plotted in Figure 4.22; the structural parameters and reliability statistics for the tetragonal and cubic structures are listed in Tables 4.2 and 4.3, respectively. The composition is single-phase tetragonal from room temperature until 525ºC where peaks from a cubic modification are first resolved. The *c/a* of the tetragonal phase decreases

Table 4.2: Refined structural and reliability parameters for the tetragonal phase of the (0.75)[(.75)PT-(0.25)BZT]-(0.25)BMT composition at relevant temperatures using neutron data.

T	a_{tet}	c_{tet}	U_A^T	U_B^T	U_{O1}^T	U_{O2}^T	R_F^2	χ^2
°C	Å	Å	x100 Å^2	x100 Å^2	x100 Å^2	x100 Å^2		
25	3.9123	4.1861	0.02751	0.00598	0.03083	0.01705	0.1138	7.446
100	3.9192	4.1711	0.03011	0.00410	0.03720	0.01657	0.1450	5.652
200	3.9280	4.1502	0.03398	0.00769	0.08755	0.07335	0.0955	4.285
300	3.9406	4.1244	0.03861	0.00570	0.03916	0.00971	0.1699	5.712
350	3.9470	4.1098	0.04092	0.00683	0.04755	0.01191	0.1663	5.897
375	3.9503	4.1023	0.04217	0.00760	0.05620	0.01118	0.1595	5.917
400	3.9534	4.0957	0.04358	0.00826	0.05067	0.14087	0.1627	5.148
425	3.9572	4.0873	0.03172	0.00873	0.03073	0.16441	0.2345	8.022
450	3.9615	4.0774	0.04845	0.01061	0.00468	0.08131	0.1526	4.448
475	3.9659	4.0675	0.05059	0.01033	0.00441	0.08791	0.1636	4.465
500	3.9706	4.0568	0.05371	0.01217	0.00208	0.10731	0.1679	4.442
525	3.9720	4.0569	0.05413	0.01623	0.06953	0.03686	0.2075	5.487
550	3.9760	4.0501	0.04173	0.01962	0.06434	0.00146	0.2903	4.804
575	3.9784	4.0472	0.06124	0.00015	0.07108	0.05165	0.2071	4.093
600	3.9807	4.0450	0.06100	0.00470	0.07514	0.03074	0.1945	3.838
625	3.9838	4.0401	0.06375	0.00556	0.06392	0.04200	0.2446	3.552

Table 4.3: Refined structural and reliability parameters for the cubic phase of the (0.75)[(.75)PT-(0.25)BZT]-(0.25)BMT composition at relevant temperatures using neutron data.

T	A_{cubic}	U_A^C	U_B^C	U_O^C	R_F^2	χ^2
°C	Å	x100 Å^2	x100 Å^2	x100 Å^2		
525	3.9963	0.06315	0.00987	0.51991	0.2075	5.487
550	3.9967	0.08202	0.04278	0.07774	0.2903	4.804
575	3.9968	0.06800	0.01979	0.06521	0.2071	4.093
600	3.9973	0.07044	0.01770	0.05689	0.1945	3.838
625	3.9981	0.07004	0.01703	0.05130	0.2446	3.552
650	3.9995	0.07002	0.01963	0.06714	0.1397	4.388
675	4.0009	0.07610	0.02199	0.04797	0.1020	4.494
700	4.0013	0.07814	0.02287	0.04727	0.1655	4.091

with increasing temperature from room temperature until it reaches 1.014 at 625ºC. Above that temperature no tetragonal phase is observed and the structure is cubic. The region of 2-phase coexistence is first observed at a temperature higher than the first dielectric transition (525ºC v. 445ºC) and persists to a temperature that is slightly higher than the "averaged" second dielectric transition (625ºC v. 610ºC) but consistent with the thermal hysteresis of the dielectric response.

The two-phase coexistence in (0.75)[75/25] – (0.25)BMT is superficially different to the "persistent tetragonality" observed in (0.5)[90/10] – (0.5)BMT. However, the asymmetric peak broadening in the tetragonal structure leaves open the possibility of an unresolvable cubic phase in the (0.5)[90/10] – (0.5)BMT composition. It should be noted

that the resolution of the synchrotron data is greater than the data collected using neutrons. An explicit 2-phase model applied to the neutron profiles showed no statistical improvement over a single tetragonal phase. It is also possible the differing macroscopic structural behavior is related to the Bi:Pb content; (0.5)[90/10] – (0.5)BMT has a larger concentration of Bi^{3+} cations than (0.75)[75/25] – (0.25)BMT. For example, if the tetragonal regions at elevated temperatures are associated with Bi^{3+}-rich unit cells and the cubic phase with Pb^{2+}-rich regions the higher Bi concentration may be influencing the macroscopic symmetry observed by diffraction.

In both compositions investigated, the high temperature dielectric maximum is associated with the transition of a ferroelectric tetragonal phase to a paraelectric cubic phase (i.e. a Curie temperature). If the structural behavior of these two compositions is consistent throughout the pseudo-binary solid solutions investigated, the PT-BZT-BMT ternary system exhibits MPB compositions with T_Cs significantly higher (~150°C) than previously reported systems.

In the next section, the effect of an alternate MBP-forming additive, $Bi(Mg_{1/2}Zr_{1/2})O_3$, on PT-BZT is investigated and compared to PT-BZT-BMT and the previously reported PT-BZT-$BiScO_3$ ternary system [Suchomel 2005].

4.3 Other BZT-containing ternary systems

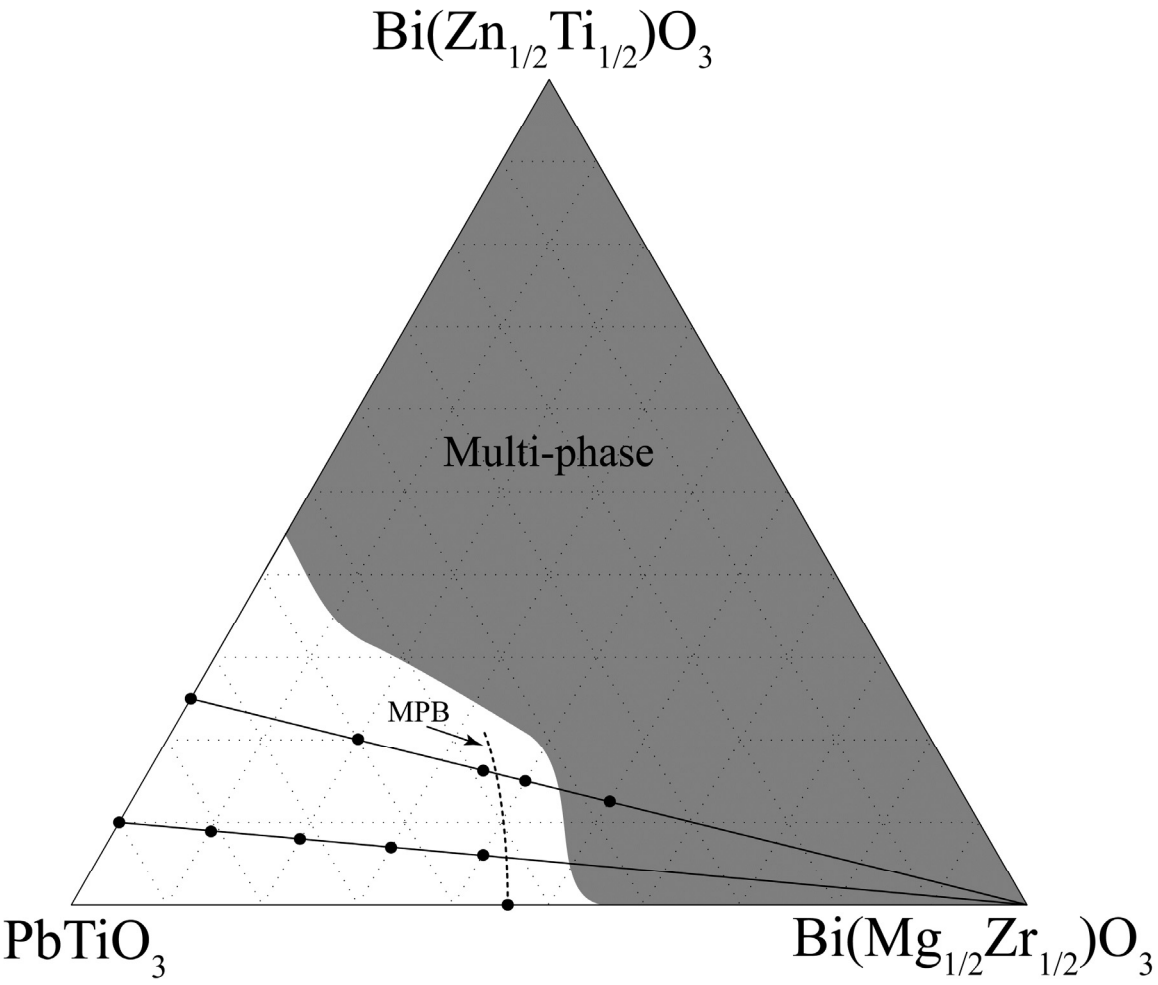

Figure 4.23: PT-BZT-BMZ ternary diagram. Synthesized compositions and MPB are marked.

The data in the previous section demonstrates that BZT induces a complex dielectric response with multiple permittivity maxima when it is substituted into the high-T_C PT-BMT binary system. This section investigates the PT – BZT – $Bi(Mg_{1/2}Zr_{1/2})O_3$ system and also revisits the results of the previously reported PT-BZT-$BiScO_3$ system.

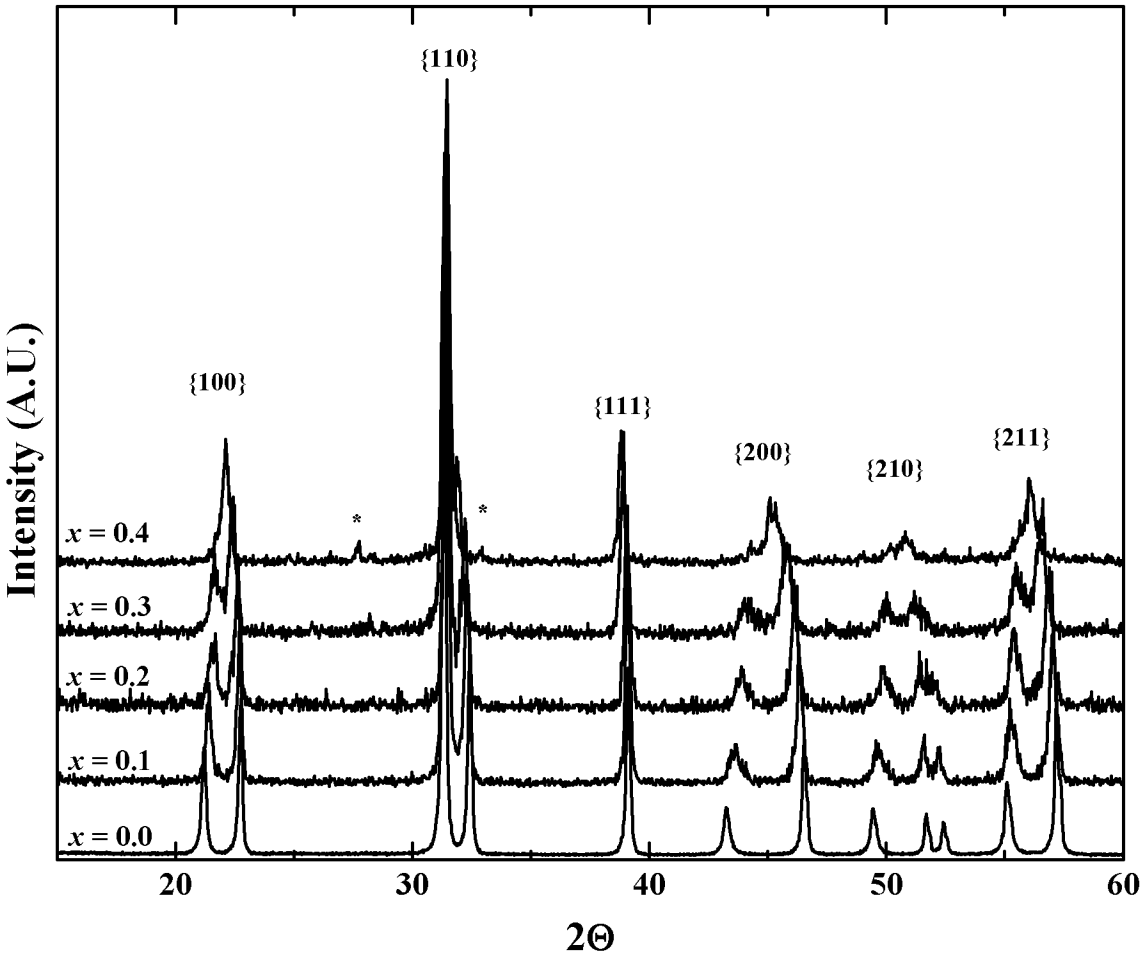

Figure 4.24: XRD patterns of compositions in the (1-*x*)[(0.9)PT – (0.1)BZT] – (*x*)BMZ solid solution. Families of perovskite peaks are labeled. Peaks denoted with a '*' represent impurity phases.

Because it has a lower tolerance factor, $Bi(Mg_{1/2}Zr_{1/2})O_3$ (BMZ) induces the formation of a MPB with PT at a relatively small substitution level of 40% BMZ; the MPB is significantly more PT-rich than the PT-BMT system [Suchomel 2004]. However, at the MPB, the T_C is much lower in PT-BMZ system compared to either PT-BMT or PZT (~300°C v. 425°C and 385°C, respectively). This was attributed to the replacement of Ti^{4+} by Zr^{4+}, a cation that is both larger (0.605Å v 0.72Å) and less ferroelectrically-active (0.13Å v 0.25Å).

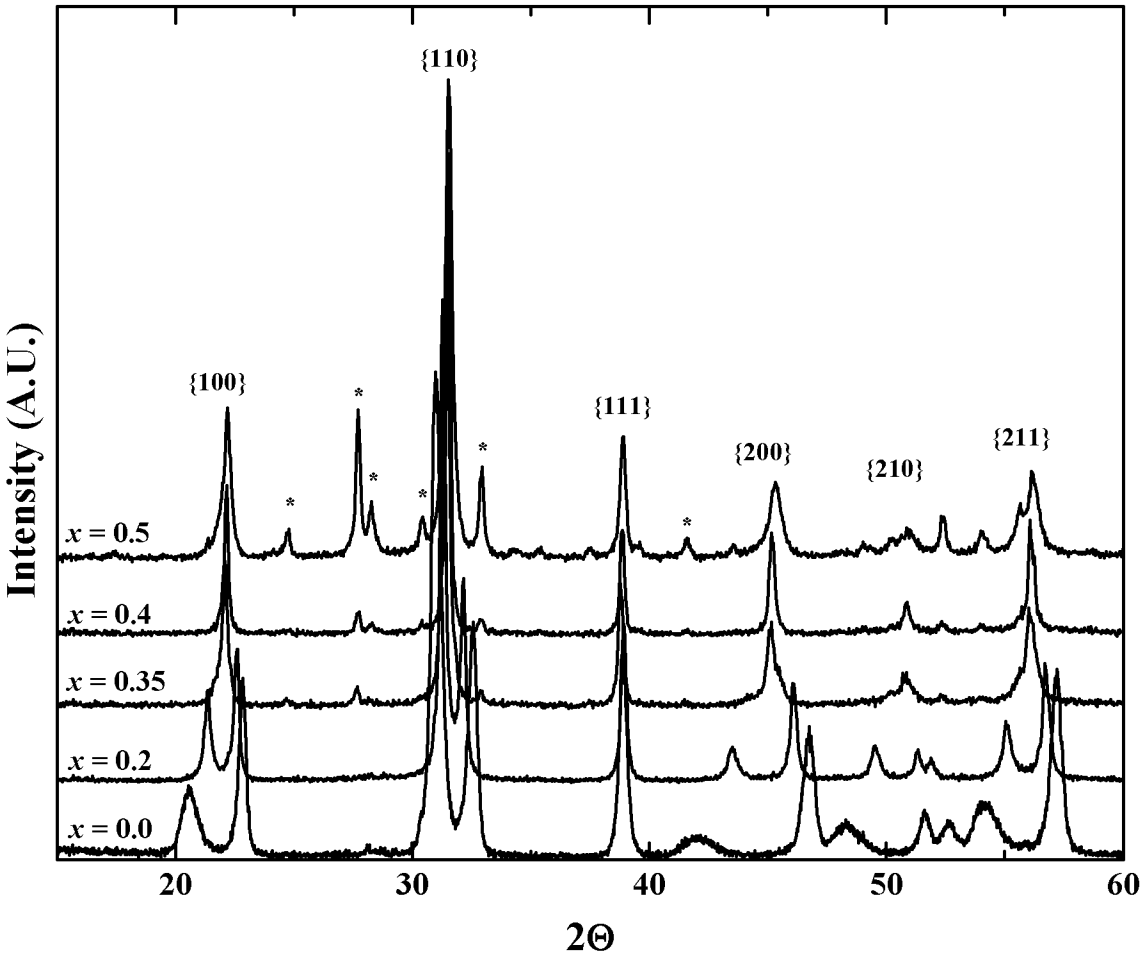

Figure 4.25: XRD patterns of compositions in the (1-*x*)[(0.75)PT – (0.25)BZT] – (*x*)BMZ solid solution. Families of perovskite peaks are labeled. Peaks denoted with a '*' represent impurity phases.

4.3.1 Room temperature structural properties

Compositions in the PT-BZT-BMZ ternary system (Figure 4.23) were synthesized at temperatures between 800°C and 1050°C along the (1-*x*)[(0.9)PT-(0.1)BZT]-(*x*)BMZ and the (1-*x*)[(0.75)PT-(0.25)BZT]-(*x*)BMZ pseudo-binary lines. The diffraction data for the two pseudo-binary lines is compiled in Figures 4.24 and 4.25. Predominantly single-phase samples, with small impurity peaks visible, were prepared for compositions up to

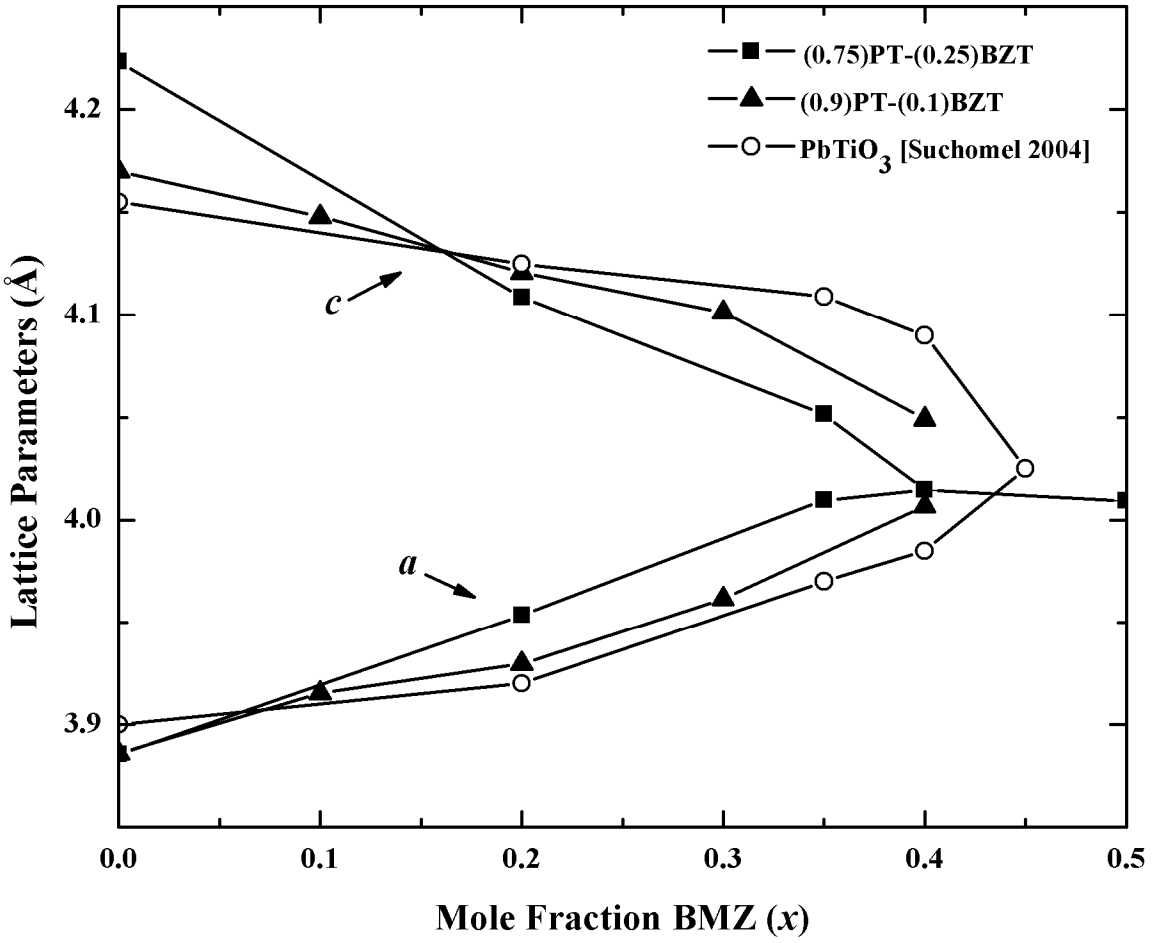

Figure 4.26: Lattice parameters as a function of BMZ substitution for the (1-*x*)[(0.75)PT-(0.25)BZT]-(*x*)BMZ (25% BZT) and (1-*x*)[(0.9)PT-(0.1)BZT]-(*x*)BMZ (10% BZT) solid solutions as well as the binary PT-BMZ system reproduced from [Suchomel 2004].

x = 0.4 in the (1-x)[90/10] – (x)BMZ solid solution. The perovskite phase maintains a slight tetragonal distortion in the x = 0.4 composition, suggesting the MPB lies at slightly higher BMZ substitutions. In the (1-x)[75/25] – (x)BMZ line small impurity peaks are observed in the x = 0.35 and x = 0.4 compositions, but the perovskite structure continues to change with composition, suggesting that BMZ is still entering the structure. Samples with x = 0.5 exhibit a significant fraction of impurities and attempts to prepare compositions with x > 0.5 resulted in even larger relative fractions of secondary phases.

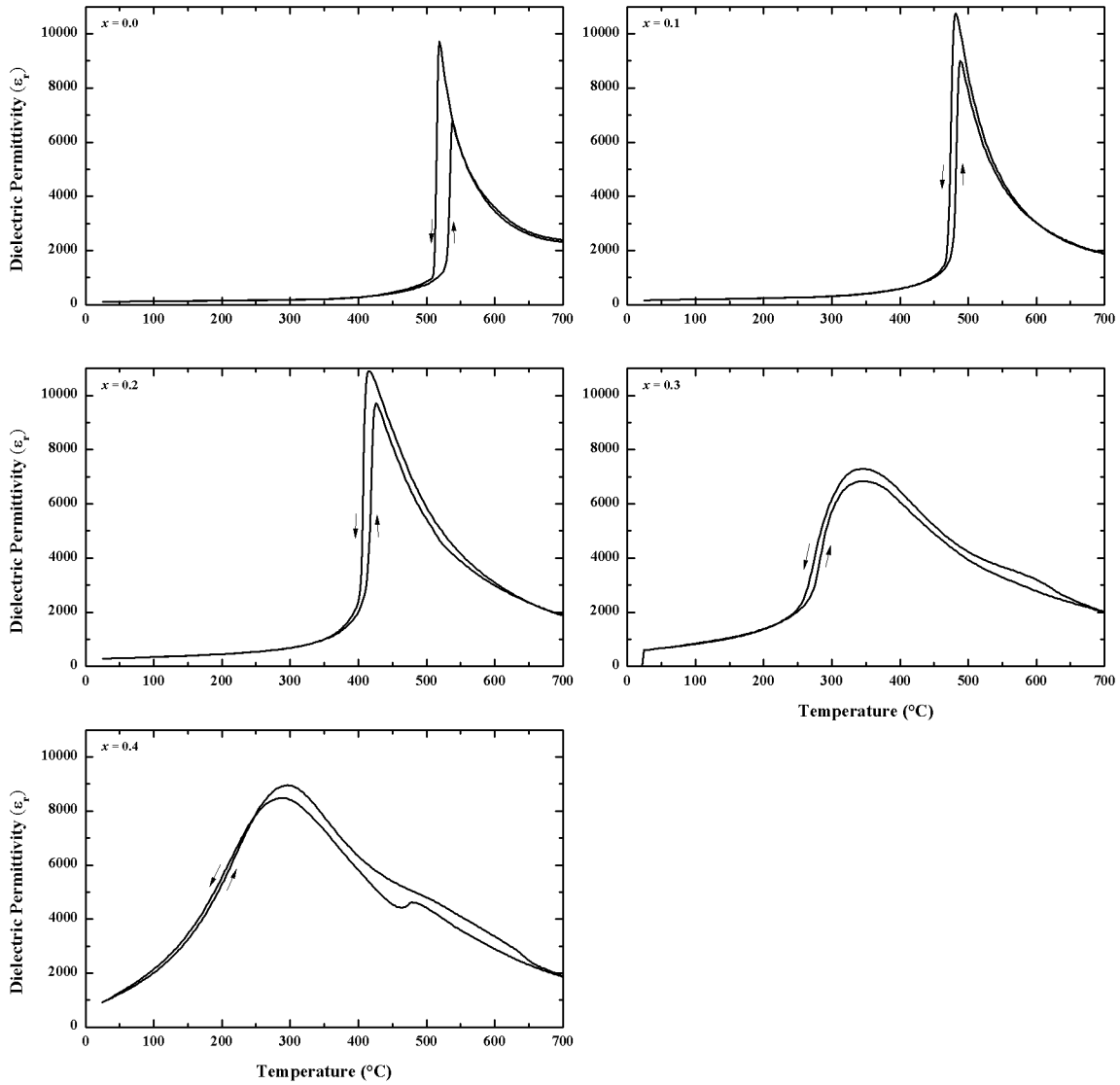

Figure 4.27: Dielectric response as a function of temperature for compositions in the (1-*x*)[90/10] – (*x*)BMZ solid solution (f = 100kHz). Arrows indicate direction of thermal ramp.

The lattice parameters as a function of composition for the two pseudo-binary solid solutions and the previously reported PT-BMZ binary system are shown in Figure 4.26. All three solid solutions form MPBs with sufficient BMZ substitution. The MPB in the binary PT-BMZ system is located near 45% BMZ, while the (1-*x*)[90/10] – (*x*)BMZ line

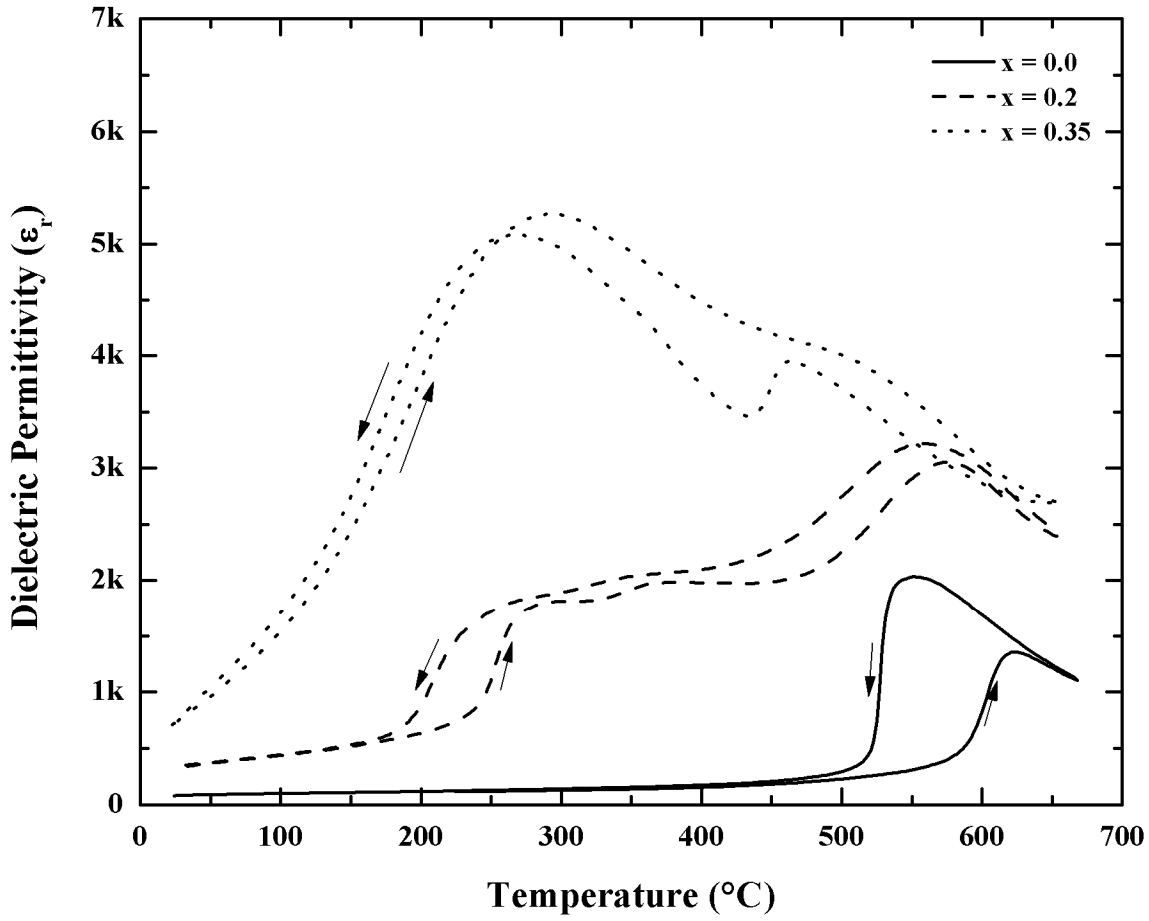

Figure 4.28: Dielectric response as a function of temperature for compositions in the [(0.75)PT-(0.25)BZT]-BMZ solid solution (*f* = 100kHz). Arrows indicate direction of thermal ramp.

forms an MPB at just beyond 40% BMZ and (1-*x*)[75/25] – (*x*)BMZ exhibits an MPB at or before 40% BMZ. The PT-BZT-BMZ system is therefore similar to the PT-BZT-BMT system: in the higher tetragonality end-member, smaller concentrations of the MPB-forming additive are necessary to induce the MPB.

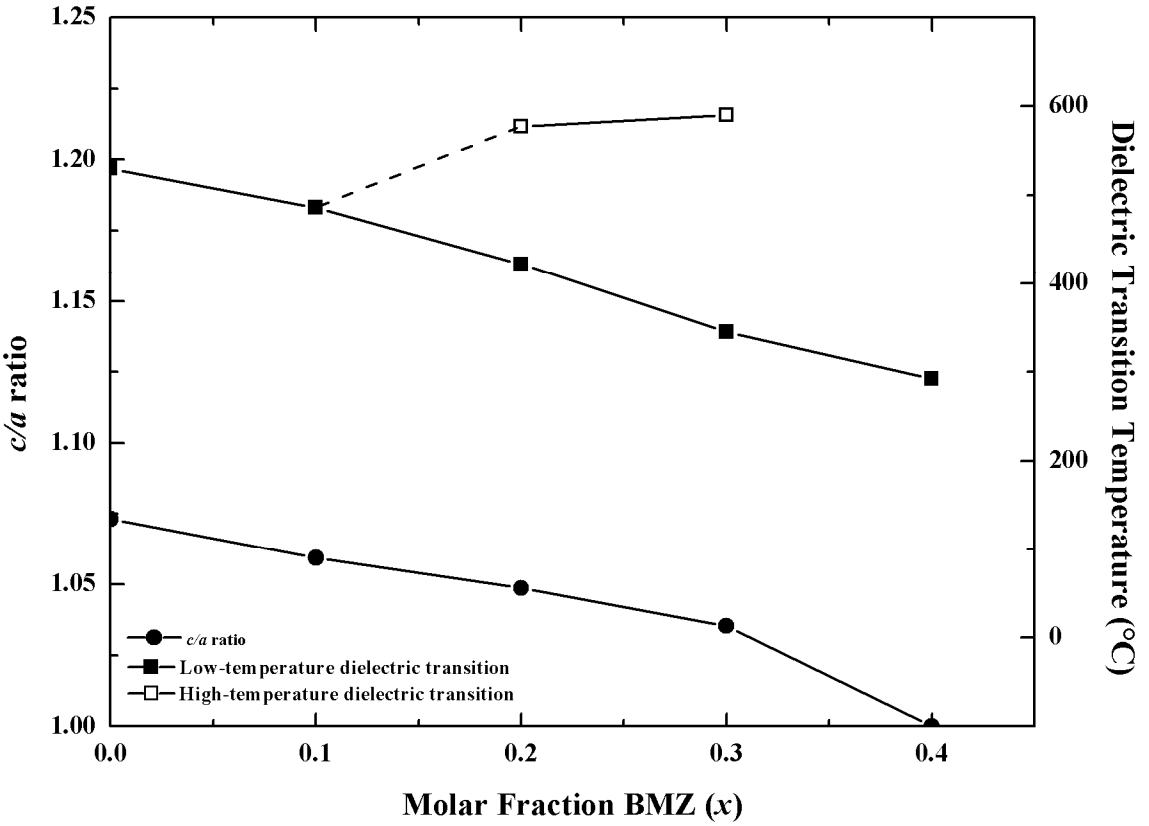

Figure 4.29: *c/a* ratio and dielectric transition temperatures as a function of composition in the (1-*x*)[90/10] – (*x*)BMZ solid solution.

4.3.2 Dielectric properties

The dielectric response of the (1-*x*)[90/10] – (*x*)BMZ and (1-*x*)[75/25] – (*x*)BMZ solid-solutions are shown in Figure 4.27 and Figure 4.28, respectively. As the concentration of BMZ in (1-*x*)[90/10] – (*x*)BMZ increases the dielectric peak broadens significantly and shifts to lower temperatures. The T_C is reduced to ~292°C for $x = 0.4$, down from 530°C in the (0.9)PT – (0.1)BZT end-member. Shoulders are observed on the high-temperature side of dielectric permittivity peaks in the $x = 0.3$ and 0.4 compositions, suggesting multiple dielectric transition behavior. The maximum permittivity in those

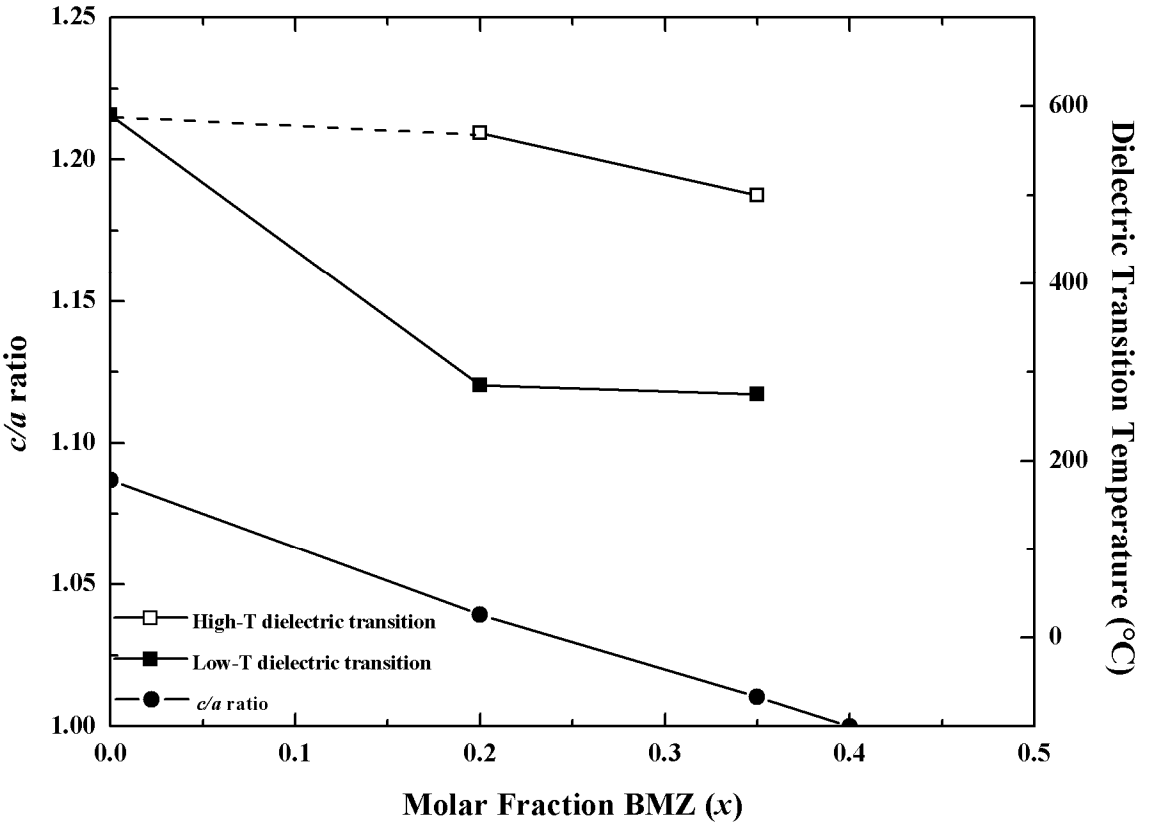

Figure 4.30: *c/a* ratio and dielectric transition temperatures as a function of composition in the (1-*x*)[75/25] – (*x*)BMZ solid solution.

compositions are large enough and the peaks broad enough that it is unlikely the high temperature dielectric transition would be well-resolved.

For the (1-*x*)[75/25] – (*x*)BMZ line dielectric permittivity data was only collected on compositions up to $x = 0.35$. The substitution of BMZ into the solution enhances the maximum permittivity of the system, though these values are significantly lower than the values in the (1-*x*)[90/10] – (*x*)BMZ line. Both BMZ- containing samples exhibit multiple dielectric transitions, with the $x = 0.2$ composition appearing to exhibit an extra peak (three total) compared to other multiple dielectric transition compositions. Between the $x = 0.2$ and 0.35 compositions the permittivity of the low-temperature transition increases

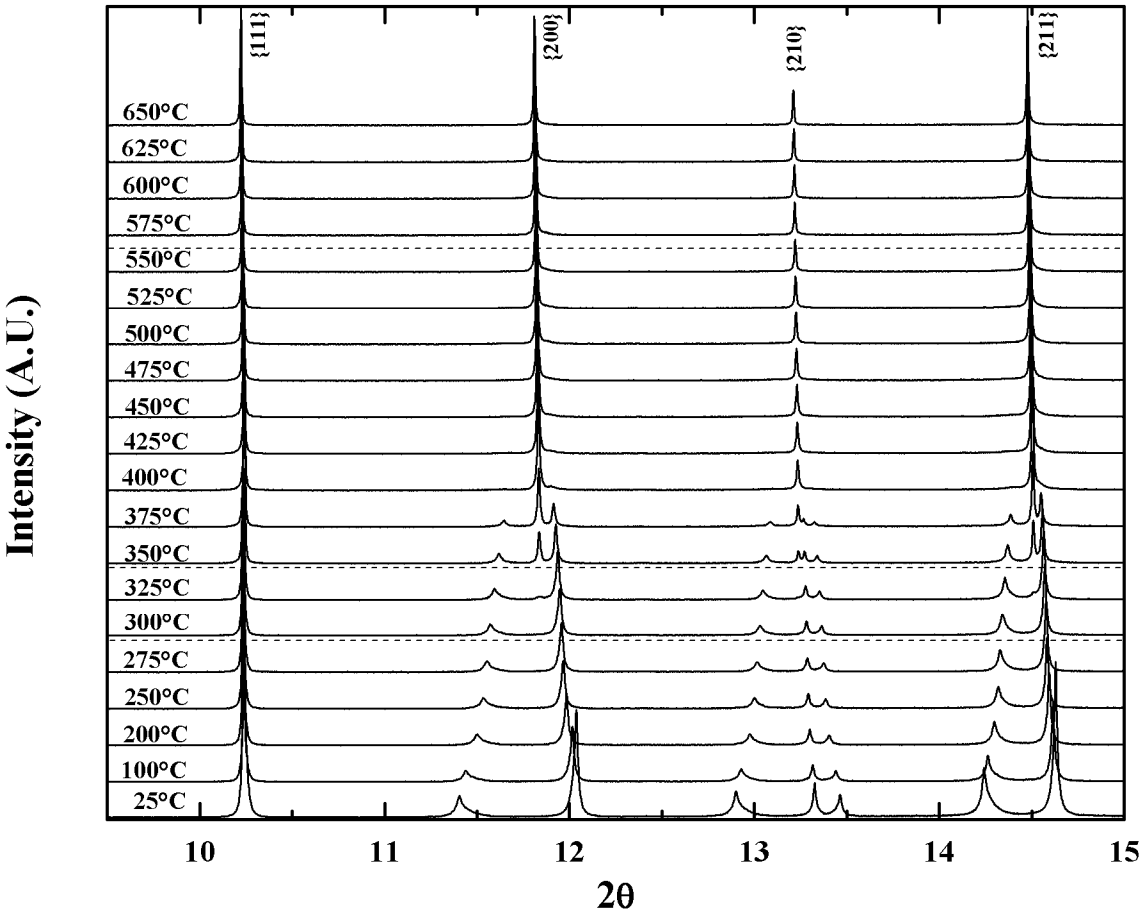

Figure 4.31: Synchrotron powder diffraction patterns for the (0.8)[75/25]-(0.2)BMZ composition for temperatures between 25°C and 650°C. The positions of the dielectric transition in this composition are represented by the horizontal dashed lines.

to a value larger than the high-temperature transition, suggesting an association with the Zr^{4+} content.

The systematic variation of these dielectric transitions with the BMZ content is shown for the (1-*x*)[90/10] – (*x*)BMZ and (1-*x*)[75/25] – (*x*)BMZ solid solutions in Figures 4.29 and 4.30, respectively.

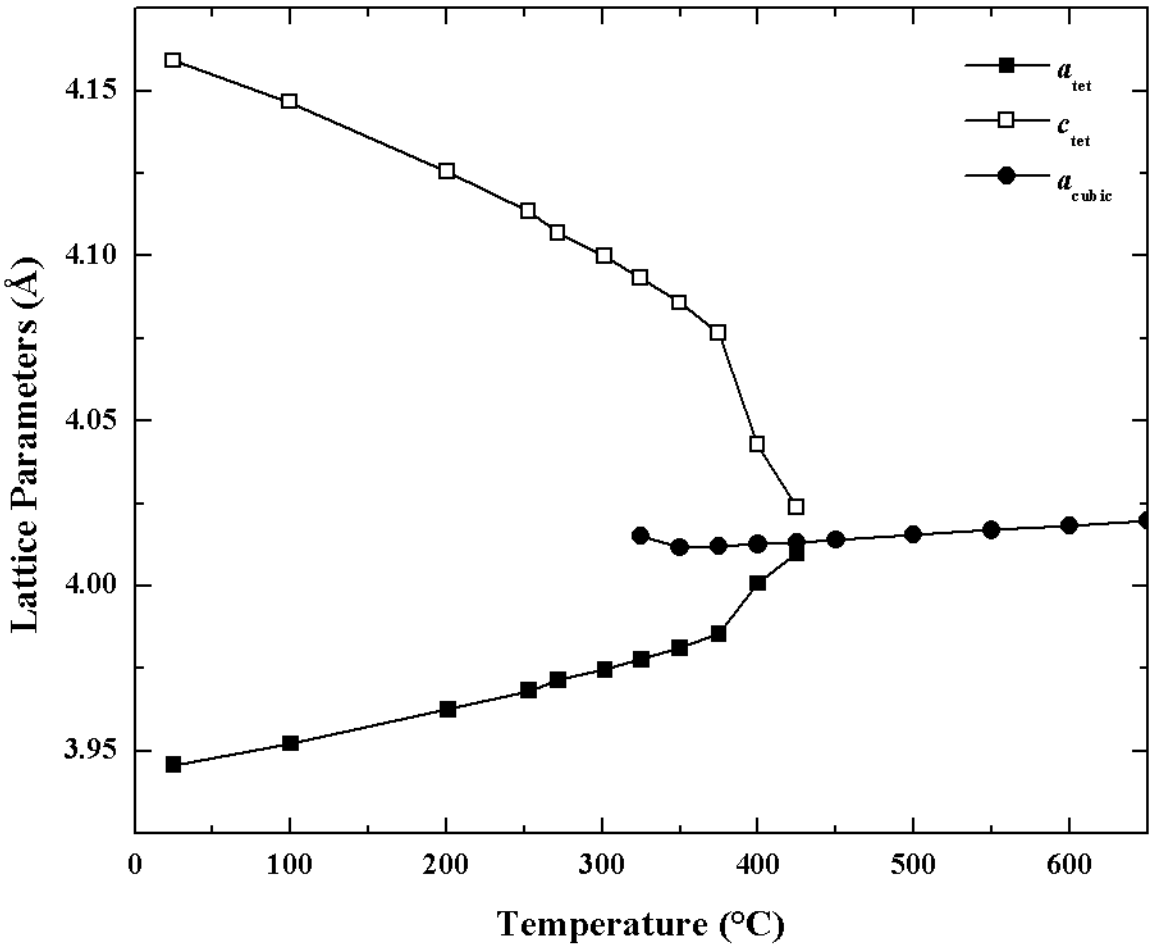

Figure 4.32: Lattice parameters as a function of temperature for the (0.8)[(0.75)PT-(0.25)BZT]-(0.2)BMZ composition.

4.3.3 High-temperature structural properties

To determine whether the compositions with multiple dielectric transitions in the PT-BZT-BMZ system also exhibit structural features similar to their PT-BZT-BMT counterparts, a high-temperature synchrotron study was performed on the (0.8)[(0.75)PT-(0.25)BZT]-(0.2)BMZ composition. This composition, whose dielectric response is shown in Figure 4.28, has dielectric peaks at 300°C, 350°C and 560°C. The diffraction data are shown in Figure 4.31. No peaks associated with phases other than perovskite

phases were observed at any temperature. The room-temperature tetragonal distortion, clearly illustrated by the splitting of the {200}, {210}, and {211} family of peaks, decreases with increasing temperature. At 325°C a second phase is observed in the pattern, with peaks in between the split tetragonal peaks. The relative fraction of this phase increases with temperature until the tetragonal phase is completely consumed at 425 - 450°C. Rietveld refinement reveals the tetragonal phase is best fit by a P4mm-type tetragonal structure while the high temperature phase is best fit by a Pm3m-type cubic perovskite structure. The best fits for the temperature range where both peaks are observed corresponded to a 2-phase model of the low and high temperature phases. Similar to the PT-BZT-BMT system, various combinations of perovskite symmetries were tested and none improved the goodness of fit relative to the 2-phase model. The lattice parameters derived from the Rietveld refinement analysis are plotted in Figure 4.32 and the structural parameters and reliability statistics from the models are listed in Tables 4.4 (tetragonal structure) and 4.5 (cubic structure).

Table 4.4: Refined structural and reliability parameters for the tetragonal phase of the (0.8)[(.75)PT-(0.25)BZT]-(0.2)BMZ composition at relevant temperatures using neutron data.

T	a_{tet}	c_{tet}	U_A^T	U_B^T	U_{O1}^T	U_{O2}^T	R_F^2	χ^2
°C	Å	Å	x100 Å^2	x100 Å^2	x100 Å^2	x100 Å^2		
25	3.9456	4.1589	0.03540	0.00398	0.02122	0.01148	0.1809	6.991
100	3.9522	4.1459	0.03760	0.00582	0.02705	0.02416	0.1508	4.006
200	3.9628	4.1243	0.04423	0.00717	0.01764	0.08983	0.1916	4.879
250	3.9685	4.1123	0.04763	0.00818	0.01464	0.03120	0.1805	4.428
275	3.9717	4.1058	0.04916	0.00844	0.01403	0.02871	0.1833	4.525
300	3.9746	4.0995	0.05425	0.00926	0.01791	0.03166	0.2073	4.504
325	3.9777	4.0931	0.04835	0.00371	0.02073	0.00499	0.2835	5.402
350	3.9813	4.0854	0.05334	0.01669	0.09045	0.03643	0.2358	4.908
375	3.9856	4.0764	0.04830	0.01373	0.10100	0.16113	0.2885	5.022
400	3.9995	4.0455	0.02376	0.01128	0.25997	0.02203	0.2488	2.967
425	4.0011	4.0427	0.02427	0.00611	0.80000	0.12244	0.2432	2.884

Table 4.5: Refined structural and reliability parameters for the cubic phase of the (0.8)[(.75)PT-(0.25)BZT]-(0.2)BMZ composition at relevant temperatures using neutron data.

T	A_{cubic}	U_A^C	U_B^C	U_O^C	R_F^2	χ^2
°C	Å	x100 Å^2	x100 Å^2	x100 Å^2		
325	4.0155	0.03018	0.04413	0.8000	0.2835	5.402
350	4.0114	0.07718	0.02204	0.06350	0.2358	4.908
375	4.0121	0.07951	0.02314	0.04879	0.2885	5.022
400	4.0126	0.07673	0.01781	0.04663	0.2488	2.967
425	4.0133	0.08086	0.02193	0.04141	0.2432	2.884
450	4.0140	0.07319	0.02184	0.05254	0.1499	4.544
500	4.0154	0.07479	0.02201	0.08855	0.2272	4.857
550	4.0168	0.07603	0.02267	0.08359	0.2226	4.508
600	4.0182	0.07934	0.02325	0.07344	0.2101	3.797
650	4.0199	0.08143	0.02420	0.06919	0.1958	3.299

The high-temperature structural data for (0.8)[75/25]-(0.2)BMZ is consistent with the synchrotron X-ray data collected from (0.75)[75/25]-(0.25)BMT and both clearly exhibit 2-phase coexistence. In the BMZ-containing sample the tetragonal phase is no longer observable almost a full 150°C below the high temperature dielectric transition, whereas the coexistence region in the BMT-containing sample persists to the high temperature transition.

4.3.4 PT-BZT-$BiScO_3$

In addition to the BMT and BMZ containing systems reported here, the substitution of $BiScO_3$ into PT-BZT has been investigated [Suchomel 2005]. Compared to BMT, the B-site in $BiScO_3$ is much larger on average (0.745Å v. 0.6625Å) and significantly less ferroelectrically-active (d^0_b = 0.11Å 0.165Å). BMZ has an average B-site cation radius that lies in between BMT and $BiScO_3$ (0.72Å) and B-site displacement similar to $BiScO_3$ (0.105Å v. 0.11Å for $BiScO_3$).

Compositions in the PT-BZT-$BiScO_3$ ternary system (Figure 4.33) were reported along the (1-*x*)[(0.8)PT-(0.2)BZT] - (*x*)$BiScO_3$ and (1-*x*)[(0.7)PT-(0.3)BZT] - (*x*)$BiScO_3$ pseudo-binary lines. The lattice parameters of the system are reproduced in Figure 4.34 and compared to the PT-$BiScO_3$ binary system. Similar to the BMT- and BMZ-containing systems, the MPB in PT-BZT-$BiScO_3$ shifts toward the tetragonal end-member with increasing BZT content.The dielectric data for (1-*x*)[(0.8)PT-(0.2)BZT] - (*x*)$BiScO_3$ is reproduced in Figure 4.35. No "extra" dielectric transitions are observed in any of the (1-*x*)[(0.8)PT-(0.2)BZT] - (*x*)$BiScO_3$ compositions. However, the raw data was obtained for the *x* = 0.2 and 0.26 samples in the (1-*x*)[(0.7)PT-(0.3)BZT] - (*x*)$BiScO_3$ system and multiple dielectric transitions can be observed (Figure 4.36) with the high temperature transitions occurring near 600°C [data from Suchomel 2008].

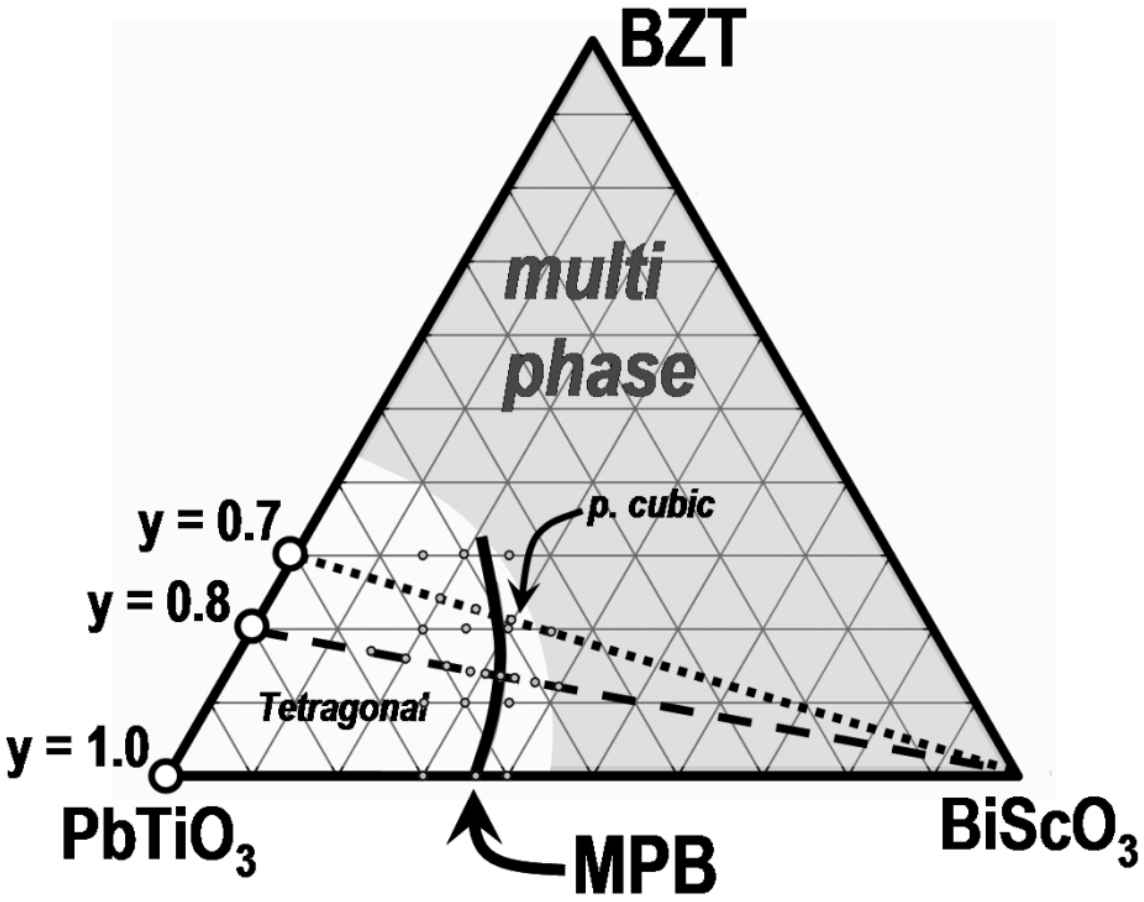

Figure 4.33: Schematic of the BZT – PT - $BiScO_3$ ternary phase diagram. Labels mark the multi-phase, pseudo-cubic perovskite, and tetragonal perovskite phase fields. Data points indicate experimentally explored compositions. The solid black line marks the location of the MPB in the system. Reproduced from [Suchomel 2005].

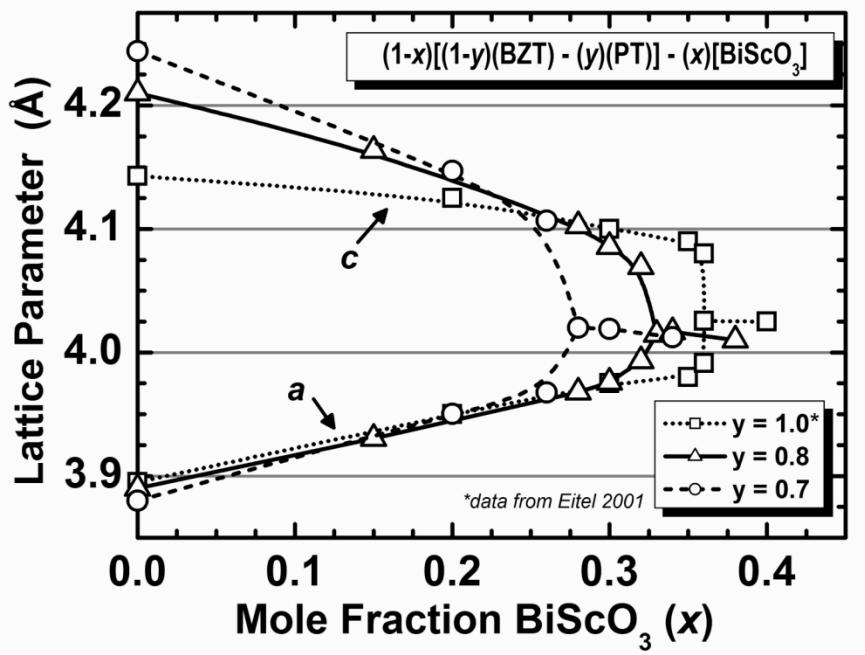

Figure 4.34: Lattice parameters plotted as a function of $BiScO_3$ content (x) for select (y) binary compositional lines in the (1–x)[(1–y)BZT - (y)PT] - (x)$BiScO_3$ pseudo-ternary solid solution. Reproduced from [Suchomel 2005].

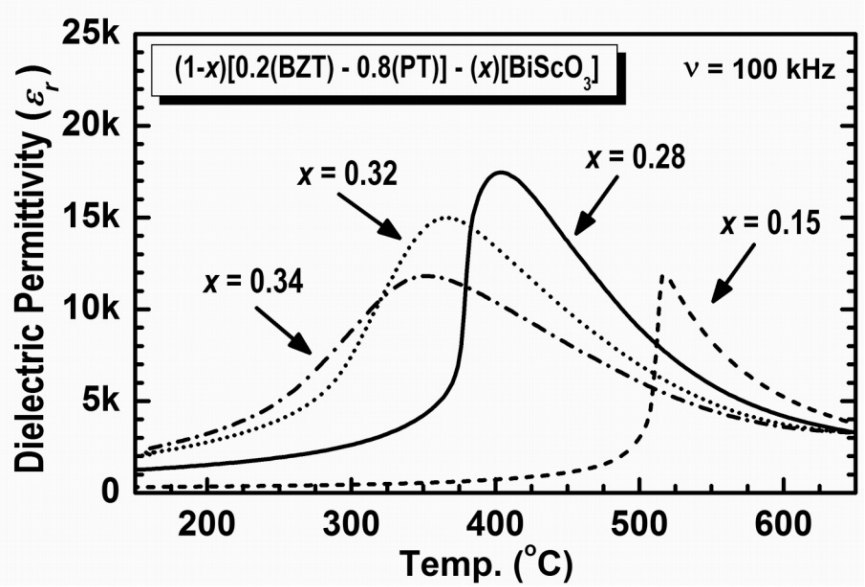

Figure 4.35: Dielectric permittivity plotted as a function of temperature for select compositions along the (y) = 0.80 compositional line in the (1-x)[(1-y)BZT - (y)PT] - (x)$BiScO_3$ pseudo-ternary solid solution. The MPB along this compositional line is (x) ≈ 0.33. Reproduced from [Suchomel 2005].

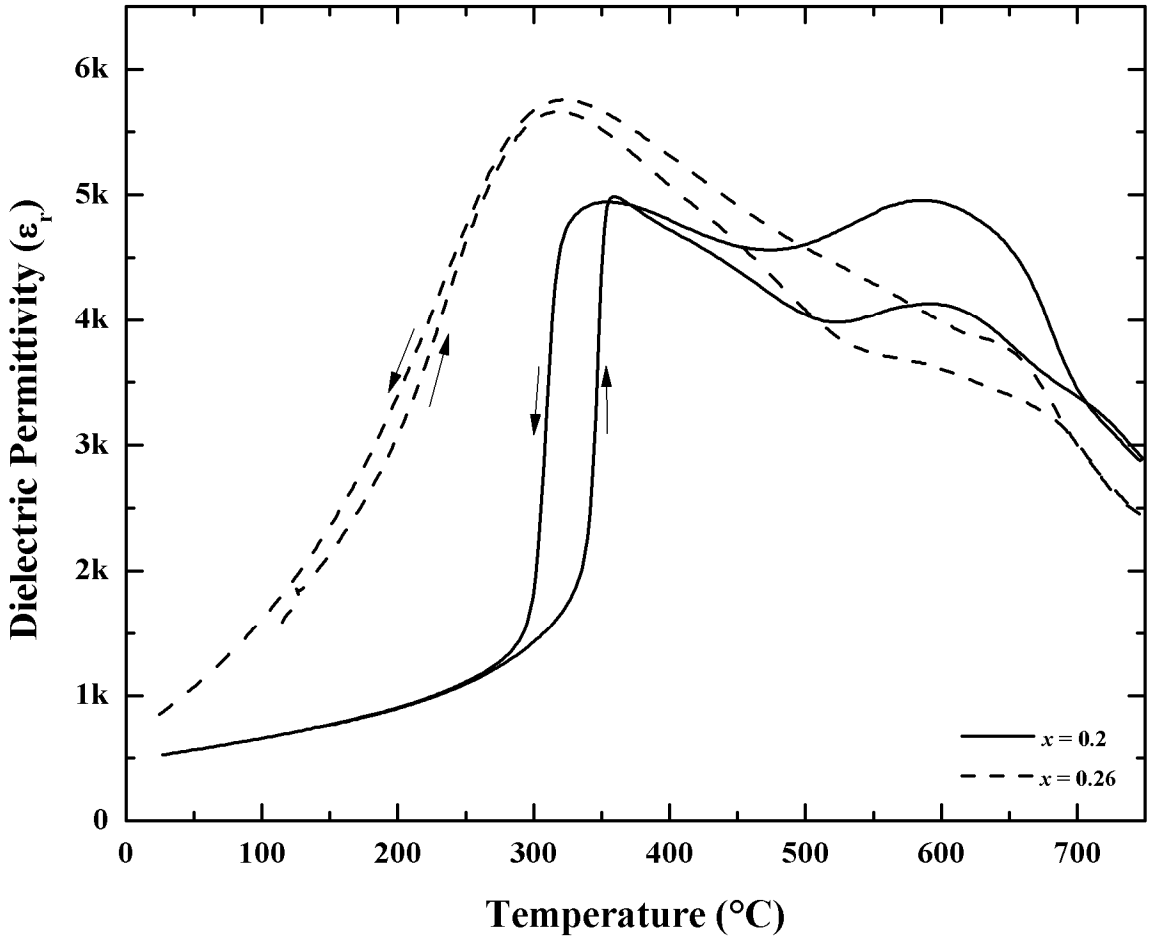

Figure 4.36: Dielectric permittivity plotted as a function of temperature for compositions exhibiting multiple dielectric transitions in the (1-*x*)[(0.7)PT - (0.3)BZT] - (*x*)$BiScO_3$ pseudo-binary solid solution. Arrows indicate direction of thermal ramp.

4.4 $BiFeO_3$-containing systems

4.4.1 Motivation

In the previous sections, the enhanced tetragonality additive BZT was shown to induce multiple dielectric transitions in the high T_C PT-BMT, BT-BMZ, and PT-$BiScO_3$ systems. For PT-BZT-BMT, the highest-temperature dielectric transition was shown to correspond to the transition of a ferroelectric tetragonal phase to a paraelectric cubic phase. Thus, MPB compositions in this system exhibit the highest reported T_Cs in a PT-based system, approximately 150°C higher than the next highest system (PT-$BiScO_3$). As demonstrated in chapter 2, BZT is not the only substituent capable of inducing enhanced tetragonality in PT. To investigate whether other enhanced tetragonality additives also induce multiple dielectric transitions, ternary systems containing $BiFeO_3$ were investigated.

$BiFeO_3$ (BF) is fully soluble in $PbTiO_3$, with an MPB near 70% BF [Fedulov 1961]. Like BZT, the substitution of BF into PT enhances the tetragonality of the former. The tetragonal phase in PT-$BiFeO_3$ reaches a *c/a* ratio of ~1.18 at the MPB and a T_C of approximately 632°C, compared to the *c/a* ratio of 1.11 and T_C of 700°C at the solubility limit in PT-BZT [Sunder 1995]. However, the high losses in these systems make them unsuitable for applications. The wide solubility range and strong enhancement of *c/a* makes $BiFeO_3$ ideally suited for further exploring in ternary Pb/Bi systems.

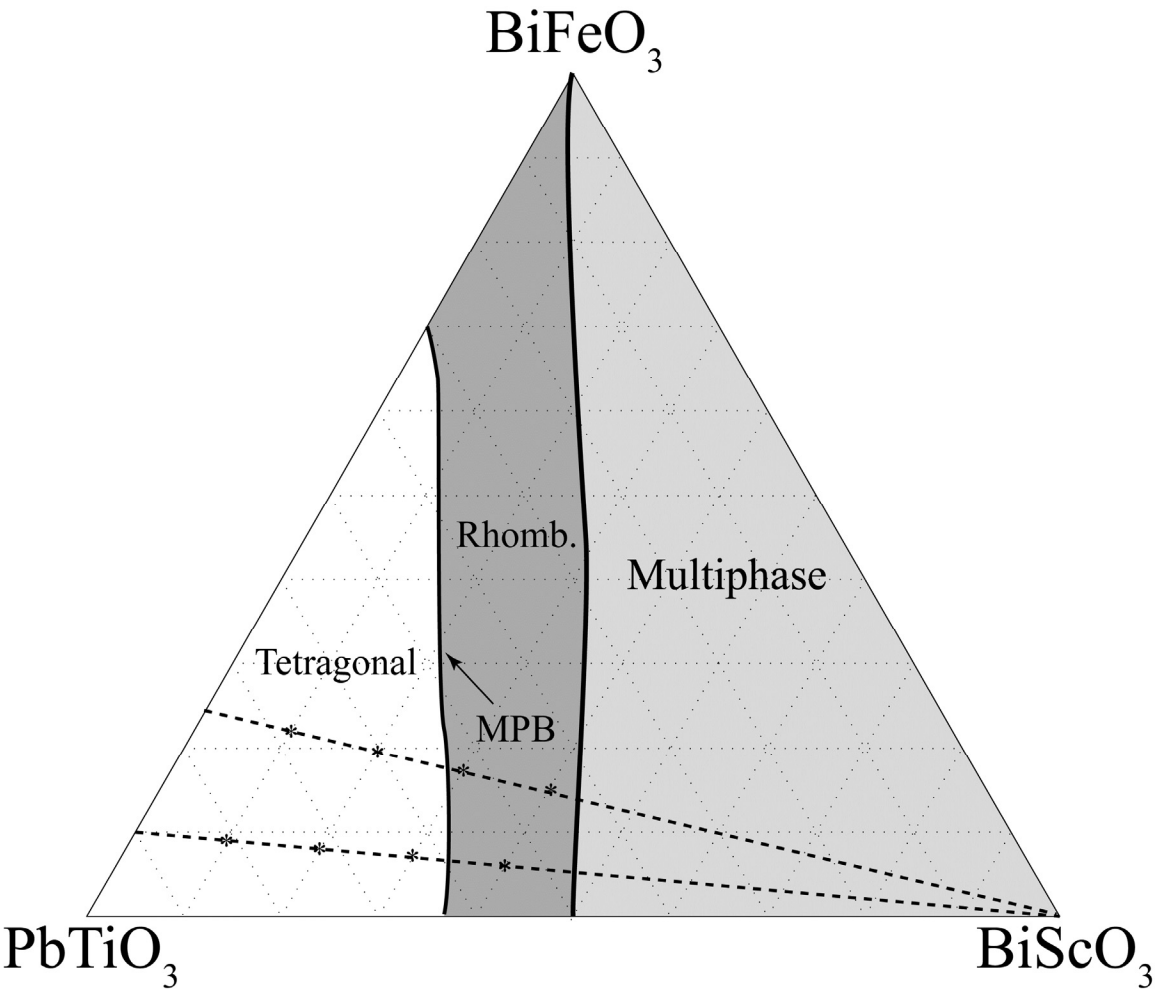

Figure 4.37: PT-BF-$BiScO_3$ ternary diagram. Synthesized compositions and MPB are marked.

4.4.2 Room temperature structural properties

Compositions in the PT-BF-$BiScO_3$ system were synthesized along the (1-*x*)[(0.9)PT – (0.1)BF]-(*x*)$BiScO_3$ and (1-*x*)[(0.75)PT – (0.25)BF]-(*x*)$BiScO_3$ lines (Figure 4.37). The PT-BF-BMT system was also investigated along the (1-*x*)[(0.75)PT - (0.25)BF]-(*x*)BMT line (Figure 4.38). The enhanced tetragonality end-members, (0.9)PT – (0.1)BF and (0.75)PT – (0.25)BF, have *c/a* = 1.066 and 1.087 and T_C = 485°C and

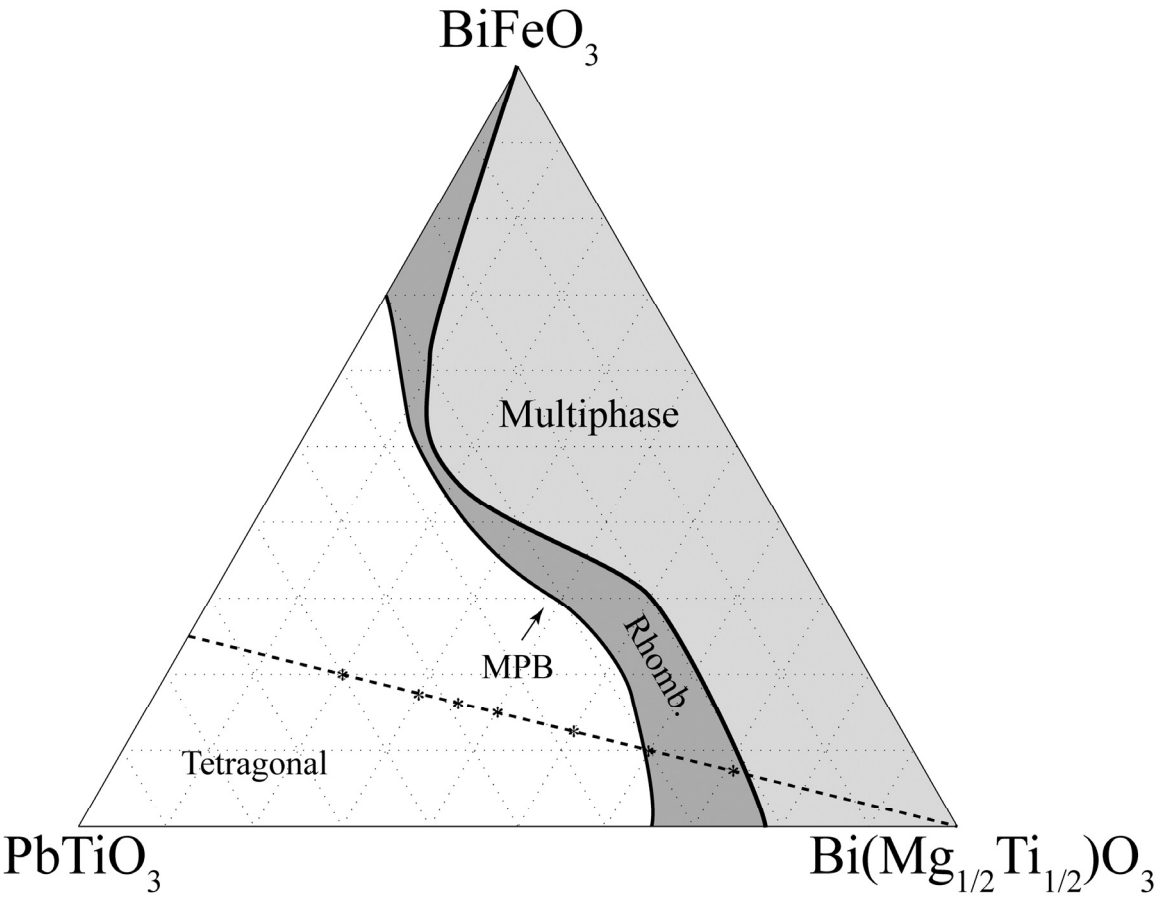

Figure 4.38: PT-BF-$BiScO_3$ ternary diagram. Synthesized compositions and MPB are marked.

500°C, respectively. The room-temperature diffraction data for the two ternary systems is plotted in Figure 4.39 ((1-*x*)[(0.9)PT – (0.1)BF]-(*x*)$BiScO_3$), Figure 4.40 ((1-*x*)[(0.75)PT – (0.25)BF]-(*x*)$BiScO_3$), and Figure 4.41 ((1-*x*)[(0.75)PT – (0.25)BF]-(*x*)BMT). (1-*x*)[(0.9)PT – (0.1)BF]-(*x*)$BiScO_3$ is single-phase for all investigated compositions ($x \leq 0.4$). The peak splitting indicates that the structure remains tetragonal through $x = 0.3$ and peak broadening in $x = 0.4$ suggests that composition lies close to the MPB.

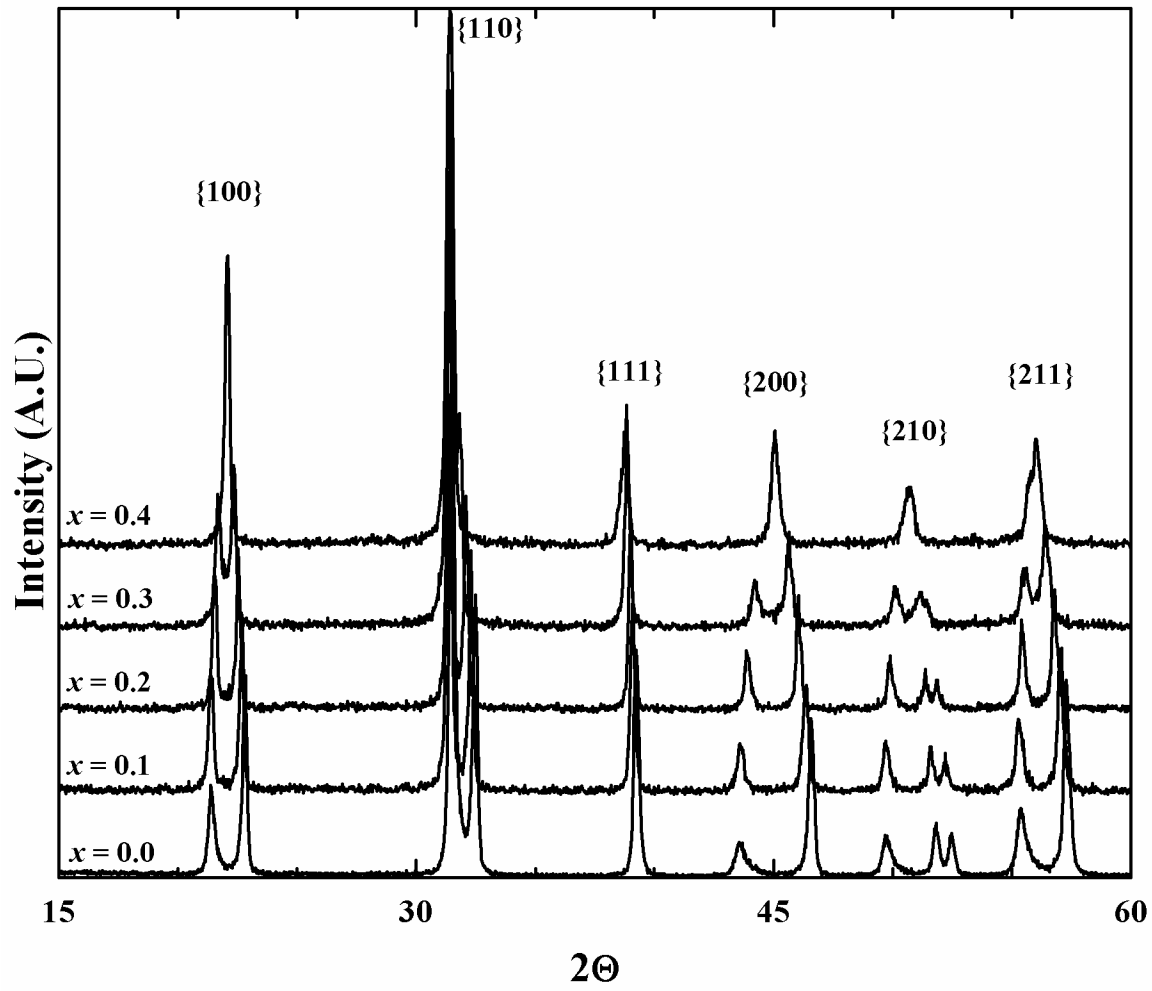

Figure 4.39: XRD patterns of compositions in the (1-*x*)[(0.9)PT – (0.1)BF] – (*x*)$BiScO_3$ solid solution. Families of perovskite peaks are labeled.

(1-*x*)[(0.75)PT – (0.25)BF]-(*x*)$BiScO_3$ is only single-phase through $x = 0.3$ and impurity peaks are detected in the $x = 0.4$ composition. A tetragonal phase is only stable to a point between $x = 0.2$ - 0.3; the $x = 0.3$ composition exhibits no resolvable splitting and the peak broadening suggests it also lies close to the MPB.

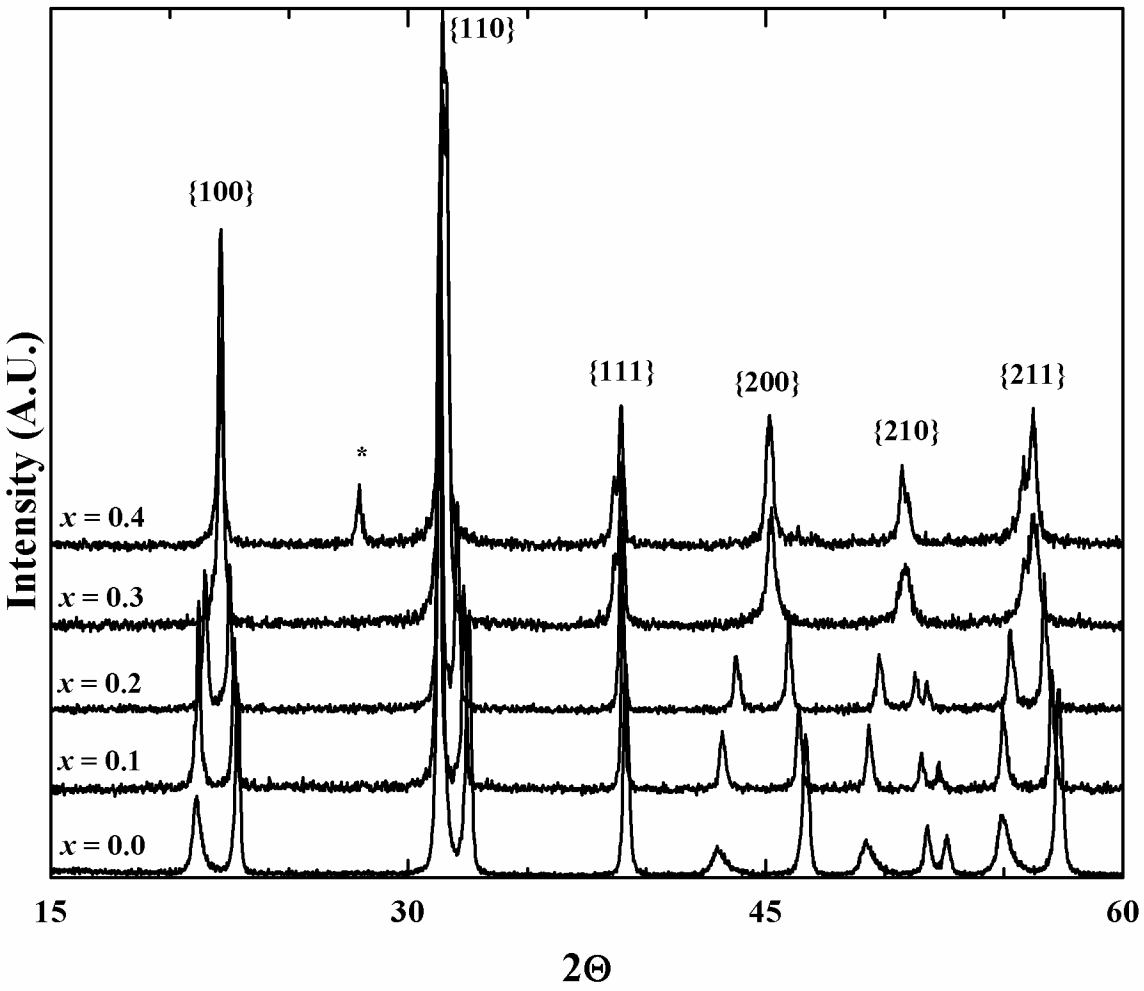

Figure 4.40: XRD patterns of compositions in the (1-*x*)[(0.75)PT – (0.25)BF] – (*x*)$BiScO_3$ solid solution. Families of perovskite peaks are labeled. Impurity phase peaks are marked with a "*".

The substitution of BMT into (1-*x*)[(0.75)PT – (0.25)BF] yields a much larger single-phase region, consistent with the larger solubility range of BMT in PT compared to $BiScO_3$. Samples are impurity free up to a BMT concentration of 70%. The MPB in (1-*x*)[(0.75)PT – (0.25)BF] – (*x*)BMT is located at approximately $x = 0.6$. The width of the {200} peak in $x = 0.7$ composition (0.323°) is approximately half that of the

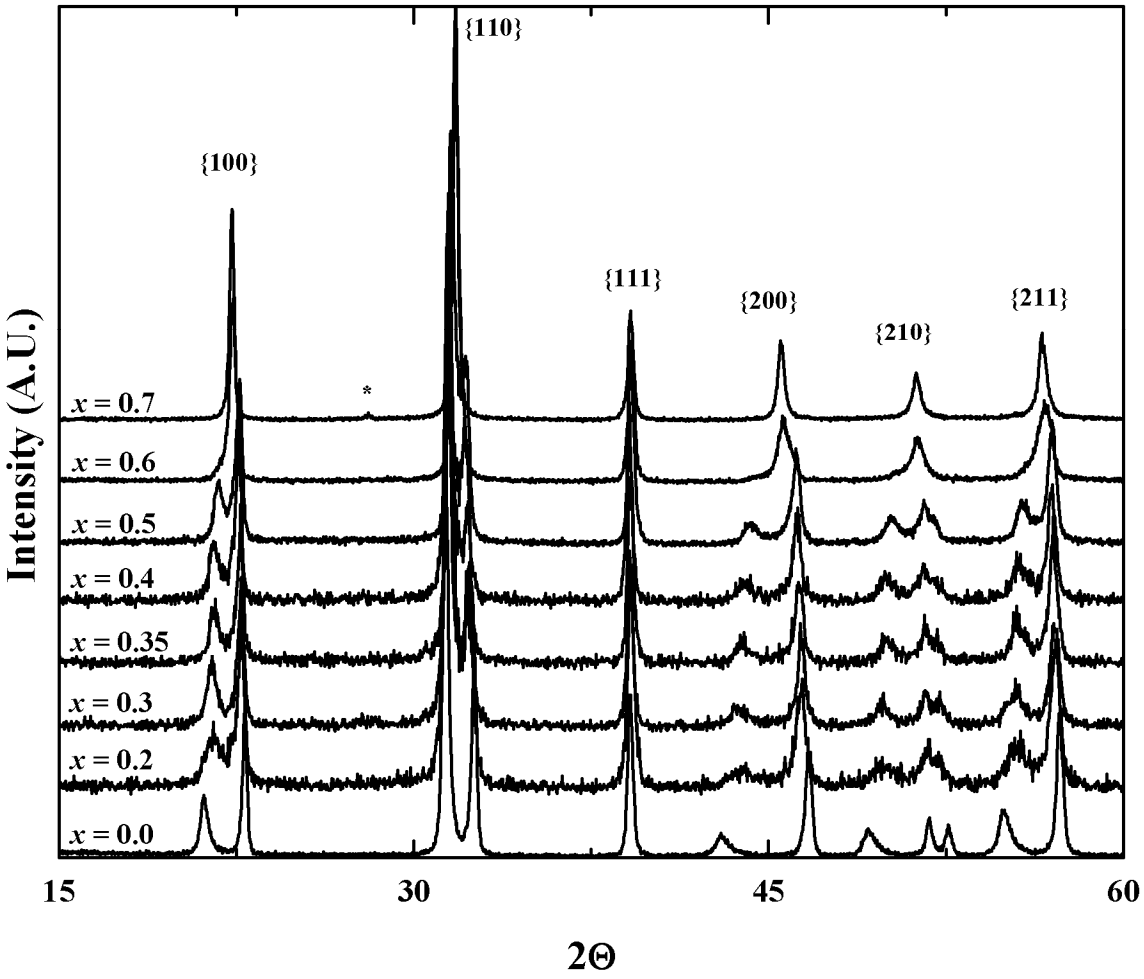

Figure 4.41: XRD patterns of compositions in the (1-*x*)[(0.75)PT – (0.25)BF] – (*x*)BMT solid solution. Families of perovskite peaks are labeled. Impurity phase peaks are marked with a "*".

x = 0.6 composition (0.655°). Figure 4.42 and 4.43 show the lattice parameters for the ternary $BiScO_3$-containing and BMT-containing PT-BF lines, respectively, and their respective binary end-members. Similar to the BZT-containing ternary systems, the location of the MPB shifts toward the binary end-member as the concentration of the tetragonality-enhancing additive (BF) is increased.

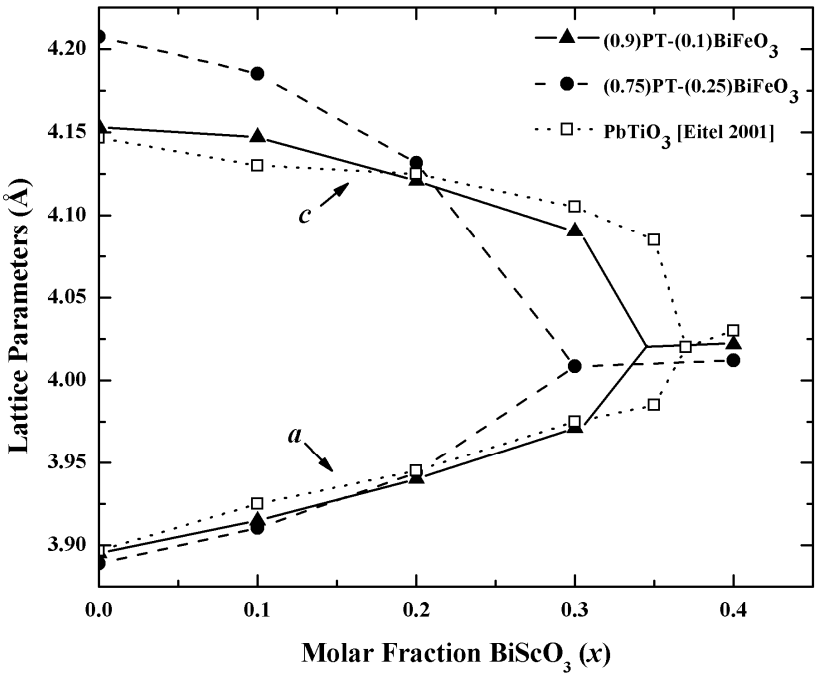

Figure 4.42: Lattice parameters as a function of $BiScO_3$ substitution for the (1-*x*)[(0.75)PT-(0.25)BF]-(*x*)$BiScO_3$ and (1-*x*)[(0.9)PT-(0.1)BF]-(*x*)$BiScO_3$ solid solutions. MPB location is estimated in (1-*x*)[(0.9)PT-(0.1)BF]-(*x*)$BiScO_3$ line.

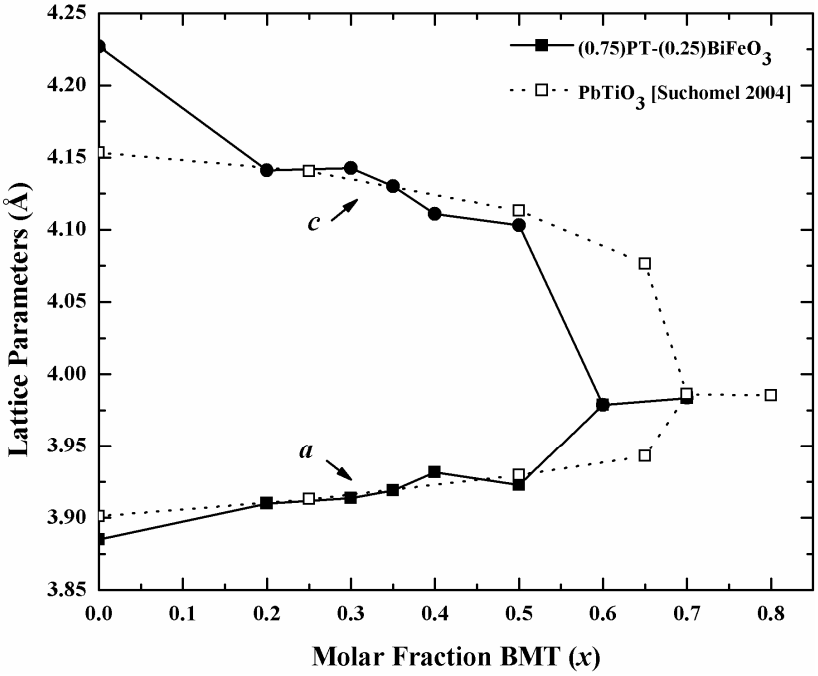

Figure 4.43: Lattice parameters as a function of BMT substitution for the (1-*x*)[(0.75)PT-(0.25)BF]-(*x*)BMT solid solution.

4.4.3 Dielectric properties

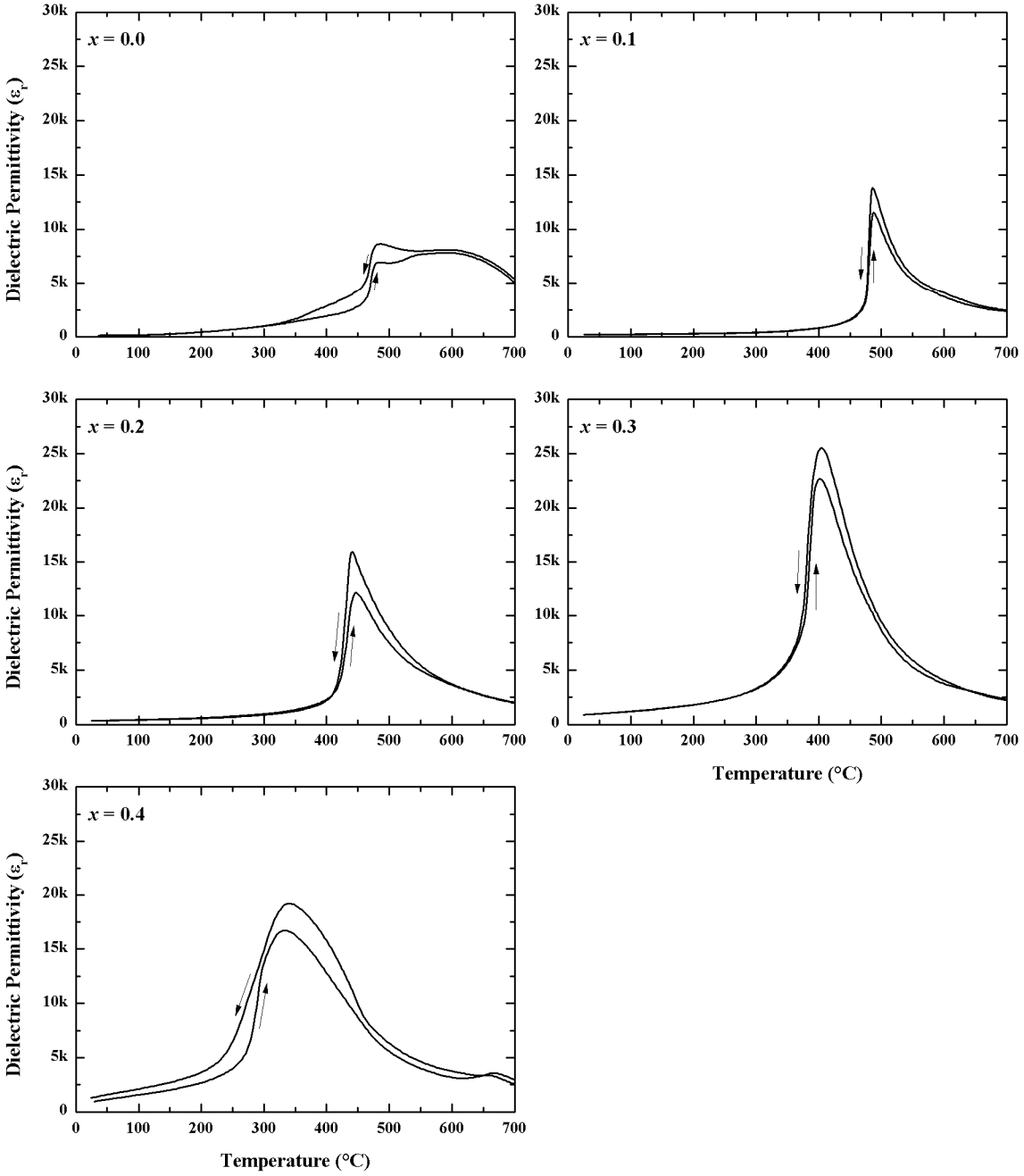

Figure 4.44: Dielectric response as a function of temperature for compositions in the (1-*x*)[(0.9)PT-(0.1)BF]-(*x*)$BiScO_3$ solid solution (*f* = 100kHz). Arrows indicate direction of thermal ramp.

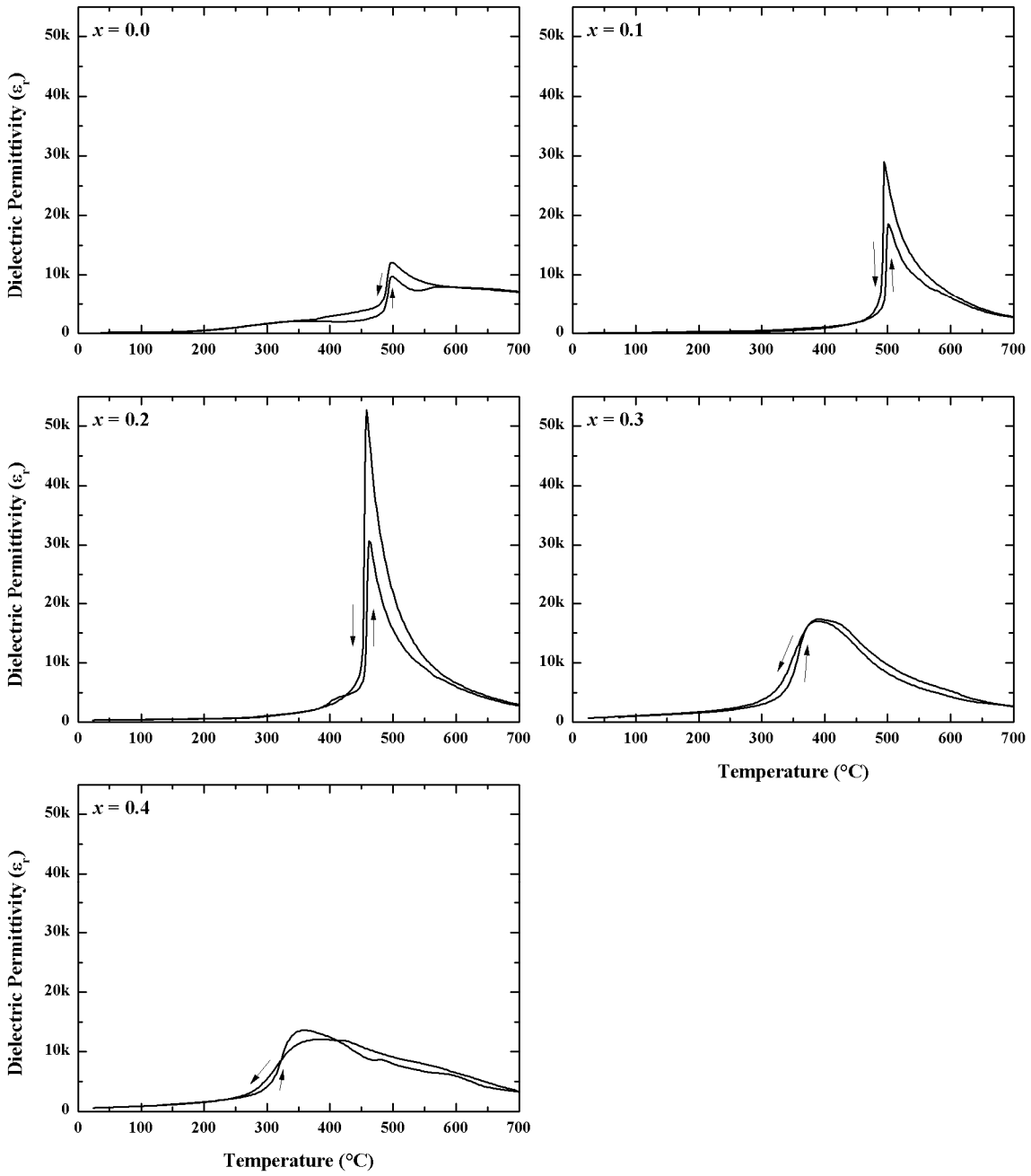

Figure 4.45: Dielectric response as a function of temperature for compositions in the (1-*x*)[(0.75)PT-(0.25)$BiFeO_3$]-(*x*)$BiScO_3$ solid solution (*f* = 100kHz). Arrows indicate direction of thermal ramp.

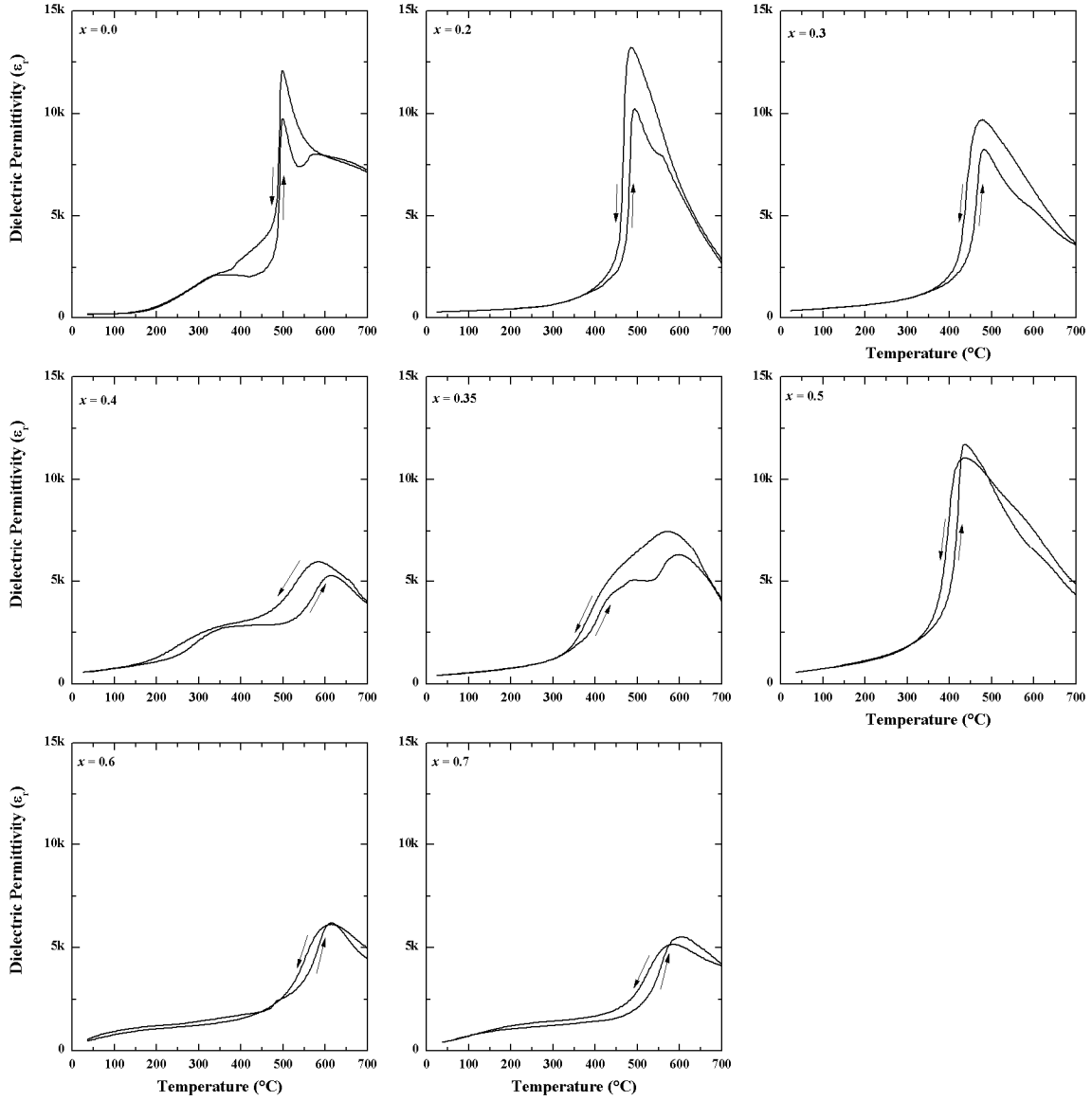

Figure 4.46: Dielectric response as a function of temperature for selected compositions in the (1-*x*)[(0.75)PT-(0.25)BF]-(*x*)BMT solid solution (*f* = 100kHz). Arrows indicate direction of thermal ramp.

The dielectric data for (1-*x*)[(0.9)PT – (0.1)BF]-(*x*)$BiScO_3$, (1-*x*)[(0.75)PT – (0.25)BF]-(*x*)$BiScO_3$, and (1-*x*)[(0.75)PT – (0.25)BF]-(*x*)BMT are shown in Figures 4.44, 4.45, and 4.46, respectively.

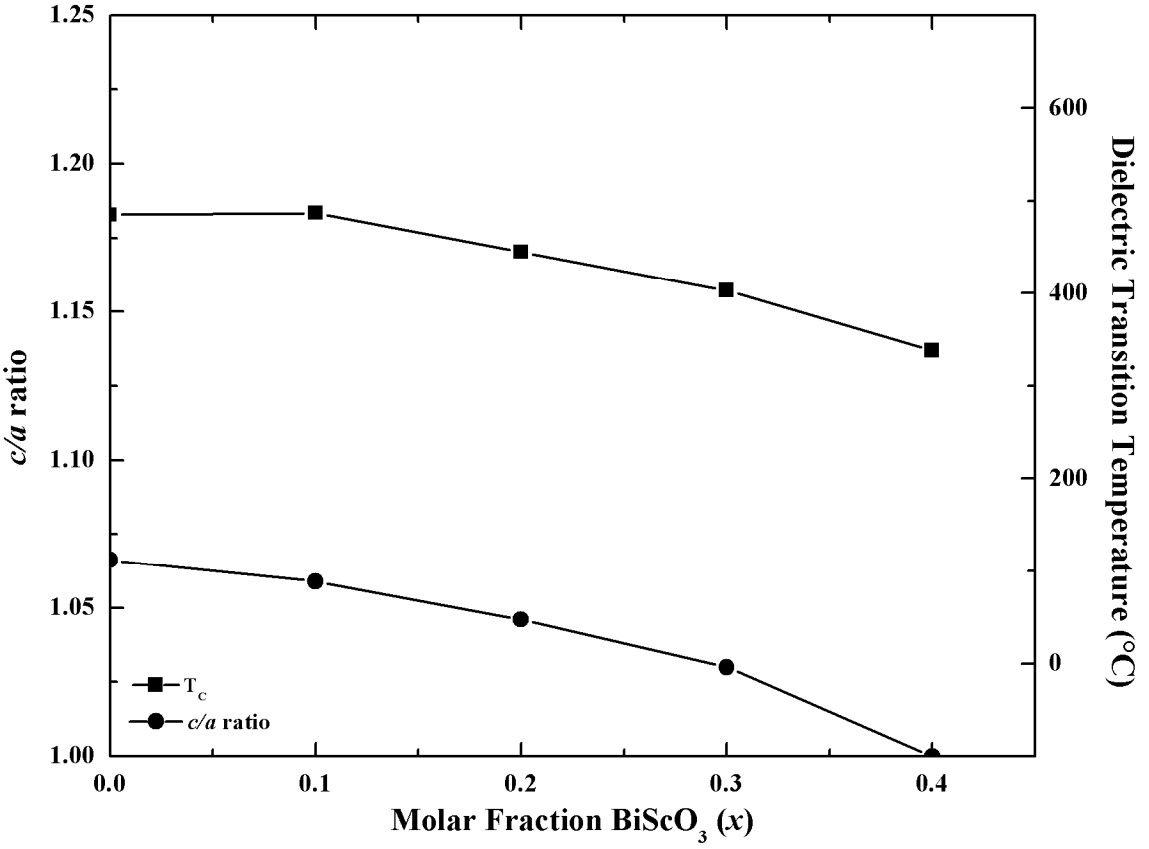

Figure 4.47: *c/a* ratio and dielectric transition temperatures as a function of composition in the (1-*x*)[(0.9)PT – (0.1)BF]-(*x*)$BiScO_3$ solid solution.

The permittivity of the $BiScO_3$-containing systems increase for low substitutions of $BiScO_3$ ($x \leq 0.2$) then decrease with further substitution as the permittivity maximum broadens. In all the $BiScO_3$-containing compositions, only the $x = 0.4$ composition in the (1-*x*)[(0.9)PT – (0.1)BF]-(*x*)$BiScO_3$ line shows any indication of a second dielectric maximum. However, the dielectric losses at those temperatures are high and it is unlikely the peak, which is at a higher temperature than observed in other ternary systems, is associated with a real transition. Similarly, large broad dielectric features are also

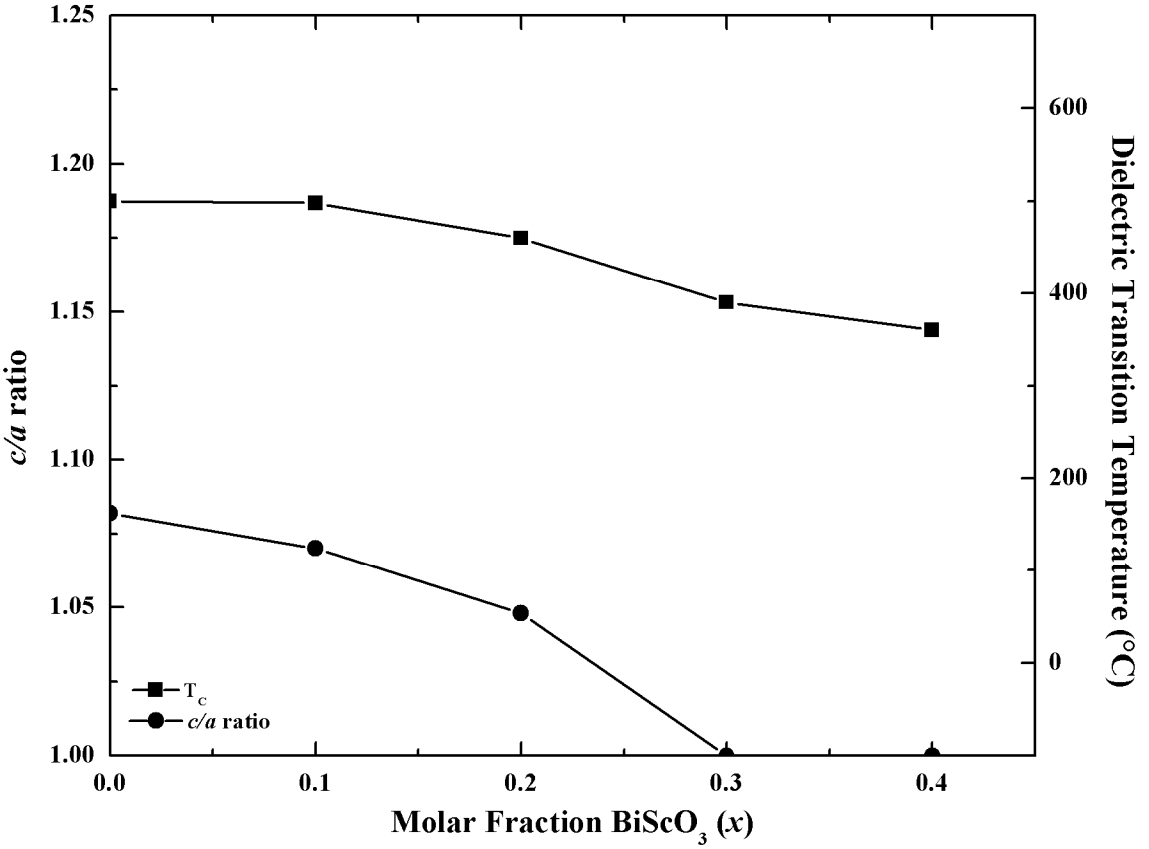

Figure 4.48: *c/a* ratio and dielectric transition temperatures as a function of composition in the (1-*x*)[(0.75)PT – (0.25)BF]-(*x*)$BiScO_3$ solid solution.

observed above 500°C in the $x = 0.0$ compositions in all three solid solutions. These high-temperature dielectric permittivities are unlikely to be reliable.

In contrast to the $BiScO_3$-containing systems, the (1-*x*)[(0.75)PT – (0.25)BF]-(*x*)BMT line exhibits clear evidence for multiple dielectric transitions, with almost every composition exhibiting a second high-temperature dielectric transition near 600°C. The dependence of the transitions in the BMT-containing system is more erratic than the BZT-containing systems reported earlier.

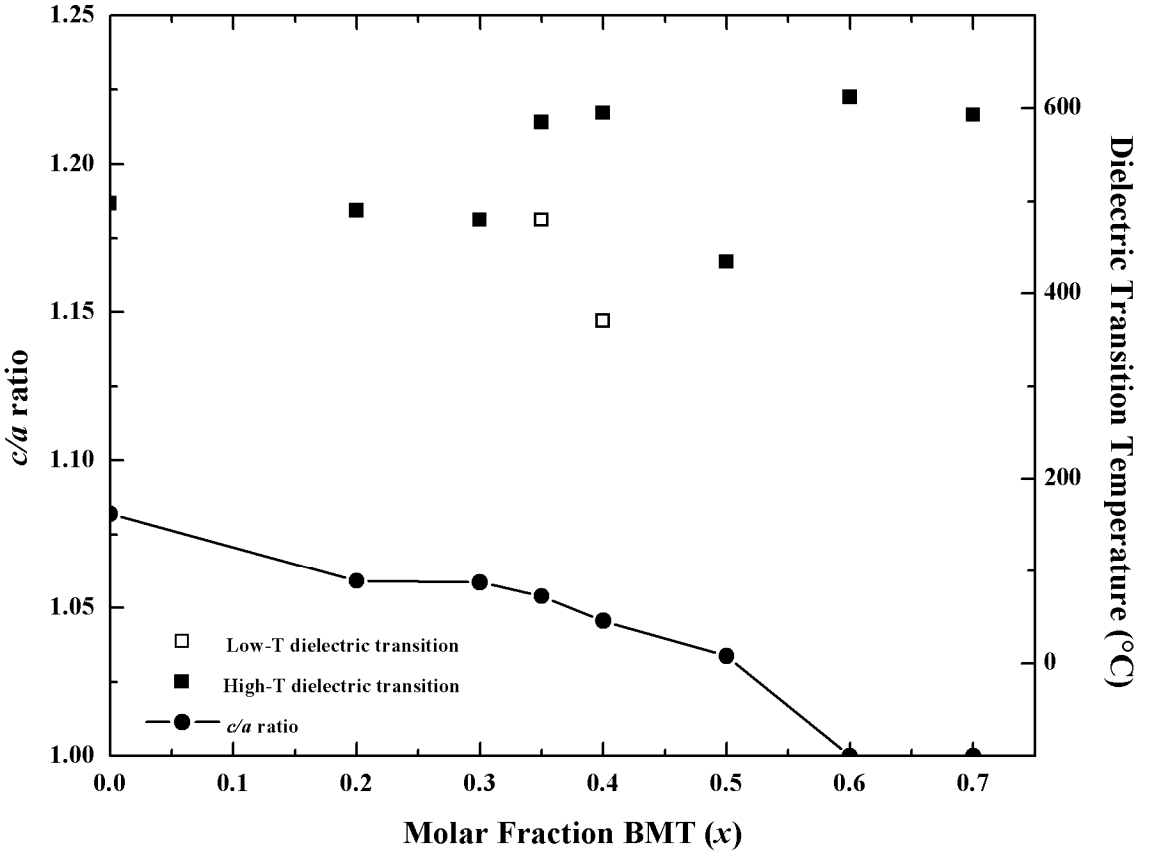

Figure 4.49: *c/a* ratio and dielectric transition temperatures as a function of composition in the (1-*x*)[(0.75)PT – (0.25)BF]-(*x*)BMT solid solution.

This variation is more clearly revealed in Figures 4.47, 4.48, and 4.49 which show the compositional dependence of the dielectric transition temperatures and *c/a* ratio of the (1-*x*)[(0.9)PT – (0.1)BF]-(*x*)$BiScO_3$, (1-*x*)[(0.75)PT – (0.25)BF]-(*x*)$BiScO_3$, and (1-*x*)[(0.75)PT – (0.25)BF]-(*x*)BMT pseudo-binaries. It should be noted the high-temperature transition (600°C) at the MPB in (1-*x*)[(0.75)PT – (0.25)BF]-(*x*)BMT (*x* = 0.6) is comparable to that of PT-BZT-BMT and significantly higher than those previously reported for PT-BS or PZT.

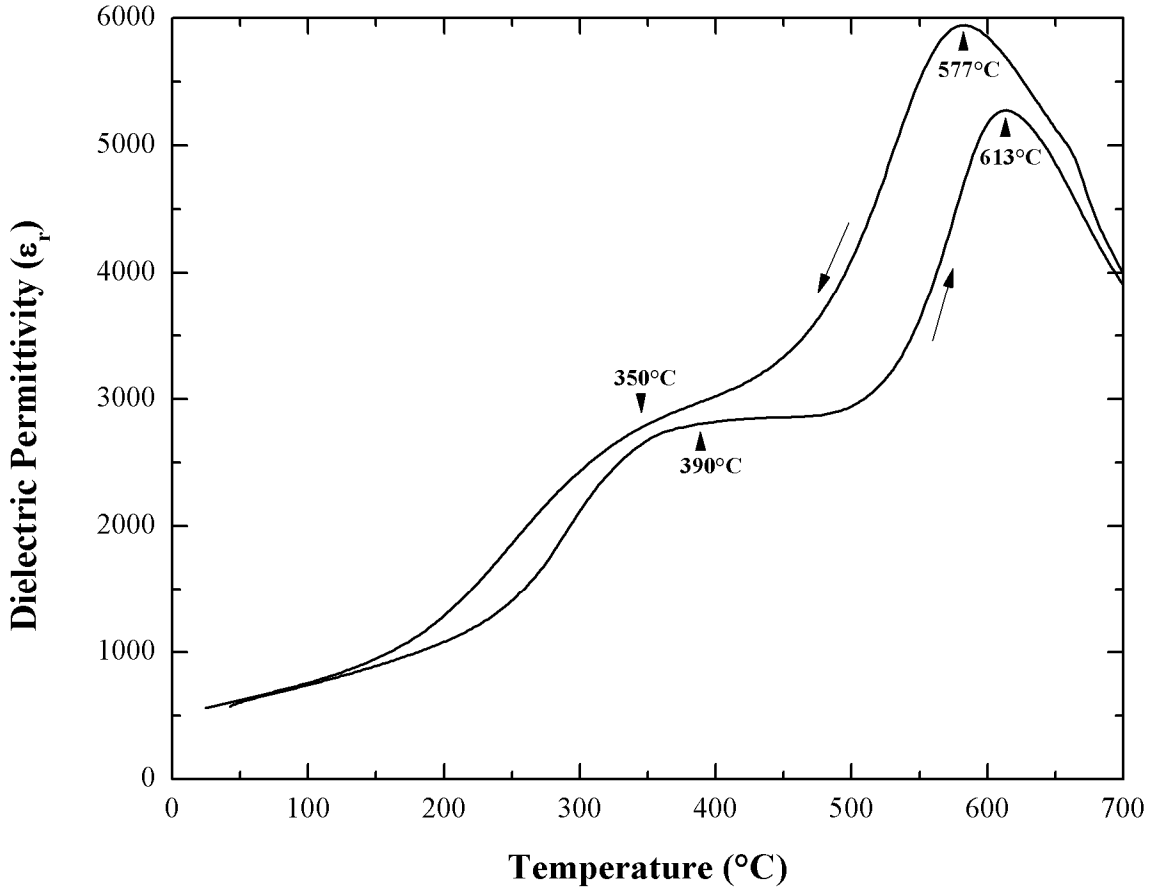

Figure 4.50: Dielectric permittivity as a function of temperature for the (0.6)[(0.75)PT – (0.25)BF] – (0.4)BMT composition. Arrows indicate thermal ramp and dielectric transition temperatures are labeled.

4.4.4 High-temperature structural properties

To determine if the structural behavior in the PT-BF-BMT compositions that exhibit multiple dielectric transitions is similar to those in the BZT-containing systems, a variable-temperature synchrotron XRD study was performed on the $x = 0.4$ composition in the (1-x)[(0.75)PT – (0.25)BF] – (x)BMT solid solution. The dielectric permittivity of that sample is shown in Figure 4.50.

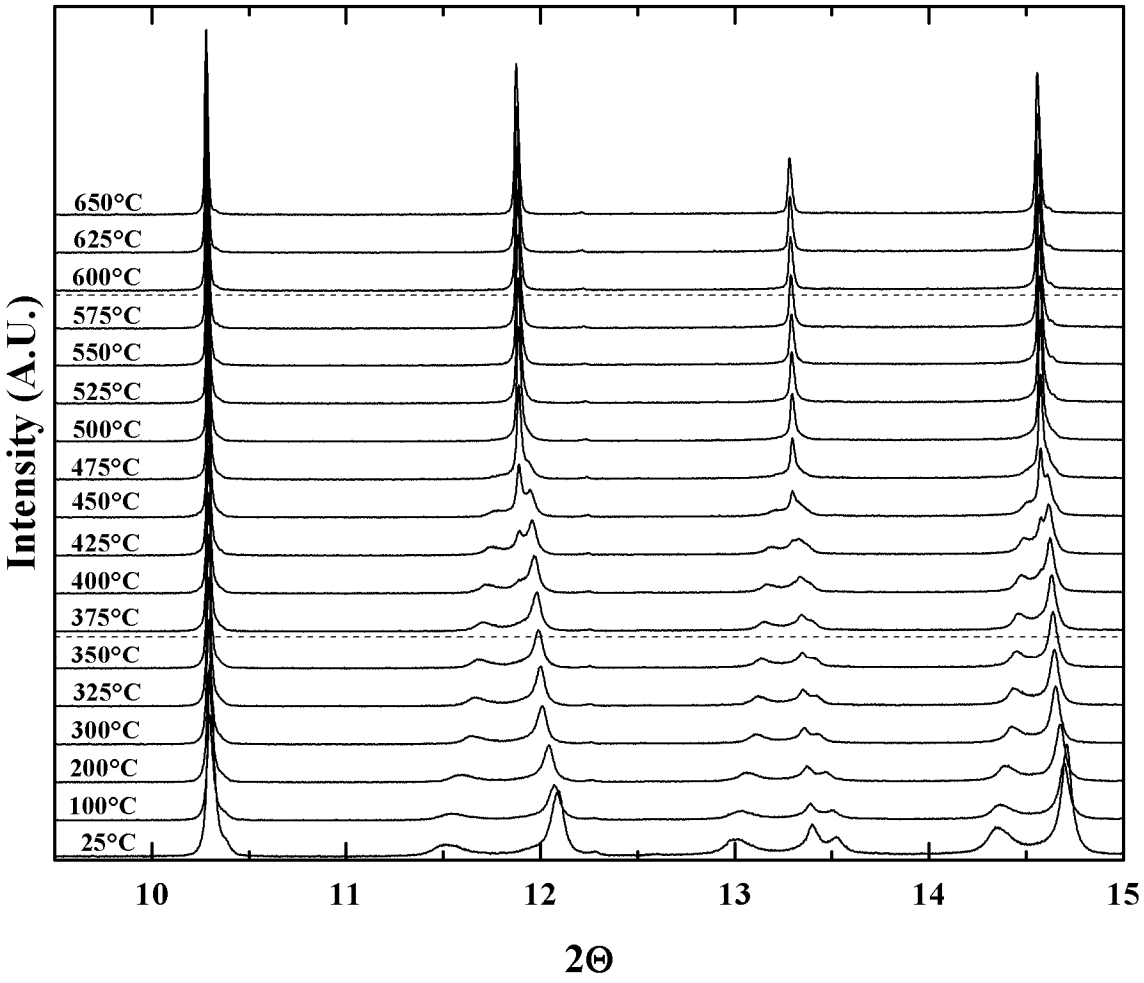

Figure 4.51: Synchrotron powder diffraction patterns for the (0.6)[(0.75)PT – (0.25)BF] - (0.4)BMT composition for temperatures between 25°C and 650°C. The positions of the dielectric transition in this composition are represented by the horizontal dashed lines.

This composition has dielectric maxima at 370°C and 590°C. The raw diffraction data are shown as a function of temperature in Figure 4.51. All patterns are free of any impurity phases. Consistent with the data for the (0.75)[75/25] – (0.25)BMT and (0.8)[75/25] – (0.2)BMZ compositions, at the first transition the single phase tetragonal structure transforms into a 2-phase assembly of the lower temperature tetragonal form and the high-temperature cubic form.

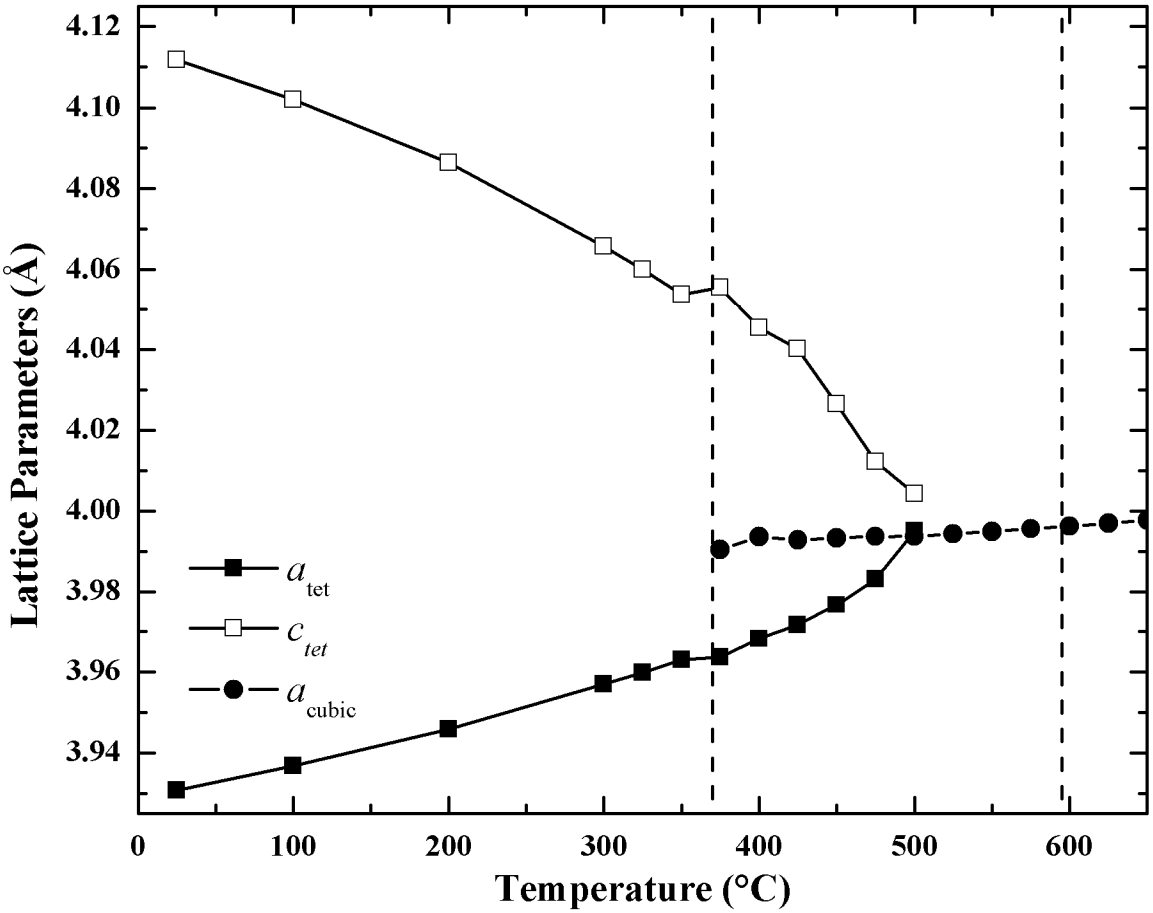

Figure 4.52: Lattice parameters as a function of temperature for the (0.6)[(0.75)PT-(0.25)$BiFeO_3$]-(0.4)BMT composition. Dashed vertical lines represent location of dielectric maxima for this composition.

Like the BMZ-containing composition, the tetragonal phase is no longer resolvable in the diffraction pattern at temperatures ~75°C below the second dielectric maximum. Rietveld refinement revealed the tetragonal and cubic phases were well-fit by the P4mm and Pm3m space groups. Once again, the diffraction patterns modeled with a 2-phase region were checked against other perovskite symmetries and the multi-phase model yielded the best statistical fit. The lattice parameters derived from the Rietveld refinement are plotted in Figure 4.52 and the structural parameters and reliability statistics are listed in Tables 4.6 (tetragonal) and 4.7 (cubic).

Table 4.6: Refined structural and reliability parameters for the tetragonal phase of the (0.6)[(.75)PT-(0.25)BF]-(0.4)BMT composition.

T	a_{tet}	c_{tet}	U_A^T	U_B^T	U_{O1}^T	U_{O2}^T	R_F^2	χ^2
°C	Å	Å	x100 Å^2	x100 Å^2	x100 Å^2	x100 Å^2		
25	3.9301	4.1135	0.03250	0.00767	0.11713	0.01538	0.1369	8.613
100	3.9346	4.1019	0.03459	0.00725	0.08946	0.00864	0.1322	5.025
200	3.9452	4.0877	0.03751	0.00709	0.14460	0.01067	0.1323	4.847
300	3.9565	4.0666	0.04318	0.00781	0.15185	0.00432	0.1467	4.861
325	3.9596	4.0606	0.04491	0.00911	0.15959	0.00395	0.1507	4.930
350	3.9630	4.0537	0.04643	0.00891	0.16369	0.00343	0.1585	4.873
375	3.9638	4.0538	0.04270	0.01463	0.08351	0.00233	0.2097	3.241
400	3.9671	4.0475	0.04557	0.01822	0.16253	0.00261	0.1950	3.029
425	3.9755	4.0294	0.04832	0.01003	0.36147	0.00253	0.1573	4.345
450	3.9784	4.0212	0.05160	0.00156	0.42597	0.02410	0.2093	3.394
475	3.9833	4.0079	0.04469	0.02500	0.43533	0.02510	0.2698	4.637
500	3.9849	4.0057	0.03210	0.01940	0.80000	0.04048	0.2581	5.151

Table 4.7: Refined structural and reliability parameters for the cubic phase of the (0.6)[(.75)PT-(0.25)BF]-(0.4)BMT.

T	A_{cubic}	U_A^C	U_B^C	U_O^C	R_F^2	χ^2
°C	Å	x100 Å^2	x100 Å^2	x100 Å^2		
375	3.9905	0.06502	0.01861	0.57721	0.2097	3.241
400	3.9909	0.06354	0.02802	0.17650	0.1950	3.029
425	3.9919	0.06655	0.00500	0.27995	0.1573	4.345
450	3.9938	0.09265	0.05139	0.00684	0.2093	3.394
475	3.9939	0.08693	0.03488	0.02774	0.2698	4.637
500	3.9941	0.06213	0.01577	0.04742	0.2581	5.151
525	3.9943	0.08043	0.02624	0.04101	0.1287	3.281
550	3.9950	0.07294	0.02035	0.05418	0.2001	3.873
575	3.9957	0.07289	0.02105	0.05878	0.1300	3.789
600	3.9964	0.07390	0.02071	0.05860	0.1822	3.498
625	3.9971	0.07564	0.02030	0.05471	0.1295	3.692
650	3.9978	0.07727	0.02112	0.05526	0.1257	3.622

High-temperature diffraction studies have been performed on four different compositions, representing three different ternary systems, which are tetragonal at room-temperature yet have exhibited multiple dielectric transitions. In each composition, the structures have exhibited "two-phase" features that plausibly underlie the observed dielectric behavior. To confirm these structural changes are unique to the multiple-transition ternary compositions, high-temperature structural studies were performed on

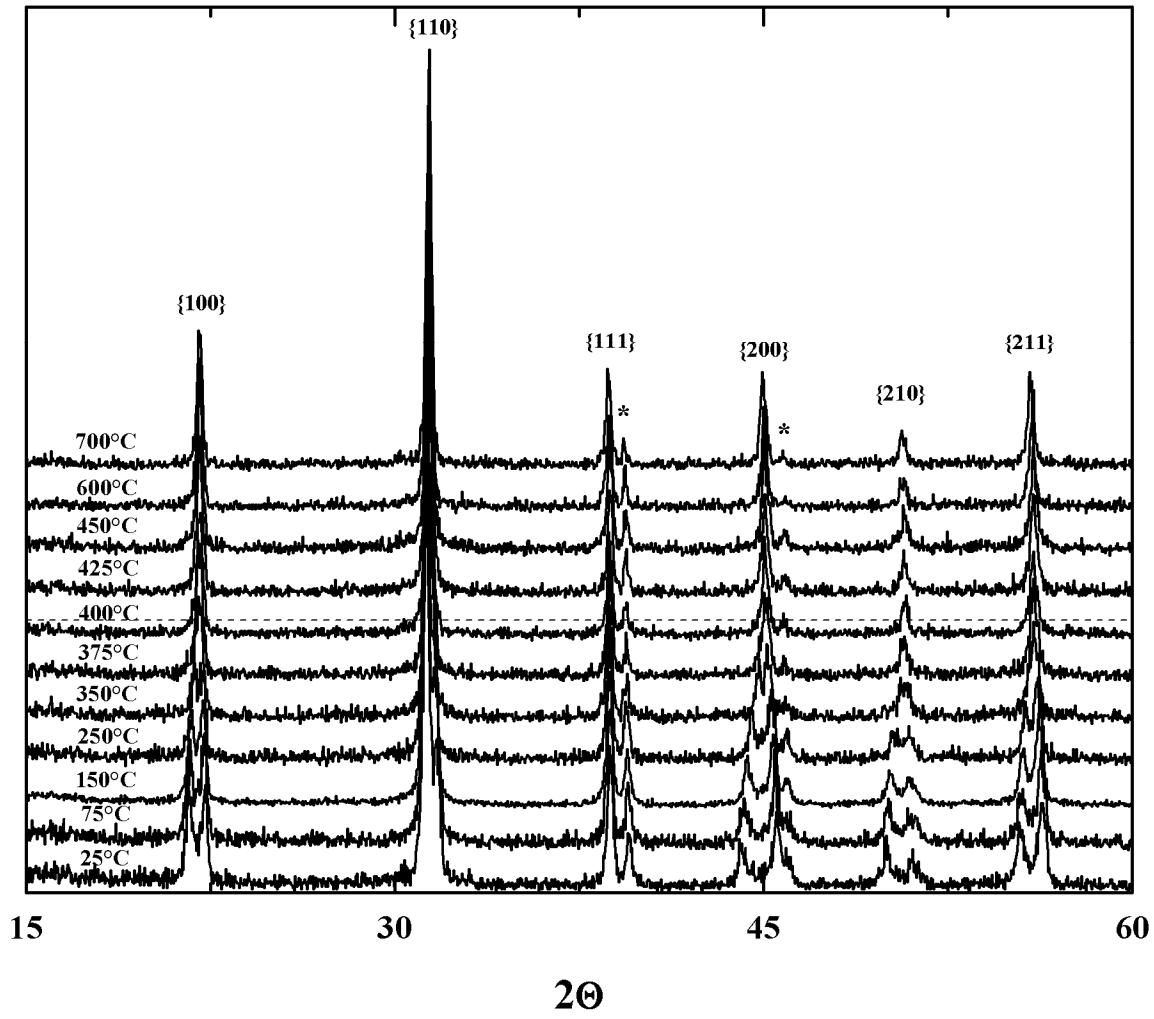

Figure 4.53: Laboratory powder diffraction patterns for the (0.7)[(0.9)PT – (0.1)BF]-(0.3)$BiScO_3$ composition for temperatures between 25°C and 700°C. The T_C for this composition (403ºC) is represented by the horizontal dashed line. Platinum peaks associated with the heating element are represented by "*".

compositions exhibiting customary single transitions. To this end, laboratory high-temperature X-ray diffraction studies were performed on (0.7)[(0.9)PT – (0.1)BF] – (0.3)$BiScO_3$ and (0.8)[(0.75)PT – (0.25)BF] – (0.2)BMT. The dielectric permittivity response for these samples was shown in Figures 4.44 and 4.45; the T_C for the $BiScO_3$-containg composition is 403°C and 490°C for the BMT-containing composition.

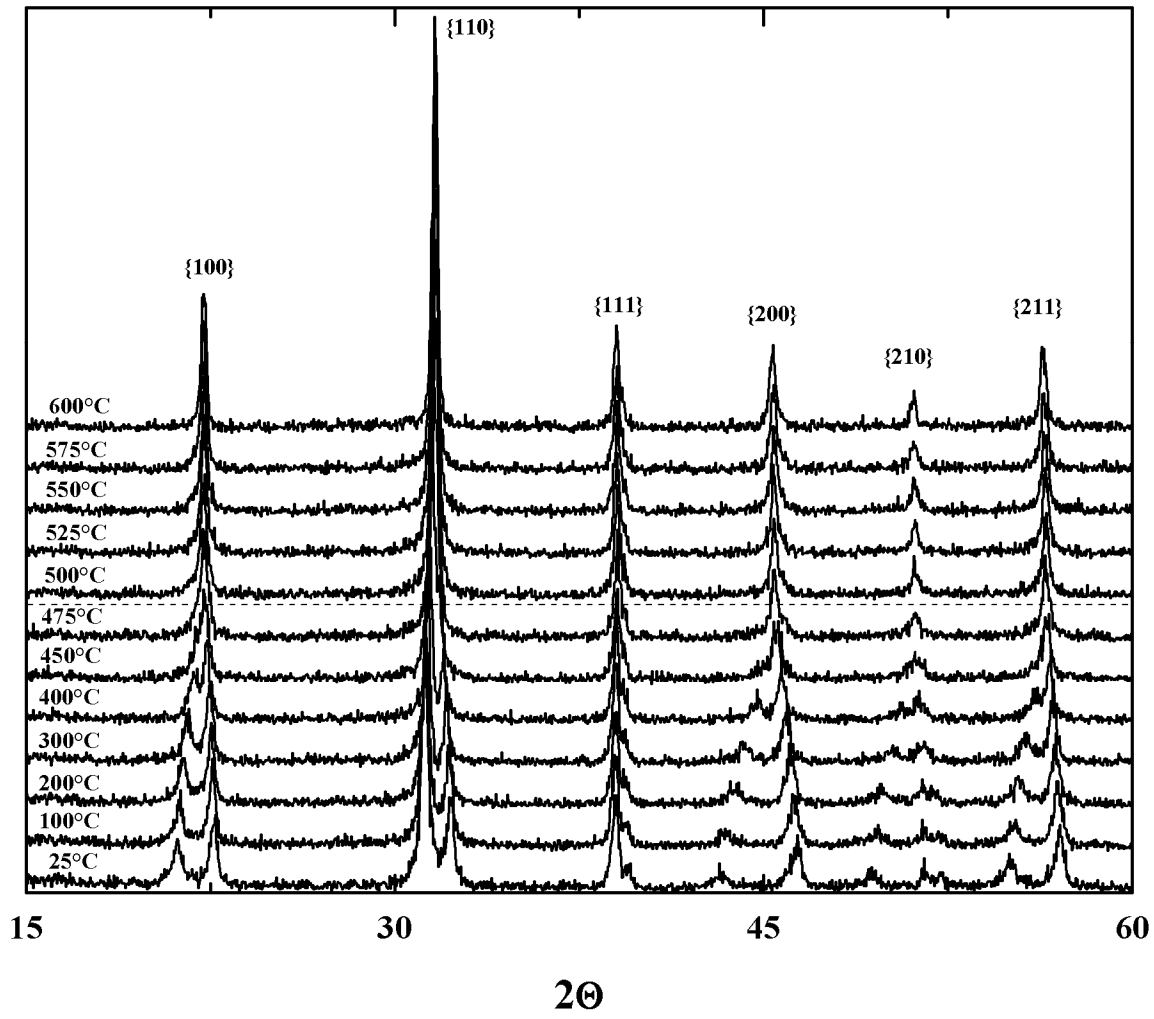

Figure 4.54: Laboratory powder diffraction patterns for the (0.8)[(0.75)PT – (0.25)BF]-(0.2)BMT composition for temperatures between 25°C and 600°C. The T_C for this composition (490ºC) is represented by the horizontal dashed line.

The temperature-dependent diffraction profiles are shown in Figures 4.53 and 4.54. Small peaks from the platinum strip holder were observed in the $BiScO_3$-containing composition, an artifact of the experimental setup. Figures 4.55 and 4.56 show the lattice parameters calculated by a least-squares refinement for both compositions. Both compositions exhibit behavior typical of tetragonal ferroelectrics with a continuous decrease in *c/a* with temperature and a loss of tetragonality at the Curie temperature.

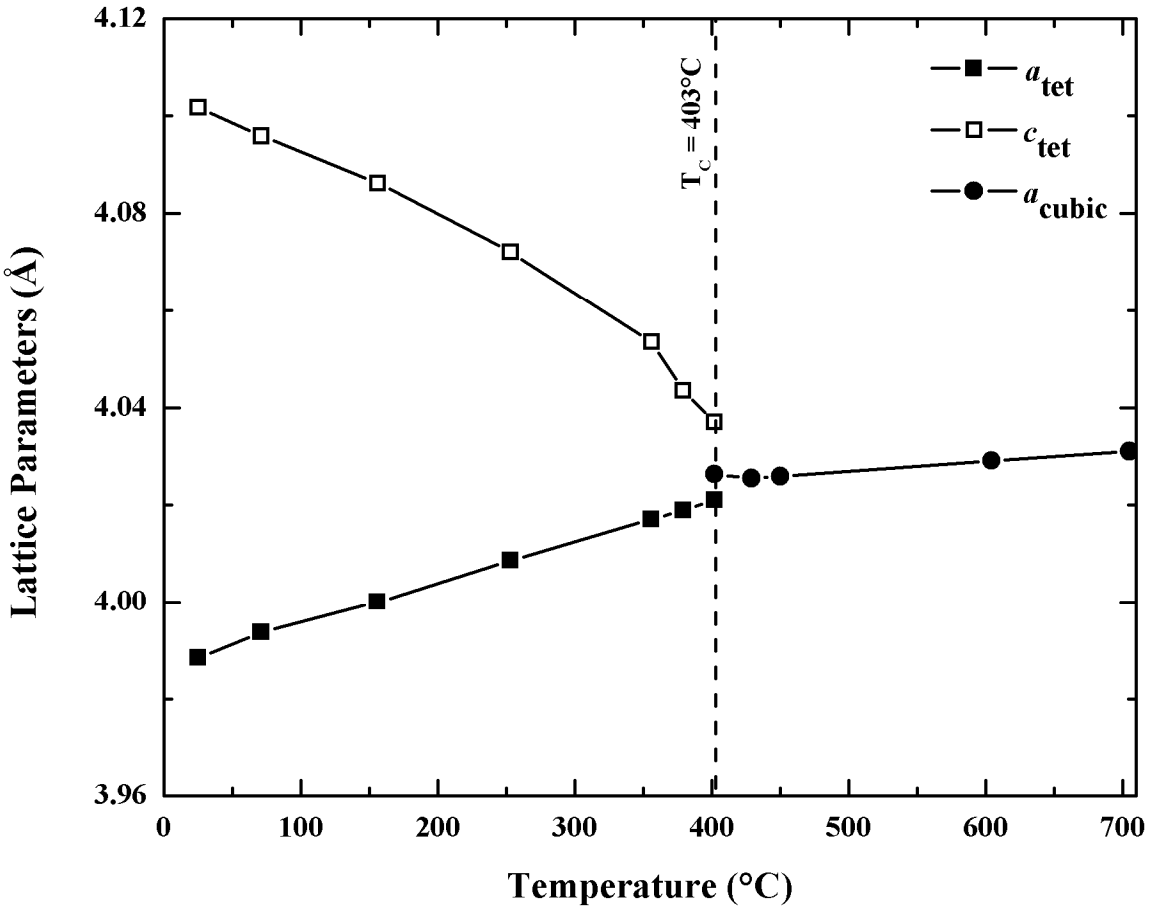

Figure 4.55: Lattice parameters as a function of temperature for the (0.7)[(0.9)PT – (0.1)BF] – (0.3)$BiScO_3$ composition.

There is no evidence for any region of 2-phase coexistence or persistent tetragonality.

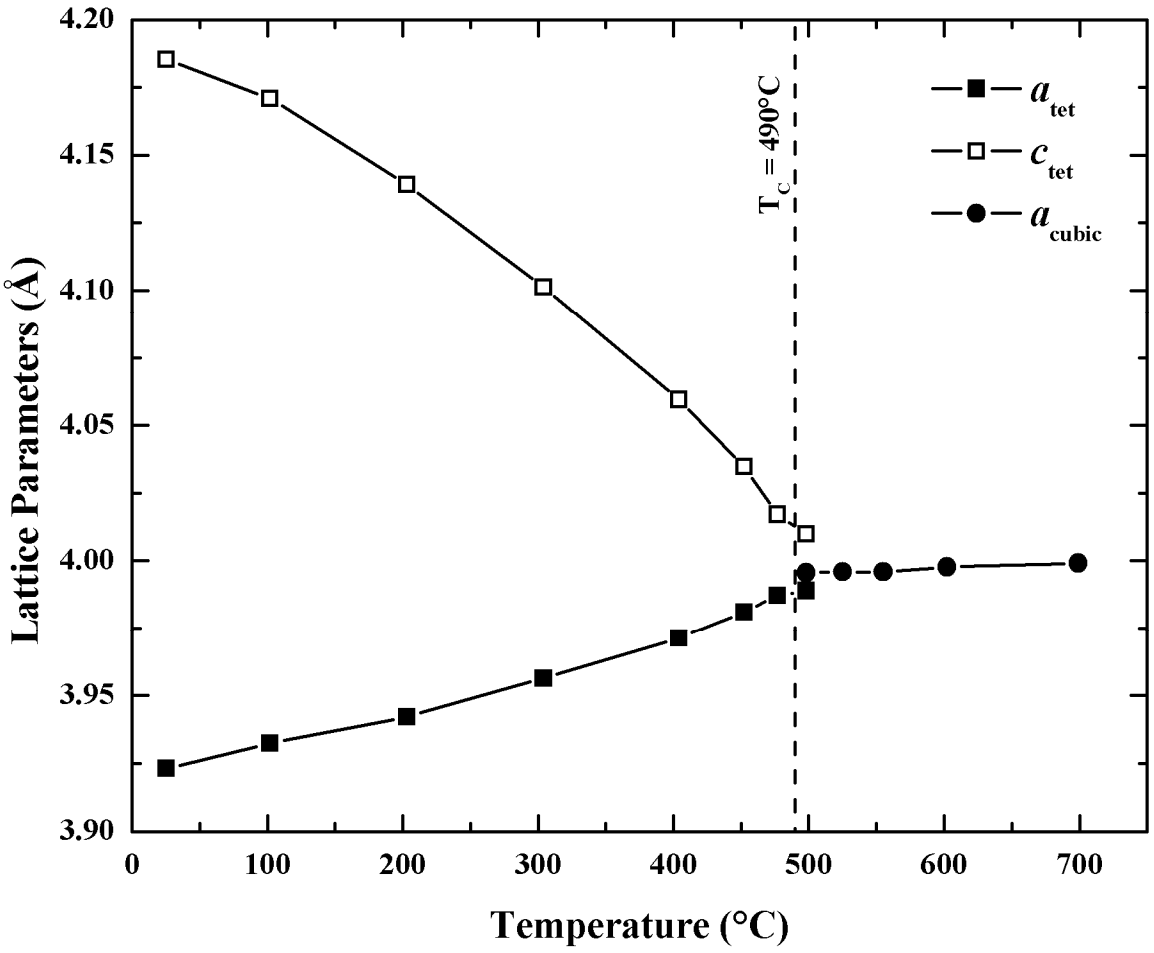

Figure 4.56: Lattice parameters as a function of temperature for the (0.8)[(0.75)PT – (0.25)BF] – (0.2)BMT composition.

4.5 Discussion

In this chapter ternary systems comprising PT, an enhanced tetragonality additive (BZT and $BiFeO_3$), and an MPB-forming additive (BMT, $BiScO_3$, and BMZ) were investigated with a view to stabilizing the enhanced tetragonality at an MPB for potential improvement of their piezoelectric properties. Each system features a mixed occupancy of Pb and Bi on the A-site and a B-site with a large occupancy of ferroelectrically-active cations. The modification of MPB-forming binary systems (PT-BMT, PT-$BiScO_3$, and PT-BMZ) by enhanced tetragonality additives can be understood as allowing the Bi content of the perovskite to be increased without reducing the ferroelectric activity of the B-site.

These modifications have produced unexpected structural and dielectric behavior, at least compared to existing empirical correlations. In each ternary, the location of the MPB moved toward the tetragonal end-member when the amount of the tetragonality-enhancing additive was increased. Also, many of the compositions that were tetragonal at room-temperature exhibited multiple dielectric transitions at elevated temperatures. This section discusses the phenomena and presents an analysis of their response in terms of their ionic displacements. This analysis was developed in collaboration with Dr. Ilya Grinberg.

4.5.1 MPB shifts

By increasing the *c/a* ratio of PT, enhanced tetragonality additives are thought to stabilize tetragonal distortions. However, a more stable tetragonal distortion would be

Table 4.8: MPB shifts in ternary systems. "Binary MPB (*x*)" is the location of the MPB in the binary system. "Shifted MPB (*x*)" is the location of the MPB in the pseudo-binary line with the BZT/BF content shown in "BZT/BF End-member content". "Crossover point (x)" is where *c* in pseudo-binary solution is equal to the binary system.

Ternary System	*Binary MPB (x)*	Shifted MPB (*x*)	BZT/BF End-member Content	Crossover Point (*x*)
PT-BZT-BMT	0.63	0.55	0.25	0.45
PT-BZT-$BiScO_3$	0.36	0.28	0.30	0.25
PT-BZT-BMZ	0.42	0.40	0.25	0.16
PT-BF-BMT	0.63	0.60	0.25	0.35
PT-BF-$BiScO_3$	0.36	0.30	0.25	0.22

expected to shift the location of an MPB away from the tetragonal end-member: more of the MPB-forming additive would be necessary to reduce the relative stability of the tetragonal phase compared to the rhombohedral phase and form an MPB. However, in the ternary systems of this chapter the opposite effect is observed; i.e. the rate of loss of tetragonality increases significantly as the *c/a* of the tetragonal end-member is increased. In Table 4.8 the positions of the MPB in the five ternary systems investigated are compared to the MPB in the corresponding binary with no enhanced-tetragonality additive. The movement of the MPB is directly related to a reversal in the effect of $Bi(Zn_{1/2}Ti_{1/2})O_3$ and $BiFeO_3$ on the *c/a* in the ternary system. Consider, for example, the PT-BZT-BMT system where the loss of tetragonality and formation of an MPB in the PT-BMT binary occurs at 63% substitution of BMT. The lattice parameters for the pseudo-binary lines in this system, Figure 4.5, indicate that below a certain "critical" BMT content the substitution of BZT into PT – BMT enhances tetragonality; for higher

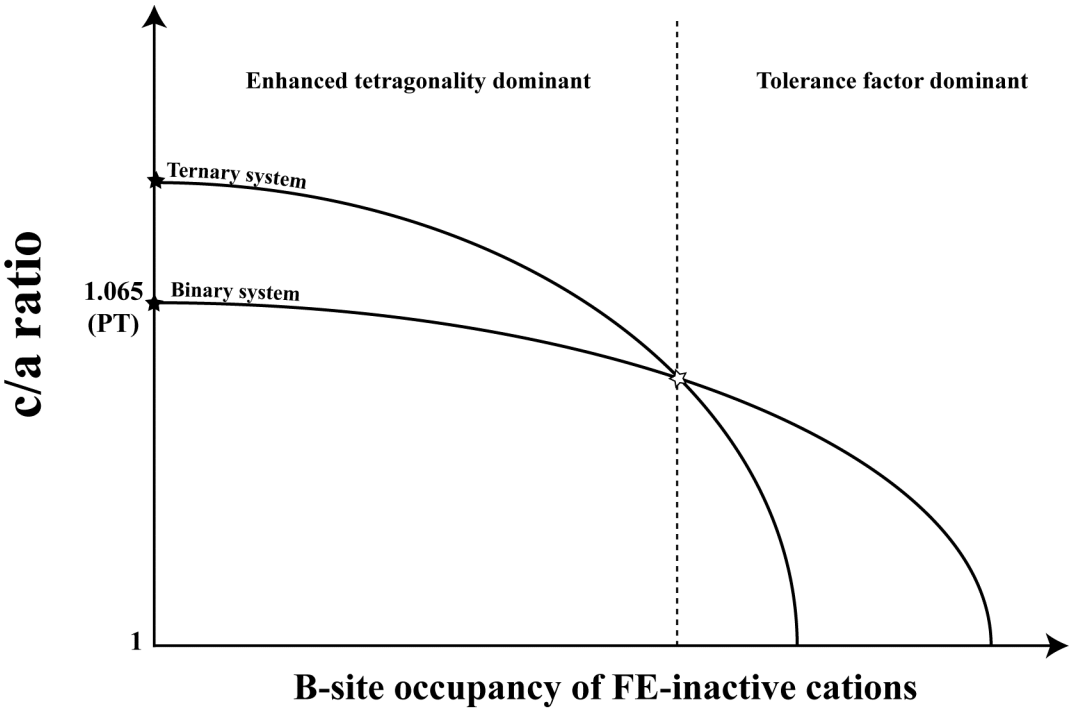

Figure 4.57: Schematic of the crossover point in a plot of *c/a* ratio for binary and ternary systems as a function of the B-site occupancy of FE-inactive cations.

concentrations of BMT, BZT induces a large reduction in *c/a*. For the (1-*x*)[75/25] - (*x*)BMT line this crossover (as gauged by the magnitude of the c axis) occurs at $x = 0.45$. To clarify, below 45% BMT the replacement of 25% PT by 25% BZT will increase *c* (and *c/a*), above 45% BMT the substitution of 25% BZT into PT reduces and, at 55% BMT, eliminates the macroscopic tetragonality. A schematic of this crossover point, as gauged by *c/a* instead of *c*, is shown in Figure 4.57.

The position of the crossover is dependent on the concentration of BZT. For (1-*x*)[90/10] – (*x*)BMT the *c* axis and *c/a* are increased only when the BMT content is less than ~ 20%. Again at high BMT concentration the replacement of 10% PT by 10% BZT reduces and ultimately eliminates (at 60% BMT) the bulk tetragonality. The reversal in

the effect of the BZT and BF additives is observed in every system (see Figures 4.5, 4.26, 4.34, 4.42 and 4.43) for each "MPB-forming" additive (BMT, BMZ, BS).

The position of the crossover varies with the concentration of the BZT and BF and with the identity of the MPB-forming additive and is difficult to rationalize or quantify using traditional radii or tolerance factor considerations alone. The change in the role of BZT and BF, from one that enhances *c/a* to one that reduces/eliminates the tetragonality, seems to be related to the overall concentration of ferroelectrically-active cations occupying the B-sites. Consider again PT-BZT-BMT. The enhancements in tetragonality occur when the B-site is occupied by high concentrations of cations such as Zn and Ti capable of undergoing large off-centering displacements (i.e. with high d^0 values). When these cations are replaced by relatively inactive cations with a low value of d^0 (Mg^{2+}) the character of the additive changes from one that can stabilize large Bi off-centering and high *c/a* via the collective coupling of the displacements on the A- and B-site sub-lattice site, to one where the inactive cations destabilize this interaction and the behavior is dominated by the reduction of the tolerance factor that accompanies the substitution of PT by BZT and BF. As discussed in Chapter 2, in almost all PT-based ferroelectric solid solutions the position of the MPB is related to the tolerance factor of the non-PT end-member. Specifically these empirical correlations reveal that the position of the MPB shifts toward PT-rich compositions as the tolerance factor is reduced. When the B-sites in the ternary systems contain significant proportions of low d^0 cations (M^{2+}, Zr^{4+}, Sc^{3+}) the role of BZT and BF therefore seems to change to one where the lower tolerance factor of the additive is dominant.

The observed movement of the MPB toward the tetragonal end-member in the high *c/a* BZT/BF ternaries might suggest that if the *c/a* of the end-member is reduced the MPB could be moved in the opposite direction. This possibility was tested by forming a solid solution of a PZT tetragonal end-member, $Pb(Zr_{0.3}Ti_{0.7})O_3$, with *c/a* lower than pure PT, with $BiScO_3$. Although extended solid solutions could be formed there was no evidence to support the movement of the MPB away from from the PZT end-member.

For several of the ternaries the position of the crossover from *c/a* enhancing to *c/a* reducing lies close to the compositions where the onset of multiple dielectric transitions was observed. The multiple transitions are discussed in the following section.

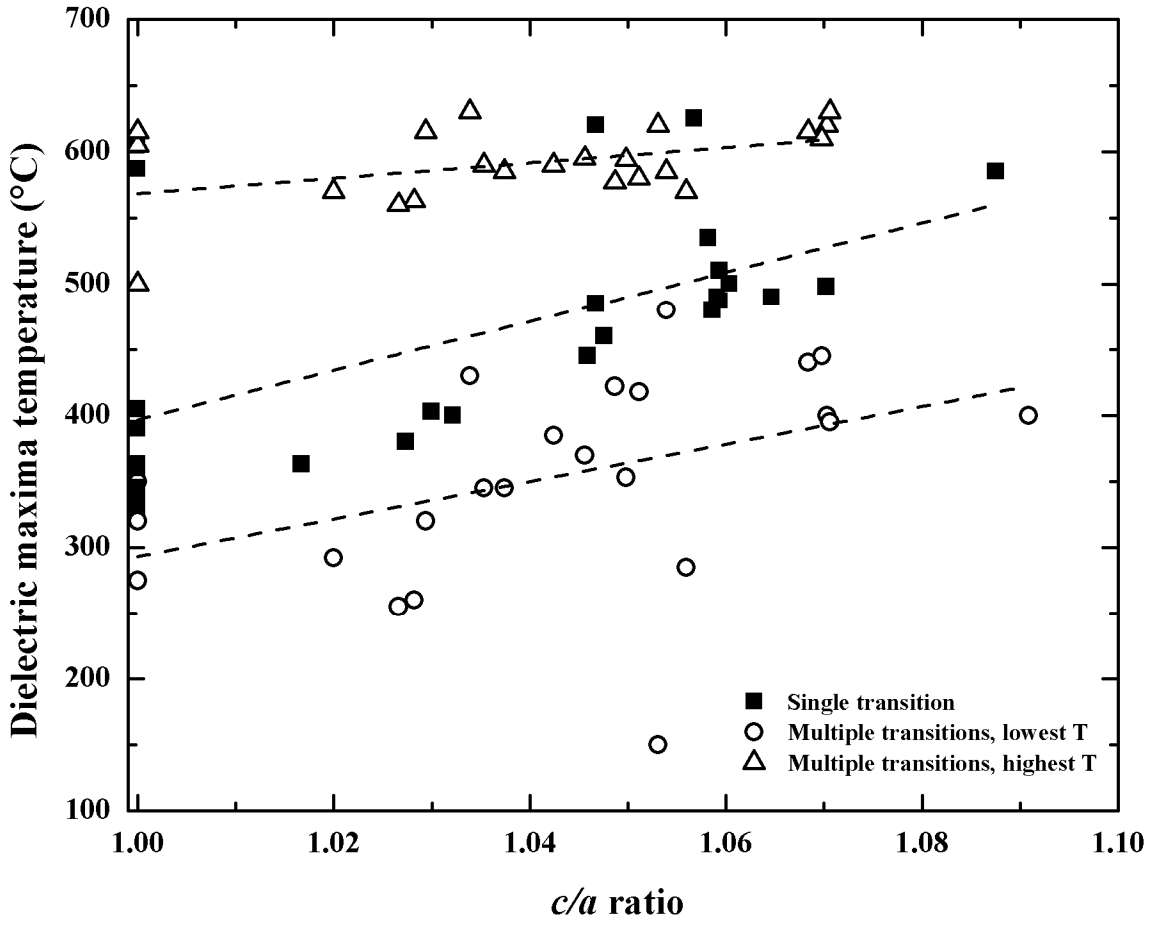

Figure 4.58: Dielectric maxima temperature as a function of *c/a* ratio for all ternary systems and PT-BMT binary. Compositions with multiple dielectric maxima are represented by open symbols, single dielectric maximum composition by closed symbols. Linear fits for each set of maxima temperatures and are also displayed.

4.5.2 Multiple dielectric transitions

Another unusual aspect of the Pb-Bi ternary systems is the appearance of multiple dielectric transitions in certain compositions (see Figure 4.10 for PT-BZT-BMT) where where normally the transformation from a tetragonal to cubic structure would be accompanied by a single maximum at the Curie temperature. In Figure 4.58 the temperatures of the dielectric transitions are plotted as a function of *c/a* of the room

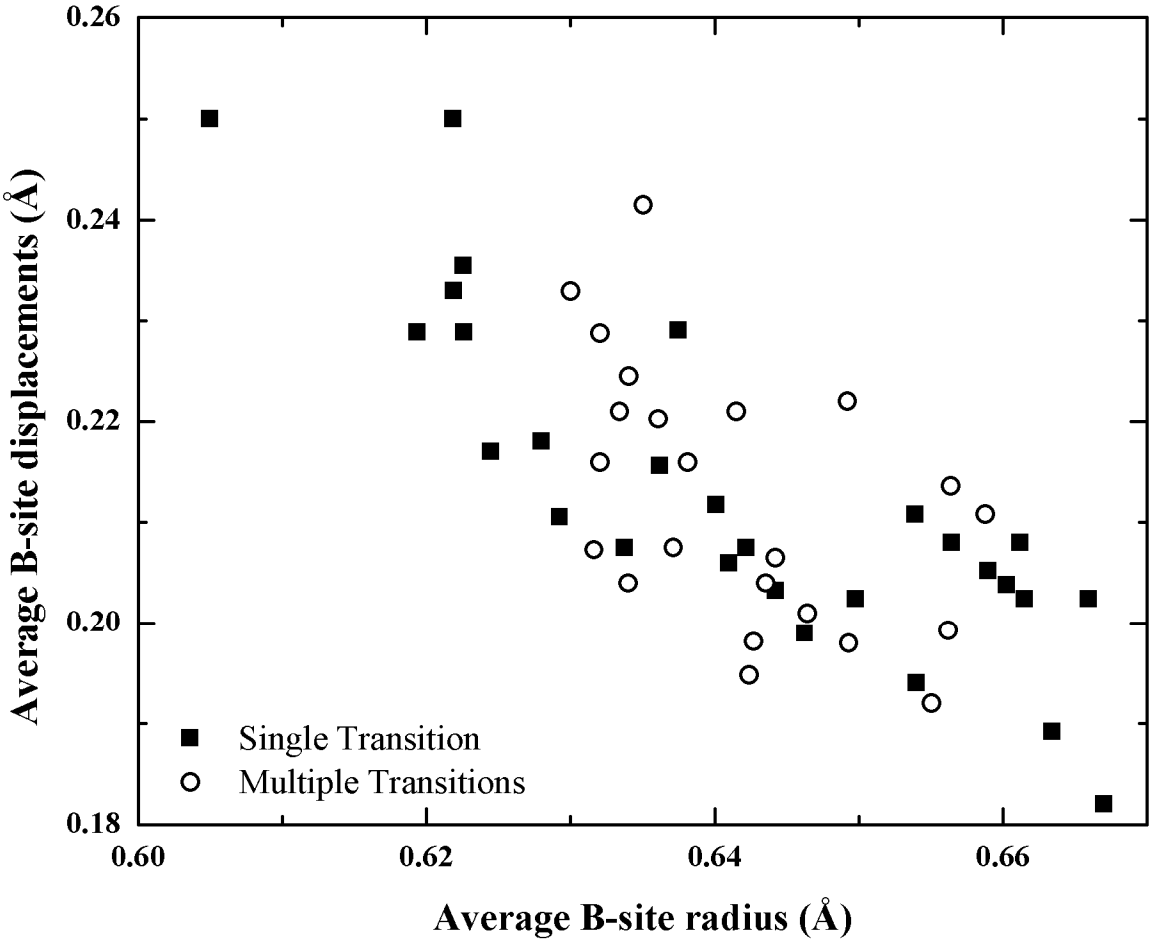

Figure 4.59: Observation of multiple dielectric peaks as a function of average B-site radius and displacements.

temperature structure for all of the compositions investigated.

Although a notable amount of scatter is observed in the transition temperatures, which is expected given the large range of compositions represented, linear fits of the data reveal that all the transition temperatures increase as the *c/a* ratio of the sample increases. Thus, the behavior of both transitions in the compositions with more than one dielectric maximum is consistent with the "normal" single transition samples, suggesting ferroelectric character for both. The transition for the majority of the single dielectric

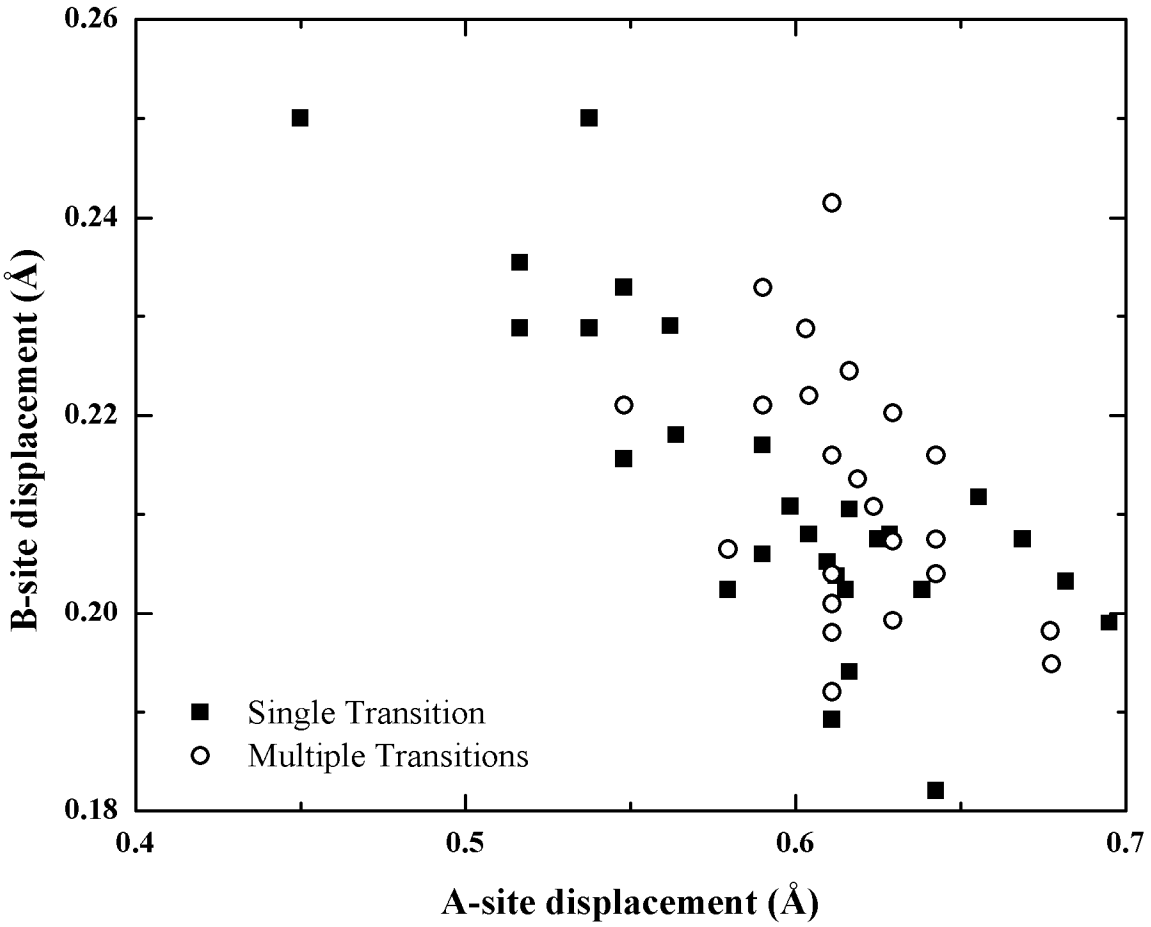

Figure 4.60: Observation of multiple dielectric peaks as a function of average A- and B-site displacements

maxima samples lie between the higher and lower temperatures of the multiple transition compositions. Given the observation of the coexistence of tetragonal and cubic mixtures in the high-temperature structure studies, the multiple dielectric maxima are most likely associated with phase separation. The multiple transition behavior is induced through modification of the binary MPB-forming systems by the BZT/BF tetragonality enhancing additives. While the *c/a* enhancement of PT by BZT and BF can be well-predicted by their cation displacements (d^0), values for the ternary system alone do a poor job of

predicting the multiple transition behavior. For example, Figures 4.59 and 4.60 show there is no well-defined correlation between the occurrence of multiple transitions and the B-site size and B-site displacement or the A- and B-site displacements. In both cases the compositions in the ternary systems are clustered in areas of large A- and B-site displacements, regardless of their dielectric characteristics.

The high-temperature structure behavior and the separation of the dielectric transitions revealed in the plot of T_C versus *c/a* in Figure 4.58 suggest the variance of cation displacements should also be considered. Because the A-site in these systems only contains two components, Pb^{2+} and Bi^{3+}, the average displacement and average A-site radius are closely coupled and it is unlikely that the variance in either A-site parameter would produce a correlation that is independent of their average value. On the other hand, the B-sites found in these systems contain multiple cations (Fe, Mg, Sc, Ti, Zn, Zr) and the variance of the B-site size and B-site displacements is independent of the average value and could be important in separating the behavior of the different systems.

A standard discrete variance function is therefore defined for the B-site displacements:

$$Var(d_B^0) = \sum_{i=1}^{n} p_i \cdot (d_i^0 - \overline{d}_B^0)^2$$

Where n is the number of B-site cation species, p_i is the B-site occupancy of the ith species (sum of p_i is 1), and $\overline{d}_B^0$ is the average B-site displacement. The variance of the B-site displacement is plotted against the average B-site displacement in Figure 4.61. In contrast to the average parameters used in Figures 4.59 and 4.60, when the variance in

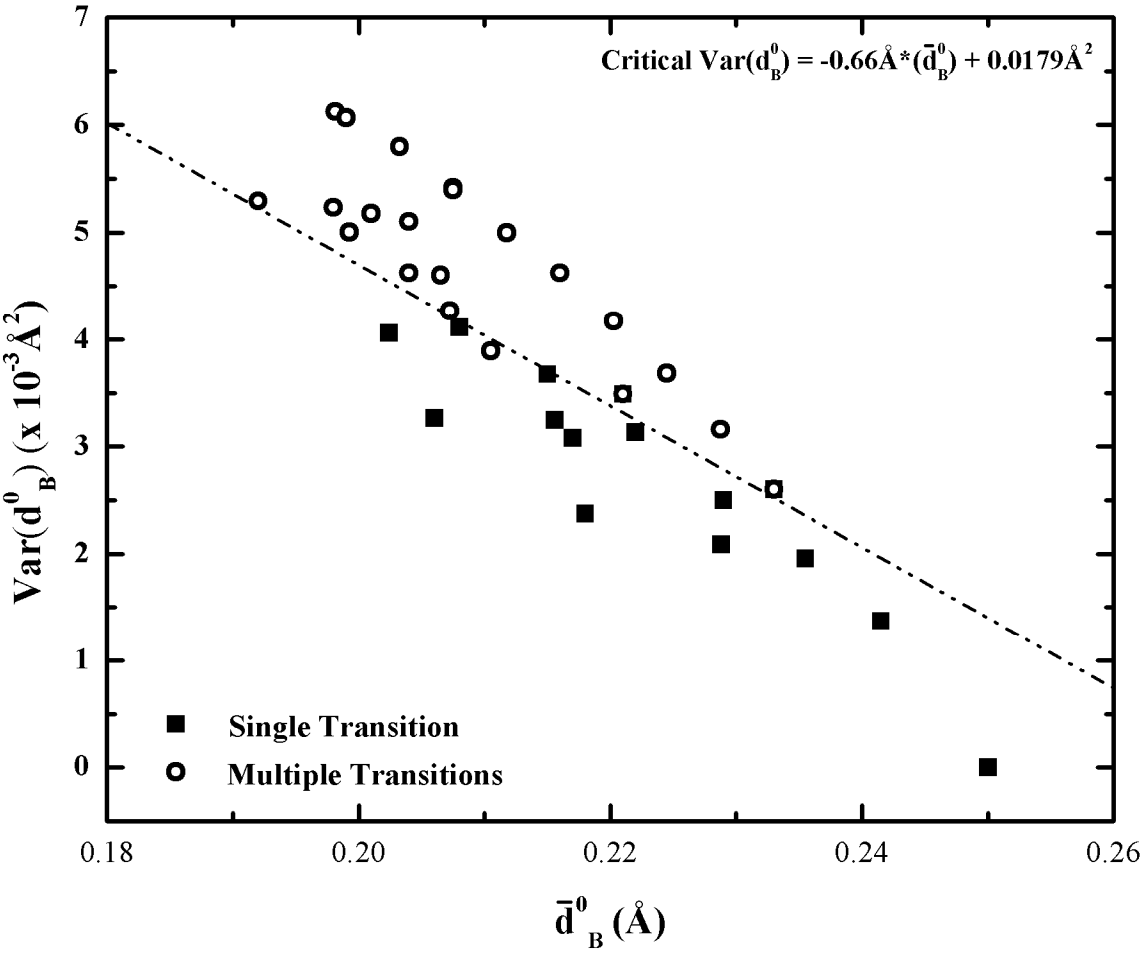

Figure 4.61: Incidence of MDP behavior as a function of B-site displacement and variance. The line separating the two sets of data is described by the equation in the upper left corner and is meant to be a guide for the eye.

displacement is introduced a strong delineation between single and multiple dielectric transition behavior is observed. Multiple dielectric transitions are observed in compositions where the B-site variance surpasses a critical value. This critical value is itself a function of the average B-site displacement. For a larger average B-site displacement (i.e. the more ferroelectrically-active cations that occupy the B-site, or the

larger the substitution of the enhanced tetragonality additive) a lower threshold B-site variance is required to induce multiple dielectric behavior.

The correlation of multiple dielectric transition behavior with the average B-site displacement and its variance does not imply independence with respect to the A-site chemistry. Multiple dielectric peak behavior has not been observed in pure Pb^{2+} A-site perovskites regardless of B-site chemistry. Furthermore, as noted in chapter 3, the (0.7)KBT – (0.3)BZT composition, which is lead-free but contains an A-site that is 65% Bi, exhibits a high temperature dielectric feature that is consistent with regard to the temperature and maximum permittivity to the multiple transitions in the Pb-Bi ternary systems, even though that composition has a pseudo-cubic room temperature structure. The occurrence of multiple dielectric transitions seems to be related to the occupancy of the A-site by Bi^{3+} and there appears to be some critical Bi^{3+} content to induce the transitions, but beyond that the behavior is driven by the B-site chemistry.

From this data it is possible to postulate a physical atomistic model to understand the multiple dielectric transitions. For example, consider (0.75)[(0.75)PT – (0.25)BZT] – (0.25)BMT (Figures 4.20-22). In this composition the A-site contains a ~44/56 mixture of Bi/Pb cations while the B-site comprises 87.5% ferroelectrically-active (Ti/Zn) and 12.5% non-active (Mg) cations. With a random population of the lattice, it can be expected that ~38% of the unit cells will contain a combination of Bi^{3+} and ferroelectrically-active nearest-neighbor B-site cations. The coupling between the Bi and B-site displacements will favor a large "local" tetragonality with a corresponding high T_C [Suchomel 2006]. The remaining 62% of cells contains a mixture of chemistries that are

also tetragonal with a lower *c/a* and a moderate T_C (Pb + Ti/Zn) as well as some cells that prefer non-polar symmetry (Mg-rich).

At room temperature, the average tetragonality, as gauged by X-ray diffraction has a *c/a* = 1.07. However, the significantly asymmetric broadening of the peaks in the diffraction data (see Figure 4.18) suggests a distribution of smaller tetragonal distortions also exist at the local-level. At the lower-temperature dielectric transition, the Pb-containing unit cells may transform to a non-polar symmetry while the Bi+Ti/Zn unit cells continue to retain local tetragonal distortions. As the temperature is increased, the cubic regions grow at the expense of the Bi-rich regions until at the second dielectric transition the remaining tetragonal regions reach their T_C. This process is illustrated schematically in Figure 4.62.

This postulated physical model is in many ways similar to those used to understand relaxor ferroelectric behavior. In relaxors polar nanoregions exist within a non-polar matrix and give rise to high-temperature dielectric transitions despite a macroscopically cubic symmetry. Here, it is postulated that "strongly polar" nanoregions exist within a polar matrix and these regions give rise to the observed high-temperature dielectric transitions.

This model may also explain some of the discrepancies observed in the correlation between the temperatures of the structural transitions which did not always show perfect agreement with the temperatures of the dielectric transitions. Finally, this "relaxor-type" model may also explain the behavior of (0.7)KBT – (0.3)BZT and (0.39)[75/25] – (0.61)BMT which both showed multiple dielectric transitions even though the structures were macroscopically pseudocubic at room temperature.

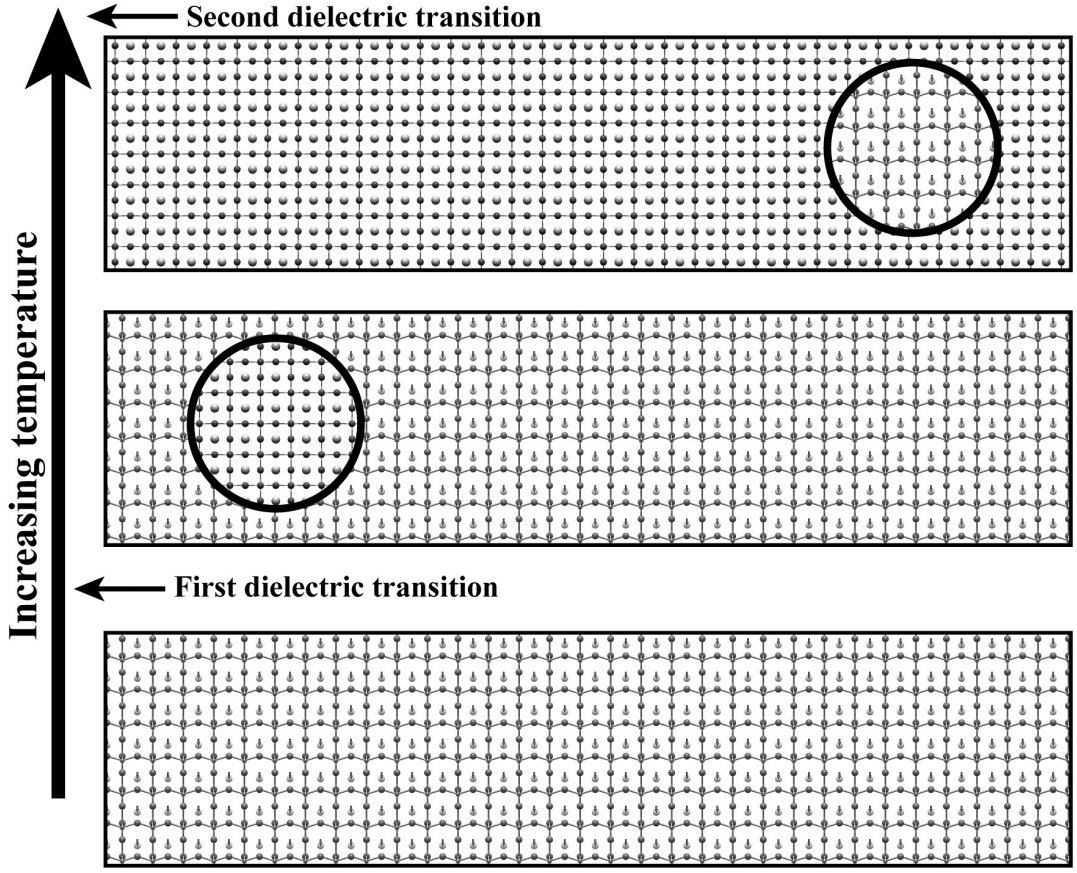

Figure 4.62: Schematic of the model postulated for multiple dielectric transition behavior. At room temperature, the entire crystal is tetragonal. At the first transition, small regions of the crystal transition to a cubic symmetry. These regions grow with temperature until only small regions are left with tetragonal symmetry that persist to the second transition.

Because this physical model involves phase separation and variations in the tetragonality at the nanoscale, it is clear that further validation will require structural techniques capable of improved spatial resolution. These and other suggestions for future work are discussed in the next chapter.

Chapter 5:

Summary and Future Directions

This thesis has focused on the stabilization of Bi-based perovskites through the formation of mixed A-site solid solutions. With an ideal electronic structure and small relative ionic size, these Bi^{3+}-containing perovskites have the potential to replace and improve upon the dielectric and piezoelectric properties of their lead-based counterparts.

Building on the discovery that additives such as $Bi(Zn_{1/2}Ti_{1/2})O_3$ increase the tetragonality and Curie temperatures of $PbTiO_3$, the first part of this work sought to indentify new substituents that could increase *c/a*. In chapters 3 and 4 these additives were used in an attempt to enhance the tetragonality of lead-free perovskites and improve the piezoelectric properties of existing mixed Pb/Bi A-site perovskites, respectively.

In chapter 2, $Bi(Zn_{3/4}W_{1/4})O_3$ was identified as a new tetragonality-enhancing additive and the successful synthesis of PT - $Bi(Zn_{3/4}W_{1/4})O_3$ solid solutions clarified the crystal chemical criteria required to increase the *c/a* of $PbTiO_3$. While the occupancy of the A-site by Bi^{3+} is the major driving force for the *c/a* enhancement, occupancy of the B-site by cations capable of undergoing large cooperative displacements (large d^0) to minimize the Bi^{3+} - B-cation repulsive forces was found to be critical in stabilizing the enhanced tetragonality.

$Bi(Zn_{3/4}W_{1/4})O_3$, $Bi(Zn_{1/2}Ti_{1/2})O_3$, $BiFeO_3$, and $Bi(Zn_{2/3}Nb_{1/3})O_3$ are the only substituents known to induce enhanced tetragonality. In each case the B-site lattice is

occupied by cations with large values of d^0; in contrast, additives such as $BiScO_3$, where Sc^{3+} has a low d^0 value, destabilize the tetragonal phase. The activity of $Bi(Zn_{3/4}W_{1/4})O_3$ is primarily due to the high concentration of Zn^{2+} and its substitution into PbTiO also enhances the Curie temperature.

In chapter 3, a member ($Bi(Zn_{1/2}Ti_{1/2})O_3$) of this select group of additives was substituted into lead-free perovskite end-members in an attempt to stabilize a new generation of environmentally benign ferroelectric materials. The ranges of solubility in the systems investigated were limited by impurity formation and no evidence was found for enhanced tetragonality.

It was concluded that the co-occupancy of the A-site by ferroelectrically inactive cations (e.g. K, Ba, Na) suppressed any correlated displacements of Bi^{3+} through cation-cation repulsive forces. A family of potentially interesting dielectrics were discovered in the KBT-BZT system with a Curie-type transition close to 600°C.

Chapter 4 explored a series of ternary systems in an attempt to capture the high *c/a* of the mixed Pb-Bi systems at an MPB. In the PT-BZT-BMT system, the T_C at the MPB of one of the pseudo-binary lines was found to be far higher (~600°C) than in any previously reported system. The behavior of these systems, however, was complicated by a series of multiple dielectric transitions prior to the transformation to a cubic, paraelectric state. The multiple dielectric transitions were observed in a region of the ternary diagram characterized by large Bi A-site occupancy and high occupancy of ferroelectrically-active B-site cations. Variable temperature diffraction studies revealed

the first dielectric transition was accompanied by a 2-phase coexistence of tetragonal and cubic phases and a region of "persistent tetragonality", while the high temperature transition corresponds to a transformation to a single-phase cubic symmetry. While the higher temperature T_Cs at the MPBs observed in this ternary are some of the highest reported, the room temperature properties are limited by a transformation to a relaxor state which did not exhibit any significant piezoelectric response.

Multiple dielectric transitions and MPB formation were also observed when $Bi(Mg_{1/2}Zr_{1/2})O_3$ and $BiScO_3$ were added to PT-BZT. Variable-temperature diffraction studies of the BMZ-containing system confirmed these are accompanied by 2-phase coexistence between the two dielectric transitions.

This behavior was not limited to BZT-containing ternaries and its replacement by another tetragonality-enhancing additive, $BiFeO_3$, yielded similar results in the BMT-containing ternary, but single transitions in a $BiScO_3$-containing system. Diffraction studies of the PT - $BiFeO_3$ – BMT system reaffirmed the multiple dielectric transitions arise from a 2-phase coexistence at elevated temperature.

These studies also revealed a crossover in the effect of $Bi(Zn_{1/2}Ti_{1/2})O_3$ and $BiFeO_3$ (and by inference $Bi(Zn_{3/4}W_{1/4})O_3$) on the tetragonality of $PbTiO_3$-containing ferroelectrics. For example the substitution of BZT into the PT-BMT binary only enhances *c/a* up to a critical composition of BMT. Beyond this limit the *c/a* is decreased dramatically, an effect likely related to the lower tolerance factor of BZT compared to PT.

The data from all the ternary systems were used to systematize the appearance of multiple dielectric transitions using crystal-chemical parameters, such as average cation size and/or average A- and B-site ion displacement factors (d^0). These parameters alone were not successful in differentiating the compositions with multiple transitions from those with "normal" single permittivity maxima. However, by introducing a new parameter that describes the variance of the cation displacements, a combination of the average B-site displacement and its variance was successful in delineating compositions with multiple transitions.

To explain the appearance of multiple transitions an atomistic model was developed where polar, Bi-rich nanoscale clusters are formed within a less polar, Pb-rich matrix. This model is similar to those of relaxor ferroelectrics. The different local Curie temperatures in the clusters and matrix are suggested to lead to the multiple dielectric transitions.

The results of this dissertation offer several promising directions for future work. The high-temperature dielectric and structural behavior of compositions that exhibit multiple dielectric transitions imply a relatively frustrated structure with at least some ferroelectric regions at temperatures up to the second dielectric transition. Testing at elevated temperatures will allow the piezoelectric response to be quantified as well as provide indirect information on what fraction of the sample is ferroelectric and the force needed to switch between the two phases.

In this thesis the structure studies of compositions in the PT-BZT-BMT, PT-BZT-BMZ, and PT-BF-BMT systems relied on synchrotron X-ray and neutron diffraction. It is clear these systems exhibit inhomogeneity in their structure at the nanoscale and future studies should utilize spatially resolved TEM imaging and diffraction. Those investigations should use in-situ heating stages to examine the changes in local tetragonality throughout the 2-phase coexistence region and would also allow observation of strain effects at the interfaces between the different nanoscale phases.

With the apparently frustrated structure observed in these systems, information about local atomic environments (bond-lengths, coordination) would also seem worthwhile. Pair-distribution function (PDF) analysis can provide this information.

There are also additional strategies for exploring the stabilization of highly tetragonal lead-free systems. Large A-site cations, such as Ba^{2+} tend to suppress the correlation of Bi^{3+} displacements, but they are also tend to stabilize the perovskite phase. Systems involving smaller A-site cations have small solubility ranges before non-perovskite structures appear. It may be possible to find a region in a ternary phase diagram, e. g. $BaTiO_3$ – $CaTiO_3$ – BZT or similar, where a single phase perovskite structure is stabilized but the A-site occupancy of the larger non-Bi cation is small enough to allow for the Bi^{3+} displacements to correlate, leading to a lead-free system with enhanced tetragonality.

Appendix A:

Rietveld Refinement Models

In chapter 4, a number of Rietveld refinement models were tested to obtain a model with the best fit for diffraction data obtained at temperatures where neither the room temperature tetragonal (P4mm) or high-temperature cubic (Pm3m) phases were clearly the correct symmetry. This appendix expounds on that process.

The samples of chapter 4 with tetragonal room temperature symmetries exhibited asymmetric peak broadening that needed to be taken into account when determining the lattice parameters. For those samples that were studied by variable-temperature diffraction, particularly the (0.5)[90/10] – (0.5)BMT composition studied by neutron diffraction, this broadening results in structural ambiguity at temperatures between the dielectric transitions of the sample. In (0.5)[90/10] – (0.5)BMT this is compounded by the relatively low resolution of neutron diffraction compared to synchrotron studies. A variety of models were fit to the experimental data obtained at 425°C in order to determine the symmetry with the best fit

The following symmetry models were fit to the experimental data: P4mm-type tetragonal symmetry, Pm3m-type cubic, 2-phase coexistence of P4mm & Pm3m, and rhombohedral R3c- and R3m-type symmetries. Tables A.1 –A.5 list the structural and reliability parameters for the five models. All models also included an Fm-3m-type Fe phase to account for peaks associated with the sample holder. Profiles were fit with

GSAS profile type 3 and the background was modeled by a shifted Chebyschev function with nine terms.

The R3c structure has the worst fit of all five models, which is to be expected because the (111) peak is a systematic absence in that symmetry while that peak is the strongest experimental peak. The single-phase Pm3m cubic and R3m rhombohedral models fit the experimental data equivalently. Neither model is able to accurately model the intensity around the (200) peak family. The 2-phase coexistence model was expected to show the best fit given its extra degrees of freedom. However, it was unable to model the experimental data as well as the single-phase P4mm model. This may be related to limitations of the GSAS routines to properly fit profile peaks when multiple phases overlap so strongly.

Table A.1: Refined structural and reliability parameters for the (0.5)[(0.9)PT-(0.1)BZT]-(0.5)BMT composition using neutron data and a P4mm-type structure model.

Phase	a_{tet} Å	c_{tet} Å	U_A x100 Å^2	U_B x100 Å^2	U_{O1} x100 Å^2	U_{O2} x100 Å^2	R_F^2	χ^2
P4mm	3.9827	4.0323	0.05193	0.01086	0.05606	0.03798	0.0969	1.690

Table A.2: Refined structural and reliability parameters for the (0.5)[(0.9)PT-(0.1)BZT]-(0.5)BMT composition using neutron data and a Pm3m-type structure model.

Phase	a_{cubic} Å	U_A x100 Å^2	U_B x100 Å^2	U_O x100 Å^2	R_F^2	χ^2
Pm3m	4.0010	0.01947	0.16344	0.06838	0.1215	3.729

Table A.3: Refined structural and reliability parameters for the (0.5)[(0.9)PT-(0.1)BZT]-(0.5)BMT composition using neutron data and a 2-phase coexistence of P4mm- and Pm3m-type structures.

Phase	a_{tet} Å	c_{tet} Å	U_A x100 Å^2	U_B x100 Å^2	U_{O1} x100 Å^2	U_{O2} x100 Å^2	R_F^2	χ^2
P4mm	3.9765	4.0603	0.05196	0.01083	0.05621	0.03794	0.1662	2.529

Phase	a_{cubic} Å	U_A x100 Å^2	U_B x100 Å^2	U_O x100 Å^2
Pm3m	3.9999	0.06810	0.04945	0.04887

Table A.4: Refined structural and reliability parameters for the (0.5)[(0.9)PT-(0.1)BZT]-(0.5)BMT composition using neutron data and a R3c-type structure model.

Phase	a_{tet} Å	α °	U_A x100 Å^2	U_B x100 Å^2	U_O x100 Å^2	R_F^2	χ^2
R3c	3.9946	90.3437	0.03142	0.02185	0.05051	0.5223	16.27

Table A.5: Refined structural and reliability parameters for the (0.5)[(0.9)PT-(0.1)BZT]-(0.5)BMT composition using neutron data and a R3m-type structure model.

Phase	a_{tet} Å	α °	U_A x100 Å^2	U_B x100 Å^2	U_O x100 Å^2	R_F^2	χ^2
R3m	4.0007	90.0339	0.27933	0.11184	0.03846	0.1162	3.854

Bibliography

Ahtee, M., and Glazer A. M., *High-temperature phases of sodium niobate-potassium niobate solid solutions*. Ferroelectrics, 1976. **12:** p. 205-206.

Atou, T., Chiba, H., Ohoyama, K., Yamaguchi, Y., and Syono, Y., *Structure Determination of Ferromagnetic Perovskite $BiMnO_3$*. Journal of Solid State Chemistry. 1999. **145**: p. 639-642.

Baettig, P., Schelle, C. F., LeSar, R., Waghmare, U. V., and Spaldin, N. A., *Theoretical Prediction of New High-Performance Lead-Free Piezoelectrics*. Chemistry of Materials. 2005. **17**: p. 1376-1380.

Belik, A. A., Iikubo, S., Kodama, K., Igawa, N., Shamoto, S., Niitaka, S., Azuma, M., Shimakawa, Y., Takano, M., Izumi, F., and Takayama-Muromachi, E., *Neutron Powder Diffraction Study on the Crystal and Magnetic Structures of $BiCoO_3$*. Chemistry of Materials. 2006. **18**: p. 798-803.

Belik, A. A., Wuernisha, T., Kamiyama, T., Mori, K., Maie, M., Nagai, T., Matsui, Y., and Takayama-Muromachi, E., *High-Pressure Synthesis, Crystal Structures, and Properties of Perovskite-like $BiAlO_3$ and Pyroxene-like $BiGaO_3$*. Chemistry of Materials. 2006. **18**: p. 133-139.

Bellaiche, L., Garcia, A., and Vanderbilt, D., *Finite-Temperature Properties of $Pb(Zr_{1-x}Ti_x)O_3$ Alloys from First Principles*. Phyiscal Review Letters. 2000. **84**(23): p. 5427-5430.

Bennett, J. W., Grinberg, I., and Rappe, A. M., *Nonmonotonic Composition Dependence of the Dielectric Response of $Ba_{1-x}Ca_xZrO_3$*. Chemistry of Materials. 2008. **20**: p. 5134-5138.

Bennett J, Grinberg I, and Rappe A. *Effect of substituting of S for O: The sulfide perovskite BaZrS3 investigated with density functional theory*. Physical Review B. 2009. **79**(23): p. 1-6.

Bridges, C. A., Allix, M., Suchomel, M. R., Kuang, X., Sterianou, I., Sinclair, D. C., and Rosseinsky, M. J., *A Pure Bismuth A Site Perovskite Synthesized at Ambient Pressure*. Angewandte Chemie. 2007. **119**: p. 8941-8945.

Brown I. D., and Wu K. K., *Empirical parameters for calculating cation–oxygen bond valences*. Acta Crystallographica Section B Structural Crystallography and Crystal Chemistry. 1976. **32**(7): p. 1957-1959.

Brown I. D., *Bond valences: a simple structural model for inorganic chemistry*. Chemical Society Reviews. 1978. **7**(3): p. 359-376.

Buhrer C. F., *Some Properties of Bismuth Perovskites*. The Journal of Chemical Physics. 1962. **36**(3): p. 798.

Cohen, R., *Origin of ferroelectricity in perovskite oxides*. Nature. 1992. **358**: p. 136-138.

Dalesio, L. R., Hill, J. O., Kraimer, M., Lewis, S., Murray, D., Hunt, S., Watson, W., Clausen, M., and Dalesio, J. *The Experimental Physics and Industrial Control-*

System Architecture - Past, Present, and Future, Nuclear Instruments & Methods in Physics Research Section A - Accelerators Spectrometers Detectors and Associated Equipment. 1994. **352**: p. 179-184.

Davies P, K. *Cation ordering in complex oxides.* Current Opinion in Solid State and Materials Science. 1999. **4**(5): p. 467-471.

Davies P. K., Wu H., Borisevich A. Y., Molodetsky I. E., and Farber L. *Crystal Chemistry of Complex Perovskites: New Cation-Ordered Dielectric Oxides*. Annual Review of Materials Research. 2008. **38**(1): p. 369-401.

Dmowski, W., Akbas, M. K., Davies, P. K., and Egami, T., *Local Structure of $Pb(Sc_{1/2},Ta_{1/2})O_3$ and related compounds*. Journal of Physics and Chemistry of Solids. 2000. **61**: 229-237.

Duan, R., Speyer, R. F., Alberta, E., and Shrout, T. R., *High Curie temperature perovskite $BiInO_3$-$PbTiO_3$ ceramics*. Journal of Materials Research. 2004. **19(7)**: p. 2185-2193.

Egami, T., Mamontov, E., and Dmowski, W., *Temperature Dependence of the Local Structure in Pb Containing Relaxor Ferroelectrics*. Fundamental Physics of Ferroelectrics 2003, American Institute of Phyiscs. 2003. p. 48-54.

Eitel, R. E., Randall, C. A., Shrout, T. R., Rehrig, P. W., Hackenburger, W., and Park, S. E., *New High Temperature Morphotropic Phase Boundary Piezoelectrics Based*

on Bi(Me)O_3-PbTiO_3 Ceramics. Japanese Journal of Applied Physics. 2001. **40**(10): p. 5999-6002.

Eitel R. E., Randall C. A., Shrout T. R., and Park S-E. *Preparation and Characterization of High Temperature Perovskite Ferroelectrics in the Solid-Solution (1-x)BiScO_3-x$PbTiO_3$*. Japanese Journal of Applied Physics. 2002. **41**(Part 1, No. 4A): p. 2099-2104.

Fedulov S. A., *Determining the Cuire point of BiFeO3 Ferroelectric*. Doklady Akademii Nauk SSSR. 1961. **139**(6): p. 1345-1346.

Fedulov, S. A., *Complete Phase Diagram of the PbTiO_3-BiFeO_3 System*. Soviet Phyiscs – Solid State. 1964. **6**(2): p. 375-377.

Filip'ev, V. S., Smolyaninov, N. P., Fesenko, E. G., and Belyaev, I. N., *Formation of BiFeO_3 and Determination of Unit Cell*. Krystallografiya. 1960. **5**: p. 958-960.

Fornari M., and Singh D. J., *Possible coexistence of rotational and ferroelectric lattice distortions in rhombohedral Pb$Zr_xTi_{1-x}O_3$*. Physical Review B. 2001. **63**(9): p. 1-4.

Francombe, M. H., and Lewis, B., *Structural and Electrical Properties of Silver Niobate and Silver Tantalate*. Acta Crystallographica. 1958. **11**(3): p. 175-178.

Fujishita H., and Katano S. *Re-examination of the antiferroelectric structure of PbZrO_3*. Journal of the Physical Society of Japan. 1997. **66**(11): p. 3484–3488.

Fukada E., *Piezoelectricity of wood*. Journal of the Phyical Society of Japan. 1955. **10**: p. 149–154.

Glazer A. M., *The classification of tilted octahedra in perovskites*. Acta Crystallographica Section B Structural Crystallography and Crystal Chemistry. 1972. **28**(11): p. 3384-3392.

Goldschmidt V. M., *Crystal structure and chemical constitution.* Transactions of the Faraday Society. 1929. **25**. p. 253-283.

Grinberg, I., Cooper, V. R., and Rappe, A. M., *Relationship between local structure and phase transitions of a disordered solid solution*. Nature. 2002. **419**: 909-911.

Grinberg, I., Cooper, V., and Rappe, A., *Oxide Chemistry and local structure of $PbZr_xTi_{1-x}O_3$ studied by density-functional theory supercell calculations*. Physical Review B. 2004. **69**: 144118.

Grinberg, I., and Rappe, A., *Local Structure and macroscopic properties in $PbMg_{1/3}Nb_{2/3}O_3$-$PbTiO_3$ and $PbZn_{1/3}Nb_{2/3}O_3$-$PbTiO_3$*. Physical Review B. 2004. **70**: 220101.

Grinberg, I., Suchomel, M. R., Davies, P. K., and Rappe, A. M., *Predicting morphotropic phase boundary locations and transition temperatures in Pb- and Bi-based perovskite solid solutions from crystal chemical data and first-principles calculations*. Journal of Applied Physics. 2005. **98**: 094111.

Grinberg I., Suchomel M. R., Dmowski W., Mason. S. E., Wu H., Davies P. K., and Rappe A. M., *Structure and Polarization in the High T_c Ferroelectric $Bi(Zn,Ti)O_3$-$PbTiO_3$ Solid Solutions*. Physical Review Letters. 2007. **98**(10): p. 107601.

Guiton B. S., and Davies P. K., *Nano-chessboard superlattices formed by spontaneous phase separation in oxides*. Nature materials. 2007. **6**(8): p. 586-91.

Guo H. Y., Lei C., and Ye Z-G., *Re-entrant type relaxor behavior in $(1-x)BaTiO_3$–$xBiScO_3$ solid solution*. Applied Physics Letters. 2008. **92**(17): p. 172901.

Huang, C., and Cann, D. P., *Phase transitions and dielectric properties in $Bi(Zn_{1/2}Ti_{1/2})O_3$-$BaTiO_3$ perovskite solid solutions*. Journal of Applied Physics. 2008. **104**: 024117.

Hughes, H., Allix, M. M. B., Bridges, C. A., Claridge, J. B., Kuang, X., Niu, H., Taylor, S., Song, W., and Rosseinsky, M. J., *A Polar Oxide with a Large Magnetization Synthesized at Ambient Pressure*. Journal of the American Chemical Society. 2005. **127**: p. 13790-13791.

Iniguez, J., Vanderbilt, D., and Bellaiche, L., *First-principles study of $(BiScO_3)_{1-x}$-$(PbTiO_3)_x$ piezoelectric alloys*. Physical Review B. 2003. **67**: 224107.

Jaeger R. E., *Hot Pressing of Potassium-Sodium Niobates*. Journal of the American Ceramic Society. 1962. **43**(10): p. 517-213.

Jones G., Kreisel J., Jennings V., Geday M. A., Thomas P. A, and Glazer A. M., *Investigation of a peculiar relaxor ferroelectric: $Na_{0.5}Bi_{0.5}TiO_3$*. Ferroelectrics. 2002. **270**(1): p. 191–196.

Kingery W. D., Bowen H. K., and Uhlmann D.R., *Introduction to Ceramics*. New York: John Wiley & Sons, Inc., 1976.

Kunz, M., and Brown, I.D., *Out-of-Center Distortion around Octahedrally Coordinated d^0 Transition Metals*. Journal of Solid State Chemistry. 1995. **115**: p. 395-406.

Larson A. C., and Von Dreele R. B., *General Structure Analysis System (GSAS)*, Los Alamos National Laboratory Report LAUR. 2000: p. 86-748

Li J-F., Wang K., Zhang B-P., and Zhang L-M., *Ferroelectric and Piezoelectric Properties of Fine-Grained $Na_{0.5}K_{0.5}NbO_3$ Lead-Free Piezoelectric Ceramics Prepared by Spark Plasma Sintering*. Journal of the American Ceramic Society. 2006. **89**(2): p. 706-709.

Lee, P. L., Shu, D., Ramanathan, M., Preissner, C., Wang, J., Beno, M. A., Von Dreele, R. B., Lynn Ribaud, Kurtz, C., Antao, S. M., Jiao, X., and Toby, B. H., *A twelve-analyzer detector system for high-resolution powder diffraction*, Journal of Synchrotron Radiation. 2008. **15:** p. 427-432.

Matthias B. T., *New Ferroelectric Crystals*. Physical Review. 1949. **75**(11): p. 1771.

Megaw H. D., *Crystal Structure of Barium Titanate*. Nature. 1945. **155**: p. 484-485.

Naray-Szabo S., *Der Strukturtyp des Perowskits ($CaTiO_3$)*. Naturwissenschaften. 1943. **31**(16-18): p. 202-203.

Naray-Szabo S., *Die Strukturen von Verbindungen ABO_3 „Schwesterstrukturen.“*. Naturwissenschaften. 1943. **31**(39-40): p. 466.

Noheda, B., Cox, D. E., Shirane, G., Gonzalo, J. A., Cross, L. E., and Park, S. E., *A monoclinic ferroelectric phase in the $Pb(Zr_{1-x}Ti_x)O_3$ solid solution*. Applied Phyiscs Letters. 1999. **74**(14): 2059-2061.

Nomura, S., Kaneta, K., Kuwata, J., and Uchino, K., *Phase transition in the $PbTiO_3$-$A(B_{2/3}Nb_{1/3})O_3$ (A = La, Bi; B = Zn, Mg) solid solutions*. Materials Research Bulletin. 1982. **17**(12): p.1471-1475.

Park S-E., Shrout T. R., *Ultrahigh strain and piezoelectric behavior in relaxor based ferroelectric single crystals*. Journal of Applied Physics. 1997. **82**(4): p. 1804-1811.

Preissner, C., Shu, D., Toby, B. H., Lee, P., Wang, J., Kline, D. & Goetze, K., Nucl. Instrum. Methods Phys. Res. Sect. A., 2010, submitted.

Randall, C. A., Eitel, R., Jones, B., Shrout, T. R., Woodward, D. I., and Reaney, I. M., *Investigation of a high T_C piezoelectric system: $(1-x)Bi(Mg_{1/2}Ti_{1/2})O_3$-$(x)PbTiO_3$*. Journal of Applied Phyiscs. 2004. **95**(7): p. 3633-3638.

Salak A. N., Ferreira V. M., Ribeiro J. L., Vieira L. G, Pullar R. C, and Alford N. M., *Bismuth-induced dielectric relaxation in the (1−x)La($Mg_{1/2}Ti_{1/2}$)O_3–x Bi($Mg_{1/2}Ti_{1/2}$)O_3 perovskite system*. Journal of Applied Physics. 2008. **104**(1): p. 014105.

Sasaki A., Chiba T., Mamiya Y., Otsuki E., *Dielectric and Piezoelectric Properties of ($Bi_{0.5}Na_{0.5}$)TiO_3 - ($Bi_{0.5}K_{0.5}$)TiO_3 Systems*. Japanese Journal of Applied {hysics. 1999. **38**: p. 5564.

Seshadri, R., and Hill, N. A., *Visualizing the Role of Bi 6s "Lone Pairs" in the Off-Center Distortion in Ferromagnetic $BiMnO_3$*. Chemistry of Materials. 2001. **13**: p. 2892-2899.

Shannon, R. D., *Revised Effective Ionic Radii and Systematic Studies of Interatomic Distances in Halides and Chalcogenides*. Acta Crystallographica Section A. 1976. **32**: p. 751-767.

Shirane G., Newnham R., and Pepinsky R., *Dielectric Properties and Phase Transitions of $NaNbO_3$ and (Na, K)NbO_3*. Physical Review. 1954. **96**(3): p. 581.

Shuvaeava, V. A., Zekria, D., Glazer, A. M., Jiang, Q., Weber, S. M., Bhattacharya, P., and Thomas, P. A., *Local Structure of the lead-free relaxor ferroelectric (K_xNa_{1-x})$_{0.5}Bi_{0.5}TiO_3$*. Physical Review B. 2005. **71**: 174114.

Singh, D. J., *Structure and energetics of antiferroelectric $PbZrO_3$*. Physical Review B. 1995. **52**(17): p. 12559-12563.

Singh, D. J., Ghita, M., Fornari, M., Halilov, S. V., *Role of A-Site and B-site Ions in Perovskite Ferroelectricity*. Ferroelectrics. 2006. **338**: p. 73-79.

Smolenskii G. A., Isupov V. A., Agranovskaya A. I., and Krainik N. N., *New Ferroelectrics of Complex Composition IV*. Soviet Physics – Solid State. 1961. **2**(11): p. 2651-2654.

Stein, D. M., Suchomel, M. R., and Davies, P. K., *Enhanced tetragonality in (x)$PbTiO_3$-(1-x)Bi(B''$)O_3$ systems: Bi($Zn_{3/4}W_{1/4}$)O_3*. Applied Physics Letters. 2006. **89**: 132907.

Stringer C. J., Eitel R. E., Shrout T. R., Randall C. A., and Reaney I. M., Phase transition and chemical order in the ferroelectric perovskite (1-x)Bi($Mg_{3/4}W_{1/4}$)O_3–x$PbTiO_3$ solid solution system. Journal of Applied Physics. 2005. **97:** 024101.

Suchomel, M. R., and Davies, P. K., *Predicting the position of the morphotropic phase boundary in high temperature $PbTiO_3$-Bi(B''$)O_3$ based dielectric ceramics*. Journal of Applied Physics. 2004. **96**(8): p. 4405-4410.

Suchomel, M. R., and Davies, P. K., *Enhanced Tetragonality in (x)$PbTiO_3$-(1-x)Bi($Zn_{1/2}Ti_{1/2}$)O_3 and related solid solution systems*. Applied Physics Letters. 2005. **86**: 262905.

Suchomel, M. R., *Greater Functionality of Bismuth and Lead Based Perovskites*. University of Pennsylvania (Philadelphia). 2005

Suchomel, M. R., Fogg, A. M., Allix, M., Niu, H., Claridge, J. B., Rosseinsky, M., J., *Bi2ZnTiO6: A Lead-Free Closed-Shell Polar Perovskite with a Calculated Ionic Polarization of 150 μC/cm^2*. Chemistry of Materials. 2006. **18**(21): p. 4987-4989.

Suchomel, M. R., Davies, P. K., *Dielectric study of the $PbTiO_3$ – $Bi(Zn_{1/2}Ti_{1/2})O_3$ – $BiScO_3$ ternary system*. unpublished raw data, received in 2008.

Sun X., Chen J., Yu R., Sun C., Liu G., Xing X., and Qaio L., *$BiScO_3$ Doped $(Na_{0.5}K_{0.5})NbO_3$ Lead-Free Piezoelectric Ceramics*. Journal of the American Ceramic Society. 2009. **92**(1): p. 130-132.

Sunder, V.V.S.S.S., Halliyal, A., Umarji, A. M., *Investigation of tetragonal distortion in the $PbTiO_3$ – $BiFeO_3$ system by high-temperature x-ray diffraction*. Journal of Materials Research. 1995. **10**(5): p. 1301-1306.

Sutapun M., Huang C-C., Cann D. P., and Vittayakorn N., *Phase transitional behavior and dielectric properties of lead free $(1-x)(K_{0.5}Na_{0.5})NbO_3-xBi(Zn_{0.5}Ti_{0.5})O_3$ ceramics*. Journal of Alloys and Compounds. 2009. **479**(1-2): p. 462-466.

Swartz S., Shrout T. R., *Fabrication of perovskite lead magnesium niobate*. Materials Research Bulletin. 1982. **17**(10): p. 1245–1250.

Toby B. H., *EXPGUI, a graphical user interface for GSAS.* Journal of Applied Crystallography. 2001. **34:** p. 210-213.

Wang, J., Toby, B. H., Lee, P. L., Ribaud, L., Antao, S., Kurtz, C., Ramanathan, M., Von Dreele, R. B., and Beno, M. A., *A dedicated powder diffraction beamline at the Advanced Photon Source: Commissioning and early operation results.* Review of Scientific Instruments. 2008. **79:** p. 085105.

Watson, G. W., and Parker, S. C., *Origin of the Lone Pair of α-PbO from Density Functional Theory Calculations*. Journal of Physical Chemistry B. 1999. **103**: p. 1258-1262.

Zerr A., and Boehier R., *Melting of (Mg, Fe)SiO_3-Perovskite to 625 Kilobars: Indication of a High Melting Temperature in the Lower Mantle*. Science. 1993. **262**(5133): p. 553-555.

Zhong, W., and Vanderbilt, D., *Phase Transitions in $BaTiO_3$ from First Principles*. Phyiscal Review Letters. 1994. **73**(13): p. 1861-1864

Zuo R., Ye C., and Fang X., *Dielectric and Piezoelectric Properties of Lead Free $Na_{0.5}K_{0.5}NbO_3$ –$BiScO_3$ Ceramics*. Japanese Journal of Applied Physics. 2007. **46**(10A): p. 6733-6736.